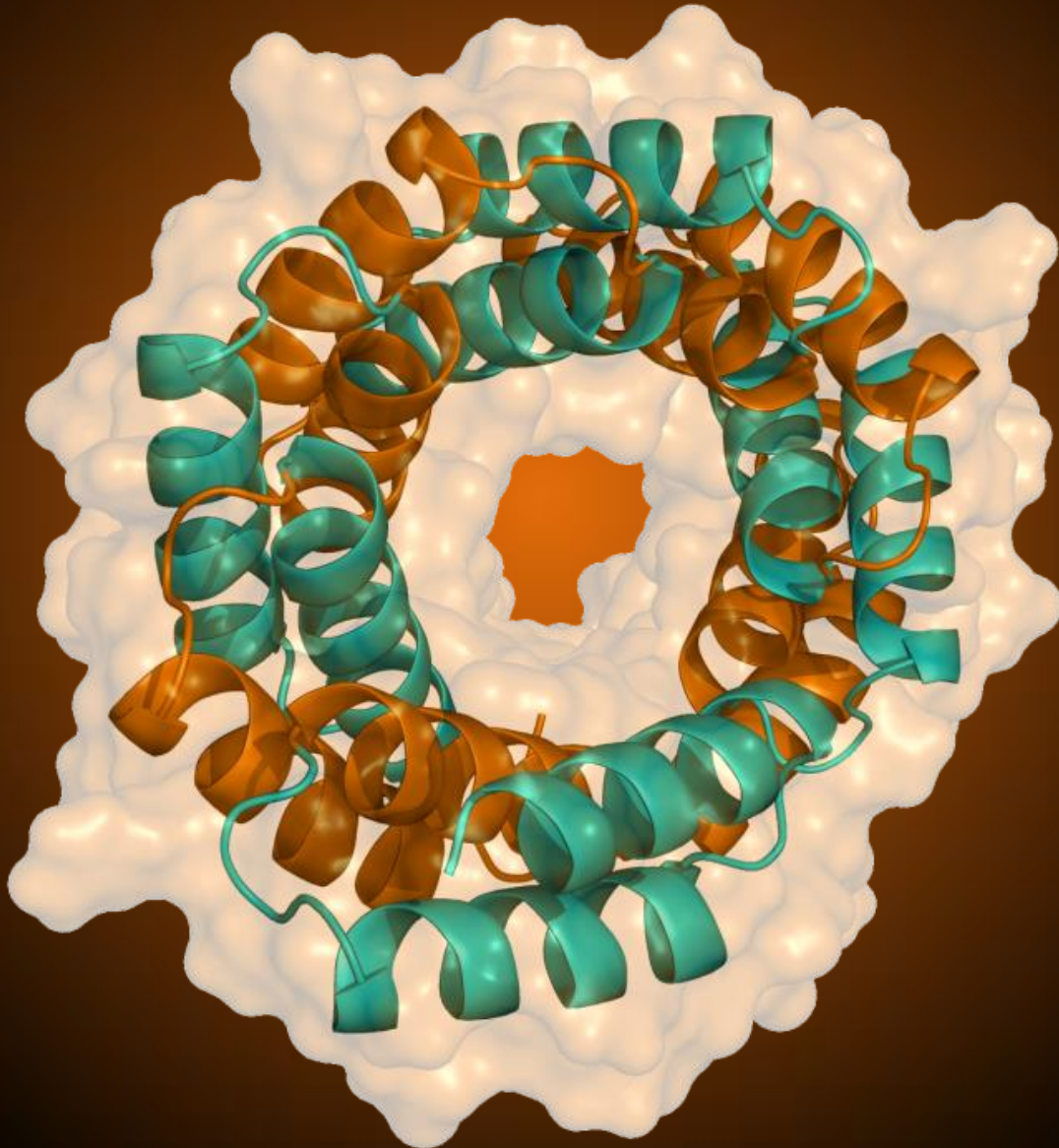


Engineered proteins as molecular templates for functional materials



Ph.D thesis

Daniel Sánchez de Alcázar Melendo

Donostia, 2019



Universidad
del País Vasco

Euskal Herriko
Unibertsitatea

Engineered proteins as molecular templates for functional materials

PhD Thesis

To obtain the Doctor of Philosophy degree in Molecular Biology and Biomedicine at the University of the Basque Country (EHU/UPV)

By

DANIEL SÁNCHEZ DE ALCÁZAR MELENDO

Donostia, 2019

Thesis Supervisor: Dra. Aitziber López Cortajarena (Biomolecular Nanotechnology Laboratory, CIC biomaGUNE)

University Tutor: Dra. Helena Ostolaza Etxabe (Department of Biochemistry and Molecular Biology, University of the Basque Country)

Funding Agencies

This thesis was economically supported by the European European Research Council ERC-CoG-648071-ProNANO (ALC), and the Spanish Ministry of Economy and Competitiveness (BIO2016-77367-R) (ALC). This work was performed under the Maria de Maeztu Units of Excellence Program from the Spanish State Research Agency – Grant No. MDM-2017-0720 (CIC biomaGUNE).

The results presented in this thesis have been published and listed below:

- 1) **Daniel Sánchez de Alcázar Melendo**; Sara Hernández Mejias; Erazo K; María Begoña Sot Sanz; Aitziber López Cortajarena. Self-assembly of repeat proteins: Concepts and design of new interfaces. *Journal of structural biology*. 201, pp. 118 - 129. DOI: 10.1016/j.jsb.2017.09.002.
- 2) **Daniel Sánchez-deAlcazar**; David Romera; Jose Castro-Smirnov; Ahmad Sousaraei; Santiago Casado; Jaime J. Hernandez; Anna Espasa; Isabel Rodríguez; Rubén D. Costa; Juan Cabanillas-Gonzalez; Ramses V. Martinez; Aitziber L. Cortajarena. Engineered protein-based functional nanopatterned materials for bio-optical devices. *Nanoscale Advanced*. Royal Society of Chemistry. DOI:10.1039/C9NA00289H.
- 3) **Daniel Sánchez de Alcázar Melendo**; Susana Velasco-Lozano; Nicoll Zeballos; Feranndo López-Gallego; Aitziber L. Cortajarena. Biocatalytic Protein-Based Materials for Integration into Energy Devices. *Chem-Bio-Chem*. 20, pp. 1977-1985. Wiley Online Library. DOI: 10.1002/cbic.201900047.

Acknowledgments

I want to start paraphrasing to Newton, “If have seen further it is by standing on the shoulders of Giants”. The latter quote was written in a letter sent to Robert Hooke 1676 in which Newton pointed out that he was able to see more and farther because he had the whole knowledge harvested for centuries from predecessors to do it. So, I would like to express my sincere gratitude to my advisor Dr. Aitziber López Cortajarena for helping me to see more and farther. Also, I would like to thank her for the continuous support of my Ph.D study and research, for his patience, motivation, enthusiasm, and immense knowledge. His guidance helped me in all the time of research and writing of this thesis. I could not have imagined having a better advisor and mentor for my Ph.D study.

I wish to show my gratitude to CIC biomaGUNE center and all staff members for support and excellent labour, including administration, platforms, direction, maintenance and cleaning staff. They have made this thesis possible in an unpainful way.

I thank my fellow labmates in Biomolecular nanotechnology group: Antonio, Elena, Mantas, Idoia, Eduardo, Leire, Lisa, Lucia, Laura, Alba, Dina, Silvia, Javi (better known as Cao de Benós) and Juan Gurruchaga, for the stimulating discussions, and for all the fun we have had in the last four years. In particular, I am grateful to Sara for enlightening me the first glance of research. Also I thank my friends that I met in Biomagune: Aldo (better known as Chochi), Dani Mexican, Anuki, Bea, Susana, Chus, Marta and Verini. Finally, I would like to thank those people that do not belong to Biomagune but that we shared moments and travels: Juanito.

Last but not the least, I would like to thank my family: my *aitas* Eduardo and Encarnación, for giving birth to me at the first place and supporting me spiritually throughout my life. Also the rest of my family for being there and for having helped me when I needed, including my aunt Tomás, Belén, my *grandaítas* (Juan and Encarnación), my *ama* in law (Juana), Rafa and Yola. Finally, I want to thank all my friends: Marcos (better known as Beckham), Jorge, Sandri, Loreai, Charlai, Wiso, Victorino, Nichi, Sunny, Xmas and Varitono, for their help, at some point, and spontaneous visits to Donosti, in some cases (I hate you! you know who you are).

I reserve my best words for Remei, thank you for showing up in my life in the best moment, even though any moment would have been the best moment. Thank you for your love, help and support, and also for correcting my English stuffs.

Acknowledgements

Finally I want to thank all those women and men that have died on behalf of science. They gave their entire life for the knowledge and progress. Their success in this matter have achieved that all of us enjoy of the technologies advances and very deep knowledge of Universe, that, among other things, has denied false ideas or theories such as homeopathy, spontaneous generation, vitalism, that Earth is not flat, that nobody live in the center of the Earth or that the evolution theory is not true. The tortuous path toward the scientific successful requires great willingness and do not succumb to failure, being the failure the normal daily situation, as a labmate said "There are good days and bad years". I am still waiting for those days come to me.

Table of Contents

Resumen	1
Summary	7
Chapter 1. Introduction: Proteins applied in nanobiotechnology	12
1.1. Elements for life	14
1.2. Proteins: general aspects	15
1.3. Proteins: sophisticate nano-machines	17
1.4. Life is chiral	19
1.5. From the Nature	20
1.6. Proteins as nanobiotechnology tool	21
1.7. Repeat proteins	25
1.8. CTPR protein as ideal scaffold	26
Chapter 2. Self-assembly of repeat proteins: Concepts and design of new interfaces	29
2.1. Background	31
2.1.1. Nanotubes based on proteins: previous work	31
2.2. Introduction	37
2.2.1. Higher-order protein assemblies: natural and designed	37
2.2.1.1. Relevance of protein assemblies in Nature	37
2.2.1.2. Designed assemblies: relevance in applications	38
2.2.2. Repeat proteins: ideal scaffold for protein engineering	41
2.2.3. Protein based nanotubes	42
2.3. Experimental section	45
2.3.1. Protein design, molecular engineering, and protein purification	45
2.3.2. Gel electrophoresis	46
2.3.3. Size exclusion chromatography	46
2.3.4. Circular dichroism (CD) measurements	46
2.3.5. Transmission electron microscopy (TEM)	46
2.3.6. TEM image processing, particle selection, and 2D classification	47
2.3.7. Computational analysis based on docking simulations	47
2.4. Results and Discussion	47
2.4.1. Nanotubes based on repeat proteins: concept and design	47
2.4.2. Characterization of higher order assemblies	49
2.4.2.1. Electrostatic model	49
2.4.2.2. Aromatic model	51

2.5. Conclusions	53
Chapter 3. Engineered protein-based functional nanopatterned materials for bio-optical devices	56
3.1. Background	58
3.1.1. CTPR protein films	58
3.1.2. Functional protein films	61
3.2. Introduction	63
3.3. Experimental section	66
3.3.1. Protein production and purification	66
3.3.2. Generation of nanopatterned protein films	67
3.3.3. Crosslinking of the nanostructured protein films	68
3.3.4. Structural characterization of the nanostructured protein films	68
3.3.5. Optical characterization of the nanostructured protein films	69
3.3.6. Distributed feedback (DFB) lasers from nanostructured CTPR-Rh6G films	71
3.4. Results and Discussion	72
3.5. Conclusions	81
Chapter 4. Biocatalytic protein-based materials for integration into energy devices	84
4.1. Background	86
4.1.1. Nanogenerators as a source of clean energy	86
4.1.2. Bioinorganic generator: Catalase as a source of mechanical energy	87
4.1.3. Enzyme immobilization	88
4.2. Introduction	89
4.3. Experimental section	92
4.3.1. Materials	92
4.3.2. Protein expression and purification	92
4.3.3. Protein thin films fabrication	93
4.3.4. Scanning electron microscopy (SEM)	93
4.3.5. Circular dichroism	93
4.3.6. Crosslinking of the protein thin films	93
4.3.7. Distribution of CAT in thin films by fluorescence imaging and fluorescence anisotropy	94
4.3.8. Enzymatic activity measurements	94
4.3.9. Electric Energy Output Measurements	95
4.4. Results and Discussion	96
4.4.1. Protein-based biomaterial fabrication and characterization	96
4.4.2. Activity and stability of CAT entrapped into the CTPR protein film	99

4.4.3. Energy output measurements	102
4.5. Conclusions	105
General conclusions	106
Appendixes	112
A.1. Self-assembly of repeat proteins: Concepts and design of new interfaces	114
A.2. Engineered protein-based functional nanopatterned materials for bio-optical devices	125
A.3. Biocatalytic protein-based materials for integration into energy devices	135
References	141

Resumen

Desde la revolución industrial a mediados del siglo XVIII hasta en la actualidad, los avances tecnológicos han logrado increíbles progresos en todas las ramas de la ciencia. Todo ello fundamentado en los avances de la ciencia básica que sirve de apoyo y punto de partida para el desarrollo de novedosas aplicaciones. Este desarrollo tecnológico ha permitido el estudio y la búsqueda de nuevos materiales con propiedades ópticas, magnéticas y/o electrónicas específicas y mejoradas. La demanda de nuevos materiales con nuevas funcionalidades o funcionalidades mejoradas y cada vez más sofisticadas ha llevado al desarrollo y diseño de nuevos compuestos orgánicos e inorgánicos que a pesar de tener buena propiedades funcionales muchas veces son contaminantes e incluso tóxicos. La naturaleza a lo largo del proceso evolutivo ha conseguido resolver infinidad de problemas. Por un lado, optimizando al máximo ciertos procesos biológicos, como podría ser la catálisis de reacciones químicas. Por otro lado, desarrollando algunos procesos nuevos, como por ejemplo la síntesis de nuevos materiales con propiedades físico-químicas específicas, como puede ser la proteína de la seda que posee propiedades mecánicas como resistencia y elasticidad excelentes.

Uno de los grandes hitos tecnológicos en el campo de la nanociencia ha sido el desarrollo de la bionanotecnología, una rama de la tecnología que aprovecha el conocimiento de la biología molecular para construir máquinas moleculares, materiales y estructuras complejas con alto valor añadido. Una de las aproximaciones implementadas actualmente en el desarrollo de estas tecnologías es el *“bottom-up”* que utiliza las propiedades de auto-ensamblaje de las biomoléculas para la fabricación de estructuras supramoleculares y materiales con aplicaciones en una gran variedad de campos, desde la nano-electrónica hasta la biomedicina. Consecuentemente, esta aproximación requiere de un conocimiento preciso y extenso, así como del control, de las propiedades físico-químicas que gobiernan las interacciones entre biomoléculas y que en última instancia dirigen el ensamblaje.

En este sentido, las proteínas de repetición pueden desempeñar un papel importante ya que su estructura modular y jerárquica permite el diseño y control apropiado para la formación de estructuras supramoleculares y materiales funcionales aplicando estrategias *“bottom-up”*. Concretamente, las proteínas de repetición a partir de una secuencia consenso de la familia de repeticiones *“tetratricopeptide repeat”* (CTPR) han sido empleadas ampliamente como herramienta nanotecnológica. Estas proteínas se caracterizan por estar formadas por un motivo estructural hélice-giro-hélice compuesto por 34 amino ácidos de los cuales 8 amino ácidos están

altamente conservados en la secuencia. La combinación en tándem de este motivo estructural da lugar a una superhélice dextrógira, necesitando 8 repeticiones de este motivo estructural para completar un giro de la superhélice. En esta tesis, las proteínas CTPR toman el papel central habiendo sido usadas para el diseño y desarrollo de estructuras y materiales funcionales con aplicaciones en energía y en óptica.

Esta tesis está dividida en cuatro capítulos. El primer capítulo introduce al mundo de las proteínas haciendo hincapié en su estructura y funcionalidades. También, se describe el estado actual del campo de los materiales funcionales y estructuras supramoleculares, en el contexto de la temática de la tesis. Por último, se introduce y se explica detalladamente la estructura, origen, función y aplicaciones de las proteínas de repetición, para finalmente, centrarnos en las proteínas CTPR como principales protagonistas de la tesis.

En el capítulo 2, titulado *“Self-assembly of repeat proteins: Concepts and design of new interfaces”*, se describe el estado actual, a nivel fundamental, en el diseño de nuevas interfaces para la interacción entre proteínas para generar estructuras supramoleculares. Específicamente se desarrolló una nueva aproximación experimental para formar estas estructuras supramoleculares a través del auto-ensamblaje *“bottom-up”* usando proteínas de repetición, CTPR. Las proteínas CTPR contienen múltiples copias de repetición idénticas que interactúan a través de la interfaz entre repeticiones para formar una superhélice. Considerando la geometría y simetría de estas proteínas, e introduciendo nuevos puntos de interacción a lo largo de la superhélice a través de ingeniería genética, se logró la expresión de una nueva proteína CTPR con una nueva interfaz. Esta nueva interfaz promueve y favorece la interacción y ensamblaje entre dos proteínas, que finalmente, dan lugar a la formación de una estructura tubular (**Figura 1**). En un modelo previo, en el que se diseñó una nueva interfaz con pares basados en amino ácidos hidrofóbicos, se observó la formación de estructuras diméricas tubulares, aunque con el inconveniente de la formación de estructuras oligoméricas debido a la inespecificidad de las interacciones. Partiendo de estos estudios, desarrollamos dos modelos para la formación de nanotubos basados en CTPRs, uno basado en interacciones electrostáticas, y otro en interacciones π - π . Los modelos fueron evaluados computacionalmente para verificar que las estructuras generadas son favorables en términos energéticos como para dar lugar predominantemente a una estructura tubular estable. Las mutaciones se realizaron en las posiciones 15 y 31 de cada repetición, donde por simetría resultan ser zonas de contacto entre las dos proteínas. En el primer modelo se realizaron

mutaciones introduciendo His y Asp, de manera que la dimerización ocurre entre los pares His-Asp a través de interacciones electrostáticas. En el caso del segundo modelo se mutaron las mismas posiciones a Tyr formando interacciones π - π entre los pares Tyr-Tyr. Se aislaron los ensamblajes y se caracterizó su estructura y estabilidad. Estos estudios aportan nuevo conocimiento respecto al diseño de nuevas interfaces entre proteínas para el control del ensamblaje y formación de estructuras más complejas.

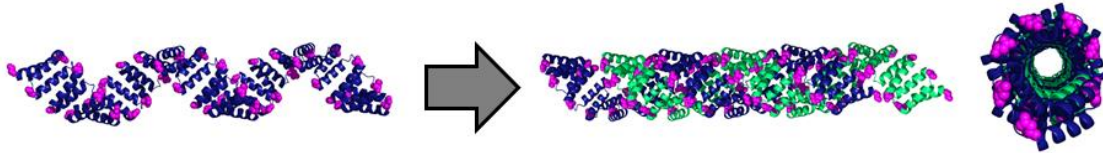


Figura 1. Representación del modelo estructural de un nanotubo formado por dos proteínas CTPR interactuando a través de una nueva interfaz. En azul la proteína que forma el dímero con otra proteína homóloga coloreada en verde. Los puntos de color rosa representan los puntos de contacto a través de la interacción entre las cadenas laterales de los amino ácidos que conforman la nueva interfaz.

Los capítulos 3 y 4 están dedicados a la fabricación de películas proteicas basadas en proteínas CTPR. En trabajos previos se demostró que esta formación de películas es una cualidad inherente a la estructura de las CTPRs. Estas proteínas pueden formar películas ordenadas que se producen como consecuencia de interacciones intermoleculares “*head-to-tail*” y “*side-to-side*”, y que proporcionan direccionalidad a las proteínas en el material. En estos capítulos se dio un paso más allá para generar películas funcionales basadas en estas proteínas de repetición con posible aplicación en óptica y en el campo de energética.

El desarrollo de nuevos materiales y dispositivos que sean activos y bio-compatibles para su implementación en múltiples campos es una necesidad actual, incluyendo la fabricación de dispositivos con potencial para la implementación en aplicaciones biomédicas, y dispositivos que sean sostenibles para aplicaciones en bio-óptica y bio-optoelectrónica.

En el capítulo 3, titulado “*Engineered protein-based functional nanopatterned materials for bio-optical devices*”, se describe una estrategia simple para usar proteínas en el desarrollo de materiales funcionales basado en proteínas CTPR. Usando estas proteínas como módulos simples para la fabricación, se obtuvo un material ópticamente activo. La estrategia de fabricación propuesta es la de generar películas proteicas finas y flexibles, a través del auto-ensamblaje de la proteína y con una nano-estructura que es transferida a la superficie de la proteína a través de un

sello polimérico mediante una técnica conocida como nanolitografía suave. Esta película proteica nanoestructurada es fácilmente transferible a objetos 3D (planos o curvos) por adhesión o por la generación del material directamente en la superficie. Además, las películas proteicas flexibles y nanoestructuradas son preparadas incorporando una fina capa polimérica como soporte, que permite una manipulación fácil del material. Por último, la modularidad de las CTPR nos permitió modificar la proteína seleccionada como andamio molecular, introduciendo una Cys única en el C-terminal de la proteína, para conjugar una molécula fluorescente a la Cys y desarrollar dispositivos laser. La organización de esta molécula en una película proteica dio lugar a la obtención de Emisión Espontánea Amplificada (ASE, del inglés *Amplified Spontaneous Emission*), un fenómeno foto-físico que permite la emisión de luz en un rango estrecho de longitudes de onda. Además, la organización de esta molécula en una película con una nanoestructuración específica, permitió observar otro fenómeno foto-físico que proporciona luz coherente, es decir, emisión laser (DFB, del inglés *Distributed Feedback Laser*) (**Figure 2**). Por lo tanto, este trabajo resultó en la producción de materiales y dispositivos basados en proteína funcionales con propiedades de emisión laser eficientes que pueden ser de utilidad en el desarrollo de biosensores o de aplicaciones en telecomunicaciones.

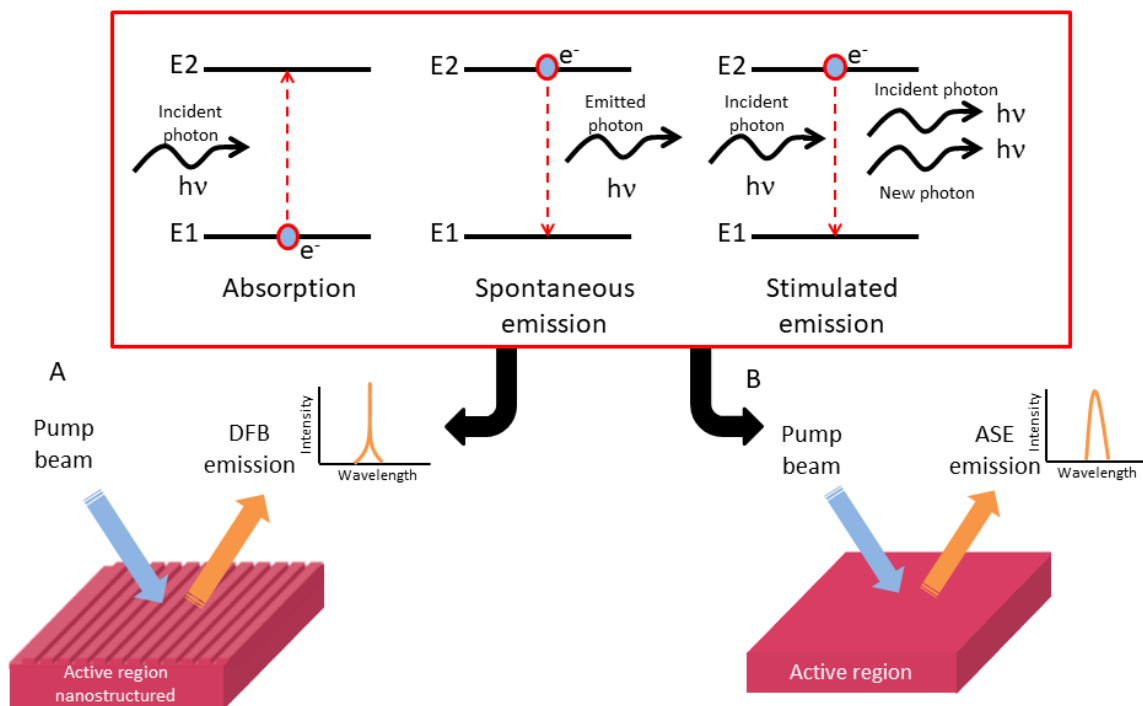


Figura 2. El panel superior muestra la representación teórica en términos de transición energética del fenómeno de DFB y ASE. Una representación esquemática del fenómeno de DFB y ASE mostrando la región activa nanoestructurada y sin nanoestructuración, y las

diferencias a nivel espectral. Panel inferior: **A.** Nanoestructuración de la región activa que da lugar al confinamiento de la luz y por tanto al fenómeno de DFB (luz coherente). **B.** Región activa sin nanoestructuración que da lugar al fenómeno de ASE (luz no coherente).

Dado el estado actual de las tecnologías y recursos en materia energética, es imperativo buscar nuevas fuentes y recursos para abastecer la demanda energética global. Además, estas nuevas fuentes o recursos deben superar las limitaciones de las actuales fuentes como la reusabilidad, la sostenibilidad o el impacto ambiental. En el capítulo 4, titulado *“Biocatalytic protein-based materials for integration into energy devices”*, se explora esta vertiente de aplicación usando materiales basados en proteínas. En este contexto, se investigó la posibilidad de fabricar películas proteicas catalíticas para generación de energía limpia. En un primer paso, se verificó que estas proteínas podrían inmovilizar enzimas sin que la enzima, en este caso la catalasa, perdiese su actividad catalítica. Para ello, dado que la propia inmovilización en la película no es suficiente para generar un material resistente en un ambiente acuoso, se realizó una reacción de fijado con glutaraldehído. Tras la verificación de que la enzima se mantiene activa, se caracterizaron tanto las propiedades cinéticas como estructurales, integridad estructural, orden, estabilidad y reusabilidad de estos materiales catalíticos. La actividad catalítica de la catalasa produce la dismutación del peróxido de hidrógeno en agua y oxígeno. Se aprovechó la liberación del oxígeno molecular como fuente de energía mecánica acoplando estos materiales funcionales a un sistema piezoeléctrico para fabricar un generador bioinorgánico (**Figure 3**). Este dispositivo es capaz de producir electricidad desde una fuente renovable, a través del gas producido por la reacción de la catalasa que estimula mecánicamente el material piezoeléctrico. Los resultados mostraron que el sistema pudo estimular la producción de energía a través de las burbujas de oxígeno producidas en la interfaz película catalítica-piezoeléctrico, aunque no tan eficientemente como la enzima en solución. No obstante, estas películas catalíticas tienen dos ventajas importantes con respecto al sistema en solución. La primera es la reusabilidad, se puede reusar el sistema hasta diez veces manteniendo hasta el 50% de la energía producida. La segunda ventaja es en relación con la capacidad de producción de energía en función del volumen de reacción. Mientras el sistema en solución alcanza la saturación energética con un volumen de reacción de 1 ml, en la película catalítica la energía producida sigue incrementando exponencialmente.

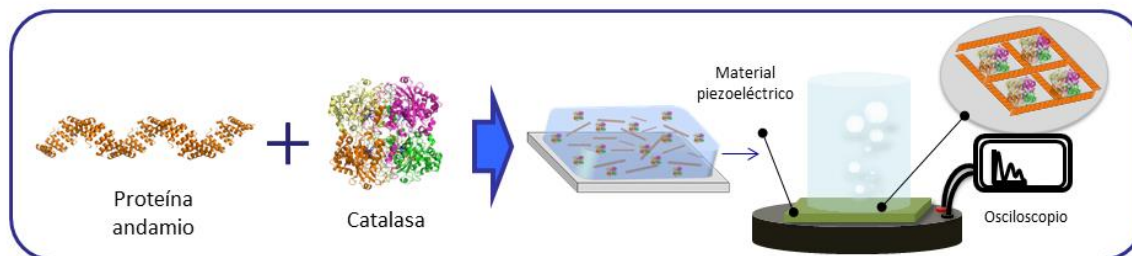


Figure 3. Representación esquemática de inmovilización de la catalasa usando un soporte proteico, y posterior acople a un sistema piezoeléctrico para la producción de energía (generador bioinorgánico).

En conclusión, en esta tesis se ha estudiado la formación de estructuras supramoleculares así como la fabricación materiales funcionales basados en proteínas CTPR. Desde un punto puramente científico, el diseño de nuevas interfaces proteína-proteína con capacidad de auto-ensamblaje plantea un auténtico reto. Aquí se abordó una nueva aproximación experimental para el auto-ensamblaje de proteínas CTPR cuyos diseños consiguieron promover la formación de estructuras supramoleculares con forma tubular. Por otro lado, en el contexto de materiales funcionales, se han fabricado materiales basados en CTPR para su aplicación tanto foto-física como en energética. La simple organización de moléculas fluorescentes en películas de proteínas (aproximación “*bottom-up*”) y una apropiada nanoestructuración (aproximación “*top-down*”) dio lugar a emisión laser. Esto abre la puerta al desarrollo de nuevos dispositivos basados en proteínas con potencial para la sustitución de los actuales materiales usados en nanotecnología y que en muchos casos producen efectos negativos en el medioambiente. Finalmente, también se pudo desarrollar una metodología para la fabricación de materiales catalíticos para su integración dispositivos de producción de energía. A través de la inmovilización de catalasa usando como soporte proteínas CTPR y a su vez acoplado este material biocatalítico a un transductor de señal o nanogenerador se consiguió la producción de energía limpia y reusable a partir de una reacción enzimática, lo cual supone una nueva aproximación para el desarrollo de nuevas tecnologías de energía sostenible.

Summary

The current state-of-the-art of biotechnology has improved tremendously over the last decades. Currently, the physico-chemical properties can be manipulated at molecular scale. Bottom-up design of complex functional nanostructures is of the great interest because it allows the synthesis of ordered structures using the intrinsic self-assembly properties of simple components. In this sense, repeat proteins are useful tools for this task due to their modular and hierarchical structure, which can be the basis to construct complex supramolecular assemblies. In this thesis, repeat proteins and in particular consensus tetratricopeptide repeat proteins (CTPR) have been employed to generate higher order structures and to design and fabricate functional materials. CTPR proteins belong to the large family of repeat proteins and consist of a 34 amino acids helix-turn-helix domain. CTPR repeats can be combined in tandem to form superhelical arrays, in which eight repeats comprise one full turn of the superhelix.

This thesis is divided in four chapters. The first chapter introduces in detail the main characteristics of proteins at a fundamental level including their vast functionality in Nature. In addition, it is also covers the potential applications in nanobiotechnology of proteins and protein-based materials giving an overview of the current state of the art in the area of interest of this thesis.

The chapter 2, entitled “Self-assembly of repeat proteins: Concepts and design of new interfaces”, focuses on fundamental concepts of the design of new protein interfaces. We describe an experimental approach to form higher order architectures by a bottom-up assembly of CTPR building blocks. CTPR arrays contain multiple identical repeats that interact through a single inter-repeat interface to form elongated superhelices. Introducing a novel interface along the CTPR superhelix allows two CTPR molecules to assemble into protein nanotubes (PNTs). Two approaches are applied to form protein nanotubes based on electrostatic interactions and on π - π interactions. The supramolecular structures obtained are isolated and their structure and stability characterized. In addition, the nanotube formation is analyzed considering the energy of the interaction and the structure in the two different models. These studies provide insights into the design of novel protein interfaces for the control of the assembly into more complex structures, which will open the door to the rational design of nanostructures and ordered materials for many potential applications in nanotechnology.

Chapters 3 and 4 are dedicated to the fabrication of CTPR-based protein films. Previously, we have reported the formation of self-assembled protein films in which the protein components are

organized through “head-to-tail” and “side-to-side” interactions, providing order and directionality to the protein within the material. In this work, we take a step beyond generating functional films based on repeated proteins with applicability in different fields such as optics and energy production.

The development of new active biocompatible materials and devices is a current need for their implementation in multiple fields, including the fabrication of implantable devices for biomedical applications and sustainable devices for bio-optics and bio-optoelectronics. Chapter 3, entitled “Engineered protein-based functional nanopatterned materials for bio-optical devices”, describes a simple strategy to use designed proteins to develop protein-based functional materials. Using simple proteins as self-assembling building blocks to create a platform for the fabrication of new optically active materials. This study takes one step further previous works on the design of materials with defined structures and functions using naturally occurring protein materials, such as silk. The proposed fabrication strategy generates thin and flexible nanopatterned protein films by letting the engineered protein elements to self-assemble over the surface of an elastomeric stamp with nanoscale features. These nanopatterned protein films are easily transferred onto 3D objects (flat and curved) by moisture-induced adhesion. Additionally, flexible nanopatterned protein films are prepared incorporating a thin polymeric layer as a back support. Finally, taking advantage of the tunability of the selected protein scaffold, the flexible protein-based surfaces are endowed with optical function, achieving efficient lasing features. As such, this work enables the simple and cost-effective production of flexible and nanostructured, protein-based, optically active biomaterials and devices over large areas toward emerging applications.

Finally, Chapter 4, entitled “Biocatalytic protein-based materials for integration into energy devices”, demonstrates the fabrication of catalytic protein thin films by the entrapment of catalase into protein films composed of a scaffolding protein. Extensive structural, and functional characterization of the films evidences the structural integrity, order, stability, catalytic activity, and reusability of the biocatalytic materials. Finally, these functional biomaterials are coupled with piezoelectric discs to fabricate a bioinorganic generator. This device is capable to produce electricity from renewable fuels through catalase-driven gas production that mechanically stimulate the piezoelectric material.

In summary, in this thesis we have studied the formation of supramolecular structures as well as the fabrication of functional materials based on CTPR proteins. From a fundamental science perspective, the design of new protein-protein interfaces is considered an authentic challenge. Here a new approach was tackled for the self-assembly of CTPR proteins. The designs shown in the chapter 2 formed energetically favorable tubular-shape structures. In the context of functional materials, we were able to fabricate materials with optical and catalytic properties. The organization of laser dyes on a protein film (“bottom-up” approach) and the endowment of a suitable nanostructure gave rise to laser emission. This result opens up the door to the development of new protein-based devices less biodegradable and toxic with potential for substitution of older systems. Finally, a new methodology for the fabrication of catalytic materials and for their integration into energy devices was achieved. The immobilization of catalase enzyme in a protein film, using CTPR proteins as scaffold, and its coupling to a signal transductor (nanogenerator) made possible to produce green and reusable energy. These results imply a new approach for the development of new clean and sustainable sources of energy.

Chapter 1

**Introduction: Proteins applied in
nanobiotechnology**

1.1. Elements for life

According to the Big Bang theory, the universe began about 15 billion years ago from an extreme and highly dense dot. Upon the rapid expansion and consequently cooling of the universe was possible the formation the first atoms that ultimately culminated with the formation of the all matter that conform the known Universe^[1]. Until now, 118 are the elements discovered. Most of them are the responsible for making up the whole existent matter, but only 25 are believed to be essential for life. From those the most abundant are carbon, hydrogen, oxygen, nitrogen and sulfur together with some elements that belong to the alkaline and alkaline earth group, *i.e.* Na, Mg, K and Ca, known as bulk elements. In lower proportion, but not less meaningful, transition metals and elements as B, F, Si, P, S, Cl, Se, and I (trace essential elements) can be found in different organisms taking part in key biological functions. However, these elements can be essential for some organisms but toxic for others. Such is the case of the W (transition metal) which is found in enzymes of some thermophilic bacterial while its presence is toxic in others bacterial strain (**Figure 1**). Controversial is the case of Cr, which might be included as trace element possibly essential but its role in biological systems are still under discussion^[2,3].

1												13					14	15	16	17	18
H	2											B	C	N	O	F	Ne				
Li	Be											Al	Si	P	S	Cl	Ar				
Na	Mg	3	4	5	6	7	8	9	10	11	12	Ga	Ge	As	Se	Br	Kr				
K	Ca	Sc	Ti	V	Cr	Mn	Fe	Co	Ni	Cu	Zn	In	Sn	Sb	Te	I	Xe				
Rb	Sr	Y	Zr	Nb	Mo	Tc	Ru	Rh	Pd	Ag	Cd	Hg	Tl	Pb	Bi	Po	At	Rn			
Cs	Ba	Lu	Hf	Ta	W	Re	Os	Ir	Pt	Au	Hg	Tl	Pb	Bi	Po	At	Rn				
Fr	Ra	Lr	Rf	Db	Sg	Bh	Hs	Mt	Ds	Rg	Cn	Nh	Fl	Mc	Lv	Ts	Og				

Legend:
■ Bulk elements
■ Trace essential elements
■ Trace elements possibly essential

Figure 1. Table periodic of elements indicating the essential elements for life.

It is estimated that the Earth was formed 4.5 billion years ago and the first living organisms did not emerge until roughly 1 billion years later^[4]. During this period of time, the primitive Earth conditions were changing up to have softer conditions that enabled the synthesis of complex molecules based on carbon. In the carbon chemistry underlie whole chemistry of the life, the building blocks of the current biomolecules, *i.e.* nucleotides, monosaccharides, phosphates, lipids, and amino acids. These molecules, in turn, led to the formation of more complex molecules such

as nucleic acids, proteins, phospholipids, and polysaccharides which are the responsible for self-assembly of simple self-replicating organism that gave rise to the superior organisms throughout evolution^[5-7].

1.2. Proteins: general aspects

Among all macromolecules in Nature, proteins attract special attention due to large chemical versatility and diverse functionality within biological systems. They are the most abundant macromolecule in cells, up to $\approx 50\%$ of the cell's total dry mass^[8]. Moreover, the number of different functional proteins in cells and tissues is much higher than the number of other macromolecules^[9]. Conceptually, proteins are linear polymers consisting of L-amino acids which are held together by peptide or amide bonds. In Nature there are 20 different amino acids which are the basic building units to form protein sequences. Proteins are encoded in genetic material, *i.e.* in the DNA which is made of chemical building blocks called nucleotides. These building blocks are composed of three parts: a phosphate group, a sugar group and one of four types of nitrogen bases. To form a strand of DNA, nucleotides are linked into chains, with the phosphate and sugar groups alternating. The four types of nitrogen bases found in nucleotides are Adenine (A), Thymine (T), Guanine (G) and Cytosine (C). The order of these bases determines what biological instructions are contained in a strand of DNA^[10]. Amino acids can be classified according to chemical properties of the side chain, thus there is four well-defined groups, non-polar, polar, negatively charged, and positively charged, providing high chemical variability. The amino acid combination has the potential to generate a wide spectrum of linear/primary sequences. For instance, considering a protein length of 50 amino acids (small protein as insulin) the total possible combination ascends to 50^{20} (or 9.5×10^{33}) permutations. In addition, the polypeptide backbone offers much greater conformational freedom than nucleic acid and polysaccharides, which in terms of possible configurations becomes staggering. However, not all protein sequences adopt stable and functional structures. The dominant structure-function paradigm establishes that one protein sequence encodes a unique protein structure which determines its function, *i.e.* Anfinsen's dogma^[11-13]. Nonetheless, that dogma is starting to change in the current scientific stage. The development of new tools for studying the structure, dynamics, and function of proteins has enabled to demonstrate that proteins are not strictly static objects. They do not adopt unique, well-folded three-dimensional structures but they can populate ensembles of diverse,

interconverting conformations, which can be also related with a functional diversity encoded in unique sequences ^[14,15].

In this sense, proteins are classified attending to hierarchical order. The first order was mentioned lines above, is the amino acids sequences (primary structure) which provide the intrinsic information that gives rise to the secondary structure formation. This secondary structure refers to the highly regular local folding of the amino acid chains in two main types of structures permitted by the Ramachandran diagram (torsional angles allowed in an amino acids sequence that prompt a spotted structural geometry), alpha-helix and beta-sheet^[9,16]. Finally, the subset of secondary structures conform the tertiary structure, i.e. the tridimensional structure or global folding of the protein, in which non-covalent interactions, hydrogen bond, ionic, Van der Waals and hydrophobic interactions, are the responsible for maintaining the three-dimensional structure^[17,18]. Additionally, there are two extra order levels, super-secondary structure, i.e. subset of secondary structure that create specific and repetitive pattern as the β -barrel in the GFP proteins^[19], and quaternary structure. This latter is the connection between two or more polypeptides chains (subunits) to form a multimer with a determined molecular function stabilized by non-covalent interaction and/or disulfide bridge, e.g. the tetrameric protein, hemoglobin, which is composed by four subunits^[20,21] **(Figure 2)**.

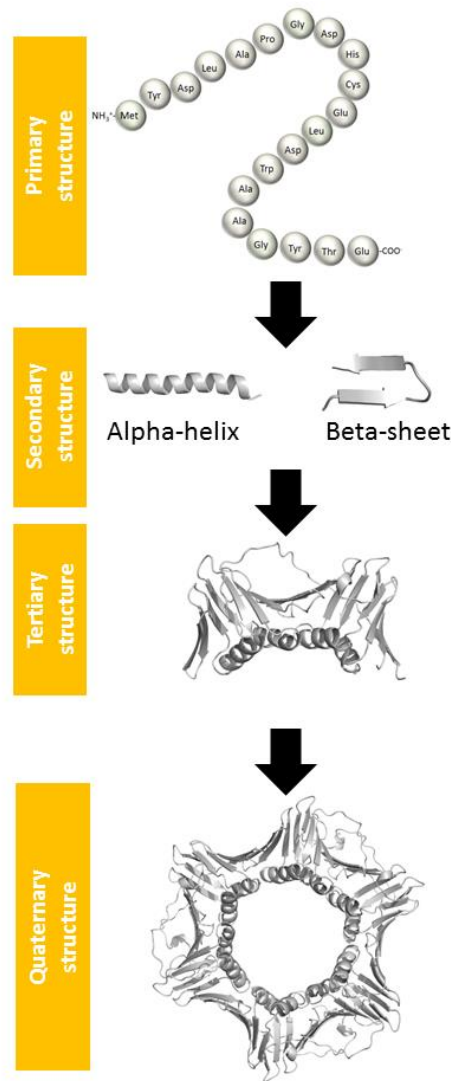


Figure 2. Hierarchical order of protein structure. Proliferating cell nuclear antigen (PCNA) protein as example of tertiary and quaternary structure (PDB ID: 1AXC)^[22].

1.3. Proteins: sophisticate nano-machines

Proteins are involved in many biological processes carrying out a broad range of distinct roles (**Table 1**). Each protein accomplishes its function specifically and simultaneously in an environment full of molecules. For instance, proteins can act as catalysts accelerating certain chemical reactions that take place in physiological conditions in a short period of time, i.e. they reduce the activation energy between reagents and products within cells without changing their nature. In doing so, reactions that take for long time (from minutes to millions years) occur in a time scale of 10^{-5} to 10^2 sec^[23]. Also they can have a structural character taking part in the architecture of cells, tissues and organs such as collagen present in all connective tissues, or dystrophin present in muscle

cells^[24,25]. Proteins play another key functions as molecular carriers (hemoglobin or hemocyanin) or regulating of molecules traffic through cellular membranes (e.g. Na⁺/K⁺ channels)^[26–28].

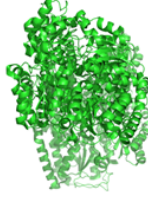
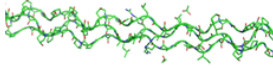

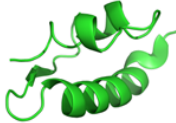
Protein	Function	Structure
Nitrogenase	Catalytic (nitrogen fixation)	
Collagen	Structural protein	
Hemocyanin	Oxygen-carrying protein	
Insulin	Messenger (hormone)	

Table 1. Examples of different protein functions in biologic systems. (PDB ID: 5vpw, 1bkv, 1nol, 3l40)^[29–32].

1.4. Life is chiral

All living being biomolecules are chiral, *i.e.* they have asymmetric carbon or asymmetric plane^[33,34]. Amino acids can exist in two distinguishable mirror-image forms, L-amino acid or D-amino acid, as well as it occurs with carbohydrates and nucleic acids. Essentially, they differ in their capacity to rotate plane-polarized light by equal amounts but in opposite directions. However, just one of enantiomers is present in Nature, L- amino acids for proteins and D- ribose for nucleic acids. This homo-chirality arose probably as a result of initial selection process in the pre-biological or early biological stages^[35]. Interestingly, this homochirality in the monomeric amino acid building blocks of proteins give rise to homochirality in higher-order structures such as the right-handed α -helix (secondary structure), and the fold (tertiary structure) that is unique to each different protein in its native state^[36] (**Figure 2**).

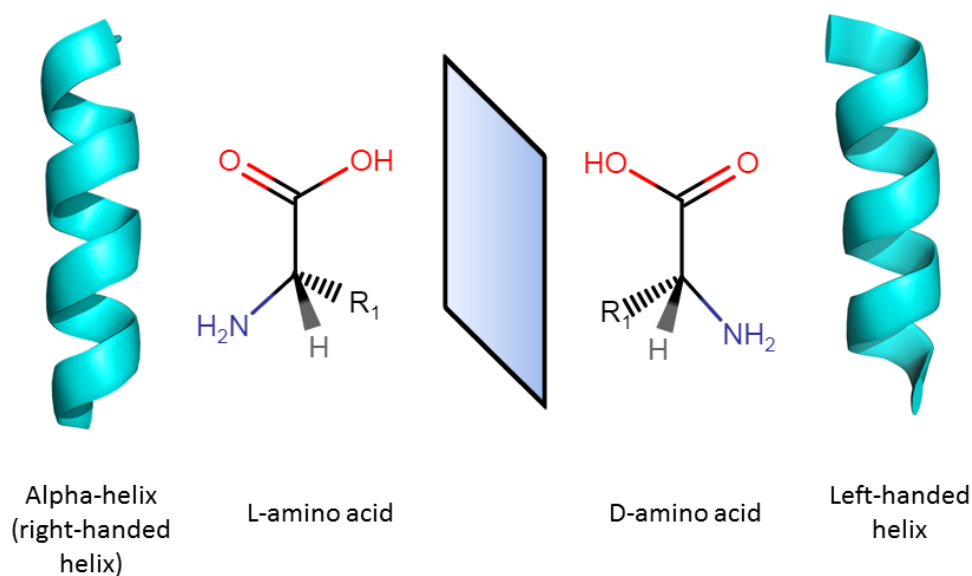


Figure 2. Nature chirality of amino acid building blocks of proteins (L-amino acids) together right-handed (alpha-helix) and its specular image (D-amino acids) together left-handed helix.

Chiral biomolecules then assemble to form cells and tissues, which further give rise to the asymmetric shapes or properties of natural biomaterials, for example, the specific rotation directions of shells, conchs, snails, and some flowers^[37,38].

1.5. From the Nature

Life requires three essential functions to be considered as such. It ought to have 1) the capacity of compartmentalization to isolate the cellular activity from the environment, 2) replication to transfer the heritable information to progeny, and 3) accomplishing metabolic functions to capture energy and material resources.^[39] In Nature, sophisticated organized functional macrostructures are formed through hierarchical self-assembly of simple molecules. The adaptive process has achieved to polish and improve along millions of years functions such as photosynthesis^[40,41], or electron transport chain^[42,43]. In addition, this adaptive process has also given rise to changes at microscopic level in the complex and hierarchical structuring of the insects and mammals epidermis. The latter mentioned cover a wide range of microstructures that play role in the micro- or macro-properties of the organism, including adhesion, anti-wetting, anti-reflectance and iridescence, are consequences of this particular structuring of the insect epicuticle^[44]. This microstructure provides an extra level of hierarchy which are mainly made up by proteins. For example, geckos have the ability to cling to walls and walk on ceilings. They owe this capacity to the microstructure and nanoscale attachment of fibrillar structures on its feet achieving extraordinary adhesion on surfaces. Van der Waals interaction are the driving force of the adhesion of any object to another. Thus, this fibrillar structure, that fall in the range of a few hundred nanometers to few micrometers, is the responsible for this outstanding adhesion due to the increasing of the effective area^[45]. These microstructures can adopt diverse geometries and morphologies providing unique functionalities. Spherical structures can be found in Nature as well. Brochosomes are granular microstructures, 200-700 nm in diameter, with hydrophobic hollow particles forming a truncated icosahedron. These structures distributed across the leafhoppers body allow them to repel water and thus protect them from getting trapped into water and their own liquids exudates^[46]. Another example of this hierarchical order in Nature is the abdominal segment of firefly lantern. The particular microstructure arrangement with a few hundred of nanometers of periodicity allows them to increase bioluminescent emission with high efficiency^[47]. Considerable interest in optics has the Tropical Morpho butterflies's wing which is very well-known for their iridescence. Iridescence is an optical phenomenon in which a pattern of color is observed in function of the viewing angle. The iridescence can be produced by light reflection or diffraction which ultimately leads to light interference, amplifying some wavelengths more than others. Butterfly's wing nanostructure has recently been resolved, showing a stacked lamellar

structure which is ultimately the responsible for white-purple iridescence as a result of light diffraction^[48] (**Figure 3**). In this section has been showed the large scope and relevance of proteins in Nature from nanoscale to microscopic and macroscopic level, following a well-defined hierarchical stratification. Thus, proteins can play role in nanotechnology as promising tools with applicability in diverse scientific fields such as photonics, catalysis, energy and related areas^[49] [47].

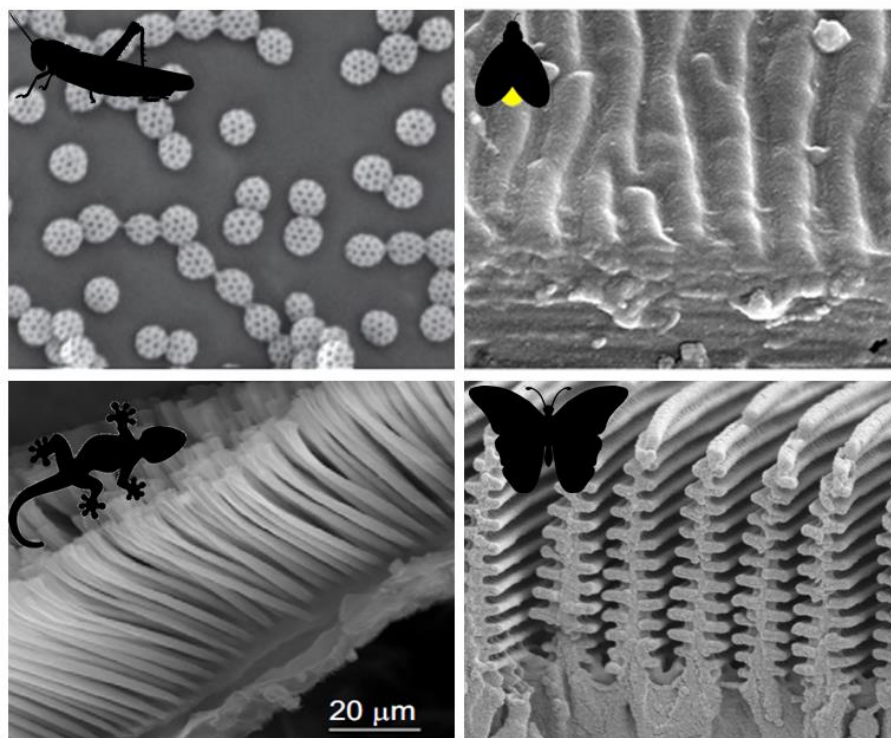


Figure 3. Microstructures commonly found in the Nature. A. Bronchosomes spheres of leafhoppers. B. Abdominal segment of firefly lantern. C. Fibrillar structure of Gecko's feet. D. Iridescent geometrical structure of Butterfly's wing. (Images from^[50-53])

1.6. Proteins as nanobiotechnology tool

During the last century, protein engineering or recombinant DNA technology has emerged as an useful tool for researchers. Recently, a growing number of new synthetic proteins and macrostructures based on proteins have been produced with the aid of rational design and computer modeling^[54-56]. Inspired in Nature, bottom-up self-assembly of proteins have reached the gold age providing a myriad of functional macrostructures.

In particular, self-assembly of shape-ring proteins have turned out to be an ideal starting point to form tubular-shape structures. Shape-ring proteins have been engineered or chemically modify to induce self-assembly merely changing the nature interface. Such is the case of the bacterial

tRNA attenuation protein (TRAP), a thermostable protein consisting of 11 monomers. The structure form a ring which hole is around 2 nm of diameter. Using genetic engineer was possible to form a nanotube of 1 μm in length, just modifying sort of amino acids by cysteine in both face of the ring^[57]. Another ring-shape protein was chemically modified, via electrostatic interactions as driving force of the assembly, *i.e.* the stable protein 1 (SP1). In this case, the different monomers are self-assembled by means of electrostatic interactions promoted by aliphatic chains that contain two quaternary amines in the extremes. The addition of this linker induces the polymerization and tube formation^[58] (**Figure 4**).

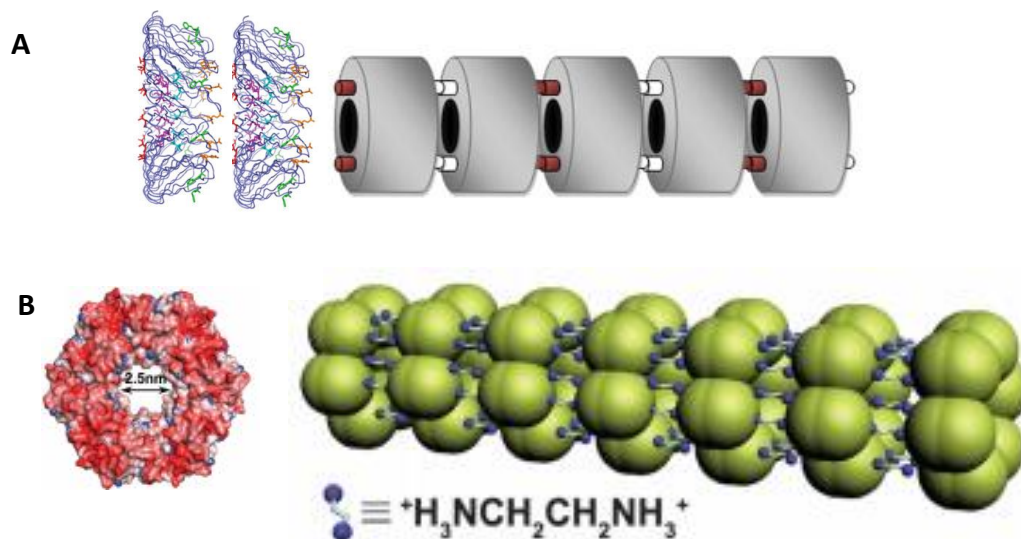


Figure 4. Protein assembly of protein ring-shape TRAP (A) and SP1 (B). (Figure from ^[57] and ^[58])

Currently, there is an increasing interest in the use of materials of biological origin and that can offer competitive properties respect to the synthetic counterpart, a part from biodegradability and biocompatibility features. In this regard, huge efforts have been done using distinct biopolymers as scaffold in the fabrication of new materials. However, the design of organized and self-assembled protein films is still an emergent field that pins down a further understanding and control of the intermolecular interactions. In the past decades, DNA has been the subject of depth studios in the design of molecular patterns, called DNA origami. Due to the predictable folding and easy design of the specific base pair interactions, DNA origami has led to the achievement of precise control at molecular level of the DNA assembly creating a vast range of nanostructures and patterns^[59,60]. In the same way, DNA has also been used to fabricate thin films, harnessing its optoelectronic properties, in applications such as organic light emitting diodes (OLEDs), solar cells

and optical amplifiers, among others^[61,62]. However, the chemical versatility and functionality, that proteins offer, cannot be overcome by other biomolecules.

In Nature, the assembly of proteins leads to hierarchically organized architectures that provide unique functionality to the material. Extracellular matrix (ECM), mostly composed of collagen, laminin, and fibronectin, has been widely employed as a tool in tissue engineering for medical applications due to biochemical, mechanical and organizational properties^[63,64]. Although, the complex tridimensional organization of the structural and functional molecules is not well-understood yet which makes its reproducibility *in vitro*^[65,66]. Nevertheless, individual components of the ECM are currently used in an effort to mimic these precious properties.

Collagen itself forms complex ordered structures. The intrinsic properties induce the bottom-up assembly provided by the internal and repetitive amino acid sequence (Pro-Hyp-Gly). Those induce triple-helix formation, and, in turn, the structure promotes the multi-hierarchical self-assembly to create nanofibrous strand. Finally, these strands continue to self-assemble linearly and laterally to give a hydrogel network. Inspired on this biological approach, a multi-hierarchical self-assembly hydrogel has been synthesized using a collagen mimetic peptide^[67] which opens the door for the design of new materials based on collagen assembly (**Figure 5**).

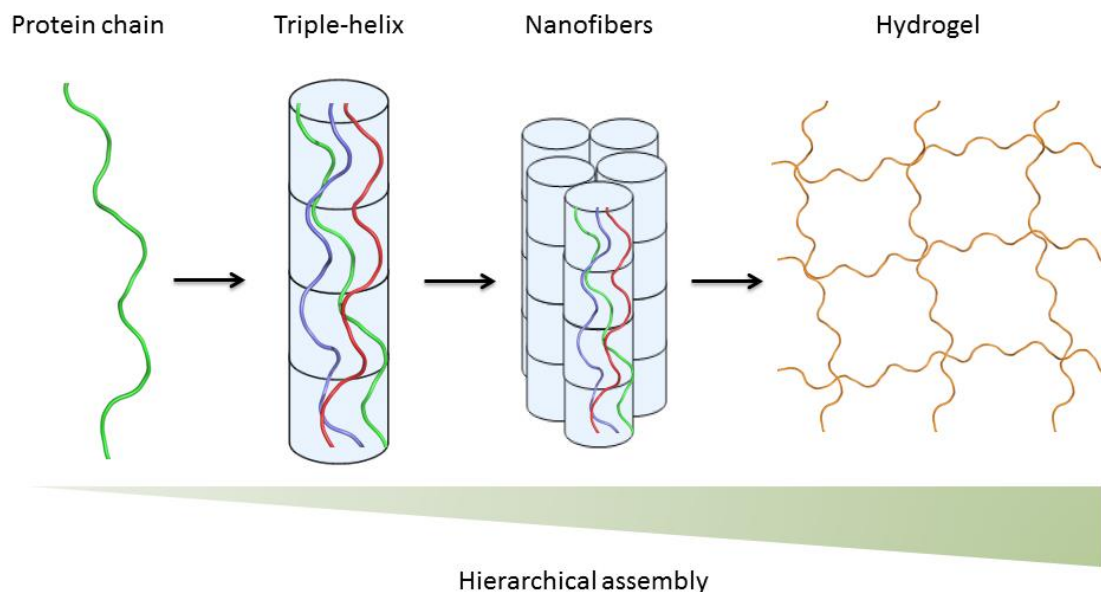


Figure 5. Schematic representation of collagen hierarchical assembly.

Elastin is another protein that belongs to the ECM and that has drawn attention to the researches because of its elastic and self-assembly properties. The fundamental building block of elastin is the tropoelastin which contains hydrophobic and hydrophilic domains that are arranged in alternating manner. Tropoelastin is self-assembled into elastin and, in turn, the elastin in elastic fibers. Their flexibility properties lie in the disordered nature of tropoelastin. Understanding the interactions that dominate in the natural materials has led to the design of a sophisticated range of designer proteins that have been used for a range of biomaterials with useful elasticity and cell interactive qualities^[68,69].

Silk proteins is another group of well-studied proteins, extract from different sources and that possess different properties in function of protein composition, mainly either fibroin (worm silk) or spidroins (spider silk). Silk-based materials have been widely used as bionanotechnology tools in biomedical applications, functional materials, and biocomposites as bulletproof vest, ropes, parachutes and coatings, because of outstanding mechanical properties, *i.e.* high tensile strength and extensibility^[70-72]. Also silk materials have widely been decorated with variety of molecules as metal particles and quantum dots for sensing applications^[73-75]. These exceptional mechanical properties lie in the specific arrangement of β -sheet, formed by repetitive motif, that ultimately allow a hierarchical organization^[76,77]. Additionally, these hierarchically organized structures have also been achieved *in vitro* in a straightforward manner, just under strict control of the evaporation conditions^[78,79].

Amyloidogenic proteins have also been described as a distinct approach to form hierarchical self-assembly nanostructured materials with remarkable mechanical properties. Amyloidogenic proteins are polypeptide molecules capable of self-assembly into β -sheet rich linear aggregates and, in turn, those form elongated fibrils that can be casted into thin films, forming ordered films in presence of plasticizing molecules^[80,81].

More recently, the rubredoxin, protein with redox properties, has been used for the biofilm fabrication, inspired in the architecture of bacterial electroactive biofilms. The self-assembly properties of rubredoxin generate organized films providing a suitable arrangement of the redox metal centers that permit electron transport^[82].

1.7. Repeat proteins

Genetic material duplication is a very common event in whole organism, especially in eukaryotic cells. It is believed that this phenomenon arises via intragenic duplication and recombination events. This duplication might vary from a single amino acid to the repetition of homologous domains of 100 or more residues and have diverse structures and functions. Most of the cases of amino acids of 1 or 2 repetitions usually lead to pathological situations as glutamine (Gln) in the huntingtin gene (resulting in Huntington's disease). However, large part of protein with repetitions of equal or more 3 amino acids give rise to stable proteins with specific structure (e.g. collagen). Repeat proteins provide certain evolutionary advantages of expanding the repertoire of cellular functions at energetic low cost and, therefore, playing a crucial roles in molecular recognition, signaling, protein transport or regulation of gene expression. Lots of repeat proteins have been described with different structure, function and phylogenetic distribution. Repeat proteins are usually classified attending to either their sequence motif length or tertiary structure. Among them, a particular family of repeat proteins attracts the attention since repetitive units are already large enough to fold independently into stable domains. This family of repeat protein, composed of multiple tandem copies of a modular structure, covers a broad range of proteins with different secondary structure elements that are interconnected to each other forming the base of the overall structure of the protein. In repeat proteins, these interactions between adjacent units define the shape and curvature of the overall structure^[54,83,84].

Thus, the differential packing arises from the secondary structure that, ultimately, impacts in the tertiary structure of the protein. Therefore, a protein as the Tetratricopeptide repeat protein (TPR) which consist of 34 amino acids and that fold in helix-turn-helix motif, gives rise to a right-handed superhelix structure. Whereas Ankyrin (ANK) repeats contain 33 residues forming a helix-loop-helix motif, and they form a left-handed twist of the stacking. Or in the case of Leucin-Rich Repeat (LRR) repeats which length vary between 20 to 30 amino acids and fold in a beta-turn-helix motif. The combination of this structural motif results in an arch shape with the β -strand and α -helix oriented in antiparallel manner (**Figure 6**)^[85].




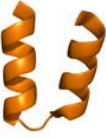




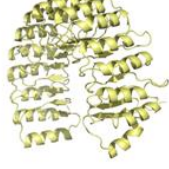
Repeat protein	Nº aa	Structural motif	3D structure (Lateral view)	3D structure (Frontal view)
TPR	34			
ANK	33			
LRR	20-30			

Figure 6. Structure of repeat proteins family (PDB ID: 1a4y (LRR), 4o60 (ANK), 2AVP (TPR)^[86-88]).

Their modular properties that stem from the particular and well-defined structure make them unique for their use in nanobiotechnology through a designable consensus sequence.

1.8. CTPR protein as ideal scaffold

TPRs have been widely used in protein engineering. Those repeat proteins consist of 34 amino acid sequence that folds in a helix-turn-helix motif (**Figure 6**). The main role of TPR proteins in Nature is associated with molecular recognition and mediate protein-protein interaction^[89,90]. Protein TPR domain has been described to interact with several protein and it is showed as domain almost ubiquitous present at many proteins in Nature. Hsp70/Hsp90 organizing protein (Hop) has three TPR domains which roles is to bind and arrange Hsp70/Hsp90 proteins^[91]. More recently, β -barrel assembly-enhancing protease A (BepA) has been described to have a TPR domain which is involved in the interaction with other proteins and that is essential for the BepA protein functionality^[92].

Consensus sequence design, *i.e.* the engineering of a protein composed of the most common residues at each position as determined from multiple sequence alignment of a group of sequences from a given family, has been a successful approach for generating proteins with a

specific fold. The best-studied consensus-designed repeat proteins are the consensus ankyrin repeats (DARPin^[93] or CARPs^[94]) and consensus tetratricopeptide repeats (CTPRs). In particular, CTPR emerges from the statistical analysis of TPR sequences and captures the sequence-structure relationships present in Nature (**Figure 7**)^[95].

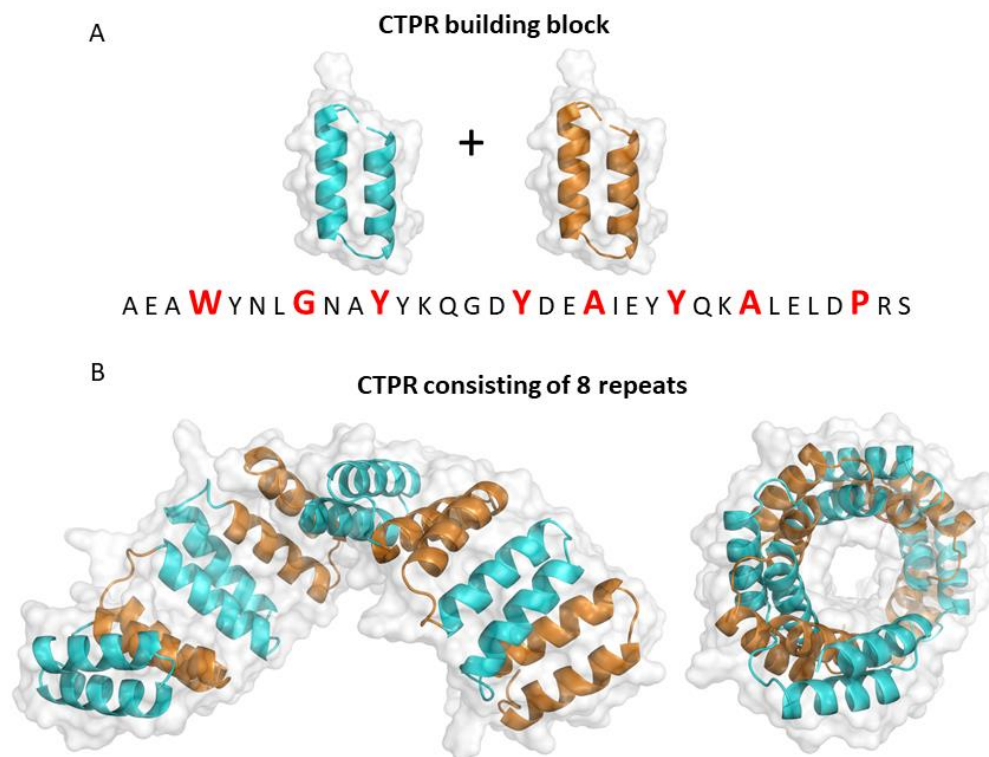


Figure 7. Consensus tetratricopeptide repeat (CTPR) protein. A. Structural motif of statistical CTPR sequence, showing the position highly conserved. B. Crystal structure of a repeat protein composed of eight repeats in lateral view (right) and frontal view (left) (PDB ID: 2AVP).

The CTPR building block is an idealized structural unit that can be combined in tandem to form superhelical arrays CTPR_n with n number of repeats. CTPR_n arrays form a continuous right-handed superhelical structure in which eight repeats comprise one full turn of the superhelix (**Figures 7**)^[96,97]. CTPR repeat is composed by only eight highly conserved small and large hydrophobic amino acids. These conserved residues are involved in intra- and inter-repeat packing interactions and thus maintain invariant the structure of the protein^[89,96,98]. Not conserved residues admit variations, even though there might be some constrains and preferences in terms of chemical nature and size at some positions, which ultimately might modify slightly the protein packing features^[88]. Thus, the protein structure permits some flexibility to design novel reactivities within

the protein by introducing mutations at many positions while still maintaining the TPR-fold. Using this approach, CTPR variants with different ligand-binding specificities have already been designed^[88,99–101]. Moreover, CTPR show higher stability compare with natural TPR^[95] which stability lie in intra and inter-repeat interaction and they can be modulated in a predictable manner^[102].

For all the above reasons, these features have opened the opportunity to tune the properties of the CTPR building block at will in order to use it as nanotechnology tools in many applications such as sensing^[103], biomedicine^[104] or electronic^[105,106], through organizing different molecules into the CTPR protein template.

Chapter 2

**Self-assembly of repeat proteins: Concepts
and design of new interfaces**

2.1. Background

2.1.1. Nanotubes based on proteins: previous work

Repeat proteins are an especially attractive target for nanotechnology applications due to their hierarchical and modular structures. In particular, consensus tetratricopeptide repeat protein (CTPR) consists of a 34 amino acids helix-turn-helix motif. CTPR repeats can be combined in tandem to form a continuous right-handed superhelical structure. As a result of that characteristic structure, CTPR proteins present geometrical and symmetric features that make them ideal for the design PNTs. Their modularity allows the engineering of novel interacting interfaces in straightforward manner, by introducing few mutations that will encode new interaction points that will be repeated along the protein. Those interaction points will result in a new interface that prompts the assembly a higher order stable structure.

In a first approach, prior to this thesis, it was explored the use of hydrophobic interactions as the driving force to lead the dimerization process^[107,108]. Thus, G15 and D31 were mutated to leucine (**Figure 1**). These modifications generated the novel hydrophobic interface that allowed the interaction between two CTPR proteins to assemble into a closed protein nanotube (**Figure 1**) that is energetically more favorable than the monomeric protein units^[109,110]. The G15L and D31L mutations were introduced at each of the 6 repeats in a CTPR6 protein to form the dimer named C6L (**Figure 1**).

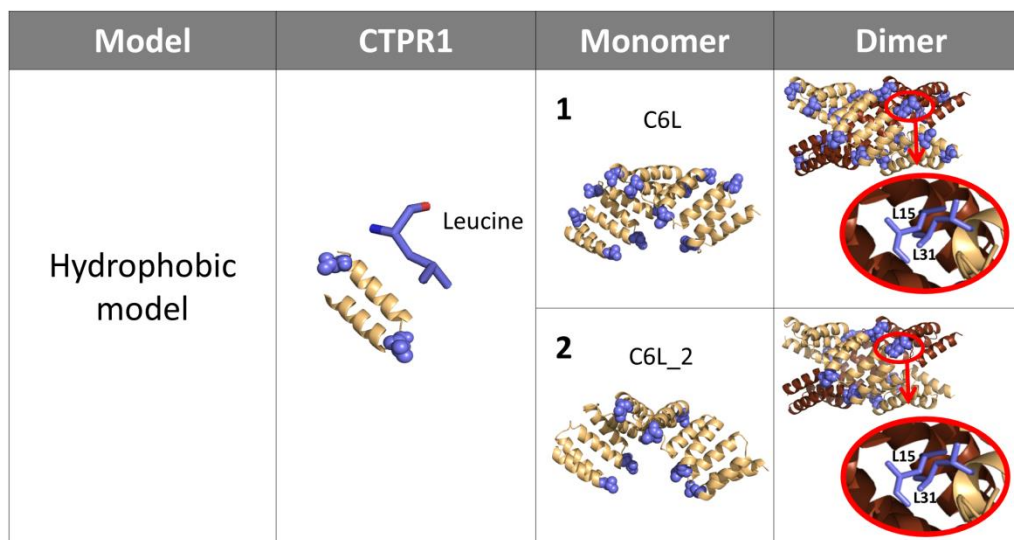


Figure 1. Hydrophobic model, based on hydrophobic interactions. The second column shows the modifications introduced in a single module (CTPR1), where the residues 15 and 31 are substituted by leucines. Column 3, construction of repeat proteins with 6 repeated units, based on the modules shown in the column 2. Column 4, dimer formation, the zoom-in images show the specific interactions that lead to the nanotube formation.

The designed C6L protein variant was purified in the presence of 0.2% of SDS to avoid precipitation. After protein purification, the sample showed two bands when is analyzed by 0.2% SDS acrylamide gel that correspond to the expected size of a monomer and a dimer: C6Ldimer (58926 Da) and C6Lmonomer (29463 Da) (**Figure 2A**). However, a native gel without SDS showed oligomers larger than expected for a dimeric nanotube, including trimers and tetramers (**A1-Figure 1**). The heterogeneity of the sample was further confirmed by TEM (**A1-Figure 2**). Using size exclusion chromatography in the presence of 0.2% SDS the monomer and dimer were separated (**Figure 2B**). Gel electrophoresis analysis of the FPLC fractions confirmed the presence of bands corresponding to dimeric and monomeric forms of C6L for the peaks eluted a 8.5 and 11 ml, respectively (**A1-Figure 3**). Additionally, mass spectrometry analysis of the higher molecular weight peak shows that is composed of C6L protein, ruling out the presence of a potential higher molecular weight contaminant in the sample (**A1-Figure 4**). The CD analysis showed that the C6L protein maintained the α -helical structure after SDS addition, as the C6Lmonomer and C6Ldimer have the same α -helical secondary structure as the CTPR6 wild type (**Figure 2C**). To characterize the stability of the sample, thermal denaturation was performed on the C6Ldimer and the C6Lmonomer samples. Comparing the thermal denaturation of these samples, similarly to what was observed in the electrostatic model, even if the mutations affected the stability of C6L when compared with the CTPR6 WT, the dimeric form is more stable than the monomeric form, indicating favorable interaction between the monomeric units (**Figure 2D**).

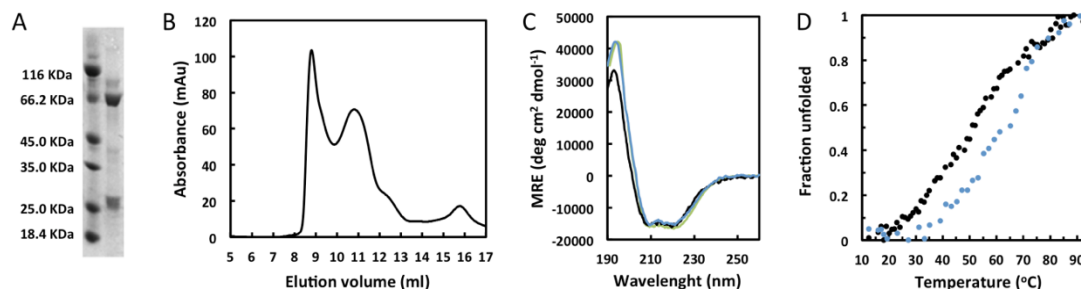


Figure 2. Characterization of the hydrophobic model (C6L) A. SDS-PAGE gel of purified C6L protein showing two bands that correspond to the monomeric and dimeric states. B. Size exclusion chromatography of C6L protein purified with 0.2% SDS over a Superdex 75 column. The chromatogram shows two main peaks corresponding to the dimeric and monomeric forms of C6L at elution volumes of 8.5

ml and 11 ml, respectively. **C.** Circular dichroism spectrum of the CTPR6 wild type protein in green, C6L_{monomer} in black, and C6L_{dimer} in blue. **D.** Thermal denaturalization of the C6L_{monomer} in black and C6L_{dimer} in blue.

The structure of the formed dimer was analyzed using TEM. Most of the molecules observed in the TEM images of the C6L_{dimer} sample have the expected size for the C6L nanotube (**Figure 3A**). The monomer population is likely to increase over time therefore the different characterization experiments must be done immediately after FPLC. To obtain a structural characterization of the formed dimer, a 2D classification is performed using the TEM images using CL2D classification (**Figure 3B**)^[112]. Also, from the predicted PDB model of the dimer (**Figure 3C**), theoretical projections of the dimer using EMAN software^[113] were performed taking into account the C2 symmetry (**Figure 3C**). The obtained projections were compared with the 20 classes obtained from the classification of the particles in the TEM images (**Figure 3D**). It was observed that the classes obtained from the images did not match well with the theoretical projections: 5/20 classes matched well with the theoretical projections (**Figure 3D/lined in green**); 8/20 matched partially with the theoretical projections (**Figure 3D/lined in orange**); and 7/20 did not match with any theoretical projection (**Figure 3D/lined in red**). Taking into account these results, it was not possible to conclude that the dimer obtained has the expected structure of the designed nanotube.

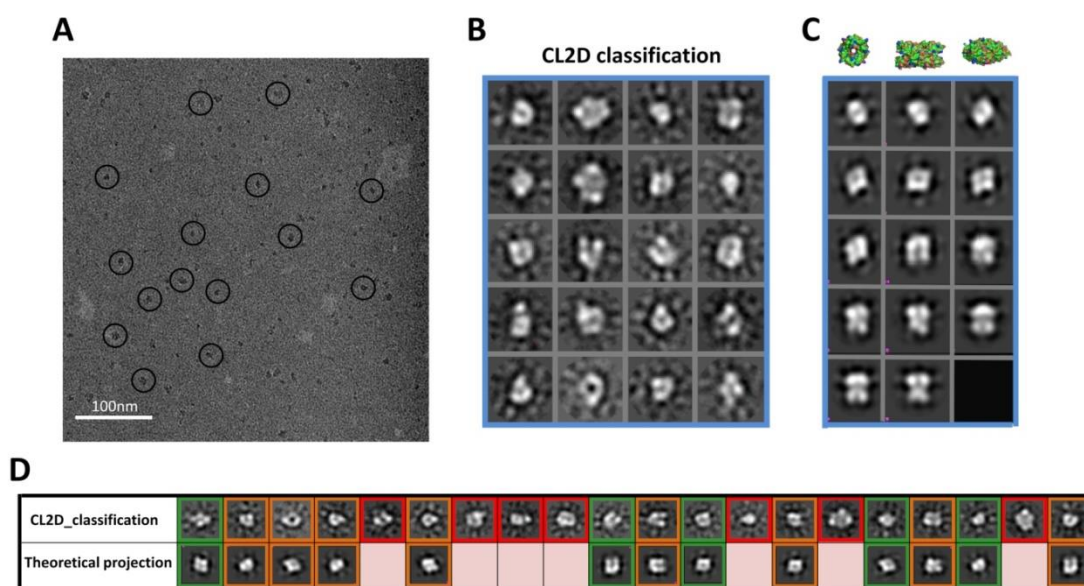


Figure 3. TEM characterization of the C6L_{dimer} sample. **A.** General TEM image of the C6L_{dimer} where it is expected to have the nanotube structure. The protein is negatively stained with uranyl acetate. The particles highlighted with black circles are some of the molecules in the TEM images which their sizes correspond to the size of a C6L designed dimer. **B.** 20 classes obtained by CL2D classification obtained from 2893 particles selected from different TEM images. **C.** Theoretical 2D projections based on the PDB model of the designed dimer. On the top, three different orientations of the C6L dimeric structure showing the surface of the protein. **D.**

Comparison between the theoretical 2D projections and real classification obtained from the picked particles in the TEM images. In green are highlighted the structures that are obtained in the classification of the particles of the TEM images that match with a theoretical projection based on the C6L designed dimer; in orange are highlighted the structures that are obtained from the classification of the particles in the TEM images that match partially with a theoretical projection based on the C6L designed dimer; and in red are highlighted the structures obtained from the classification of the particles in the TEM images that do not match with any of the theoretical projections.

The TEM characterization of the C6L dimers showed that there is a problem in the specificity of the nanotube formation. In addition, C6L formed oligomers larger than expected for a dimeric nanotube in absence of SDS, including trimers and tetramers (**A1-Figure 1**). In order to unravel the causes of heterogeneity in the C6L sample, docking was performed using *Cluspro* program. The docking results showed a large number of possible stable oligomeric conformations from the designed C6L monomer (**A1-Figure 5**). The unspecific interactions are likely to arise because some leucines of the designed hydrophobic interface are solvent exposed even when the nanotube is formed (highlighted with red circles in Figure 4A). Because of these leucines, the interaction between two monomers is not specific and different stable oligomers could be formed (**Figure 4B**) which are energetically more favorable than the designed nanotube (**Figure 1**). This result agrees with the large multimeric structures shown by TEM before adding the SDS and in the native gel (**A1-Figure 1 and A1-Figure 2**). Once 0.2% of SDS was added, the weak hydrophobic interactions are disrupted, and only dimers were obtained. However, the dimers obtained can adopt different dimeric conformations (**Figure 4B**). This result explains why the theoretical projections of the model do not agree with the classes obtained from the TEM images analysis (**Figure 3D**).

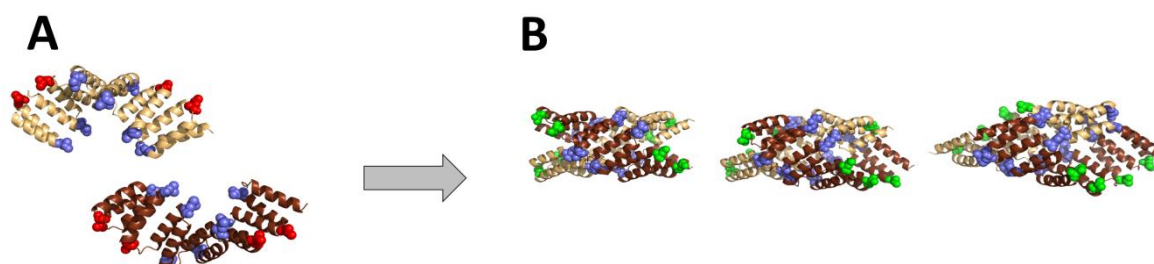


Figure 4. Potential dimeric nanotube structures from the C6L designed model. A. C6L protein design highlighting in red the leucines of the generated novel interface that are solvent exposed when the nanotube is formed: L31 in the repeats 1 and 2 and L15 in the repeats 5 and 6. B. 3 different stable possible dimers. The leucines from the novel interface that are interacting are highlighted as blue spheres and the leucines from the novel interface that are exposed are highlighted in green. The two C6L monomers are colored in dark and light brown to distinguish one from the other, but they are identical.

Considering the potential problem described above in the previous design, a new model is redesigned in which the leucines that remain exposed when the tube is formed in the C6L model

are removed (**Figure 1**). The new design, C6L_2, was generated and it was expected to form only one dimeric structure avoiding the competition between different conformational states. After protein purification, an electrophoresis gel of C6L_2 protein showed two bands corresponding to a monomer and a dimer: C6L_2dimer (58710 Da) and C6L_2monomer(29355 Da) (**Figure 5A**). Size exclusion chromatography was used to separate the monomeric and dimeric species (**Figure 5B**). The CD spectra of the isolated forms showed that the C6L_2dimer and C6L_2monomer samples maintained the α -helical secondary structure when compared with the spectrum of the CTPR6 wild type protein (**Figure 5C**). In the thermal denaturation, it was observed that in this case the stability was not very different between the monomers and dimers but the dimeric conformation showed slightly higher cooperativity than the monomeric conformation (**Figure 5D**). Purified C6L_2dimer were diluted and run on an electrophoresis gel. Similarly to the C6HD design, the dimer can be dissociated into the monomeric form upon dilution. From this study, an apparent K_d of about 1.5 μM could be estimated for the dimer dissociation (**A1-Figure 6**).

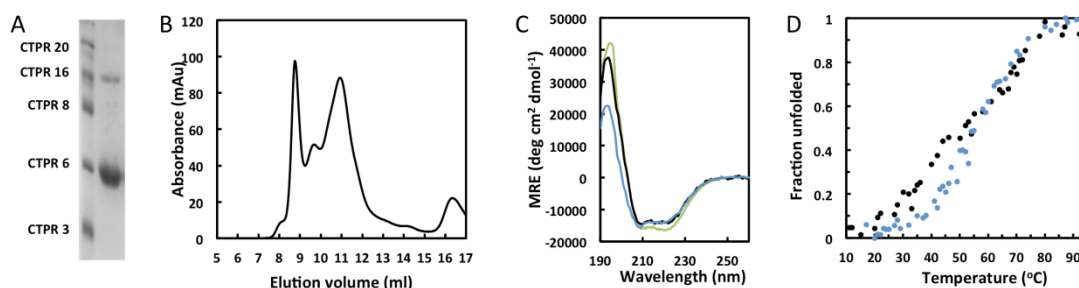


Figure 5. Characterization of the second generation hydrophobic model (C6L_2) **A.** SDS-page gel of purified C6L_2 protein showing two bands that correspond to the monomeric and dimeric states. In lane 1, a mixture of CTPR wild type proteins of different repeats as a marker is used. **B.** Size exclusion chromatography of C6L_2 protein over a Superdex 75 column. The chromatogram shows two main peaks corresponding to the dimeric and monomeric forms of C6L_2 at elution volumes of 8.7 ml and 11 ml, respectively. **C.** Circular dichroism spectrum of the CTPR6 wild type protein in green, C6L_2monomer in black, and C6L_2dimer in blue. **D.** Thermal denaturation of the C6L_2monomer in black and C6L_2dimer in blue.

However, C6L_2dimer could not be obtained upon concentration of purified monomeric form (data not shown) indicating that the dimeric form needs to be produced when expressed inside the bacteria. In order to structurally characterize the sample, TEM images of the C6L_2dimer were acquired. In the TEM images most of the molecules have the expected size for the C6L dimeric nanotube in the presence of 0.2% SDS (**Figure 6A**). From the TEM images some particles were selected and compared with theoretical projections expected for a C6L nanotube (**Figure 6B**). Most of the selected particles matched with the theoretical projections, suggesting that the

nanotube with the conformation expected from the design model might be formed. However, TEM images also showed that in addition to the dimeric conformation there were other higher order oligomeric structures present in the samples, probably due to the non-specificity of the strong hydrophobic interactions.

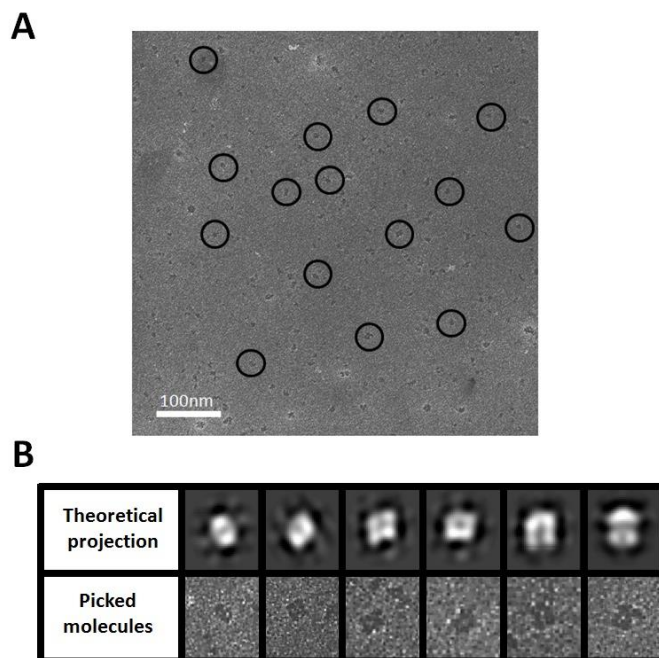


Figure 6. TEM characterization of the C6L₂_{dimer}. **A.** General TEM image of the C6L₂_{dimer} sample at 0.8 μ M. The proteins are negatively stained with uranyl acetate. The particles highlighted with black circles in the images are some of the particles with sizes that correspond to a C6L designed nanotube conformation. **B.** Matching between the theoretical 2D projection based on the PDB of the designed dimer, on the top, and the structure of some molecules picked from the TEM image, on the bottom.

Considering this previous model using the hydrophobic interaction as driving force of the assembly, we designed two new approaches based on electrostatic and aromatic interaction as driving force with the aim of having a better understanding and control of the self-assembly, and overcoming the drawbacks concerning non-specific interactions which gave rise to oligomerization process.

2.2. Introduction

2.2.1. Higher-order protein assemblies: natural and designed

2.2.1.1. Relevance of protein assemblies in Nature

Nature displays multiple examples of proteins that have evolved to generate combinations or assemblies of smaller independently folded domains^[117–119]. Myoglobin, the first protein whose structure was determined more than half a century ago by Max Perutz in 1959^[120], is a monomeric heme protein very similar to hemoglobin. For its physiological and historical relevance, hemoglobin is an example of an oligomeric protein in Nature assembled from four globular subunits. Since then, many proteins have been shown to permanently (e.g. collagen) or transiently (e.g. G proteins) form oligomeric complexes for function. Proteins self-assemble into multi-subunit complexes such as viral capsids, stabilized by interactions between subunits, or bacterial flagellum, a complex molecular machine assembled from more than 20 different proteins^[121,122]. Studies estimating the natural occurrence of oligomeric proteins in *Escherichia coli* indicated that dimers and tetramers are by far more common than other oligomers, and monomers are in the minority, being only about one fifth of the protein species in the whole cell^[123]. Since oligomeric proteins are prevalent in Nature, protein oligomerization may often be an advantageous feature from the perspective of protein evolution^[124].

The basis of oligomerization has been deeply studied and its biological significance is of the utmost importance. Protein-protein interactions may occur between different or identical chains and may confer structural symmetry. Monod already classified homo-oligomers based on the mode of their interactions as isologous or heterologous, giving rise to dimers with 2-fold symmetry or higher oligomers, respectively^[125], introducing the symmetry concepts. More recent classifications separate oligomeric states between non-obligate or obligate, transient or permanent, according to biological function, or classify the protein-protein interactions into six types of interfaces (intra-domain, domain-domain, homo-oligomers, homo-complexes, hetero-oligomers and hetero-complexes) which differ in both their amino acids composition and residue-contact preference^[126].

Many studies have analyzed the characteristics of protein-protein interactions to characterize how structural geometry and chemical complementarity contribute to the affinity and specificity of the interacting proteins^[127–131]. Some of those studies have been focused on residue composition at different interfaces, pointing out that hydrophobic and aromatic residues are more frequent and hydrophilic residues are less common. Other studies have taken solvent accessibility of the interface into account, which turned out to be relevant for the residues distribution along the interface^[132].

As mentioned above, the symmetry plays a crucial role in order to understand protein-protein interactions. It is worth noting that symmetry is the rule rather than the exception for proteins. Therefore, most of the oligomeric proteins found in living cells have symmetry: bacterial S-layer proteins assemble into oblique, square, or hexagonal planar symmetry^[133,134], gap-junction plaques display hexagonal planar symmetry^[135], water channels have square planar symmetry^[136], viral capsids display helical or icosahedral symmetry^[137,138], and even the most simple oligomeric proteins like human serum amyloid P-component show pentagonal symmetry^[139]. Thereby, symmetry is a highlight tool to design large and regular macrostructures.

2.2.1.2. Designed assemblies: relevance in applications

The modular assembly of higher-order structures using nanoscale globular building blocks is a fundamental aspect of molecular biology. A bottom-up approach enables to mimic the hierarchical organization observed in Nature, enabling the design features of small and simple elements to impart structural features more complex composite structures^[140–142]. Self-assembly is a spontaneous process of organization of molecular units into ordered structures as a result of intra- and inter-molecular interactions^[143], and relies on highly specific biomolecular interactions. Thus, bottom-up approaches based on these interactions provide attractive strategies to design complex structures from simple molecular units^[144]. This approach represents an extraordinary source of innovation with strong potential impact in material sciences^[145].

Currently, the rational design and controlled assembly of biomolecules is the state-of-art in nanobiotechnology, mostly based on DNA origami. DNA is an excellent building block owing to its high chemical stability, predictable folding and easily controllable assembly properties through rational design^[80]. The great potential of DNA architectonics is reflected by the variety of two and

three-dimensional shapes and patterns with sizes from 20 to 200 nm^[60,146,147]. However, functionalization of nucleotide-based nanostructures is still challenging^[148]. Apart from DNA, although less used, RNA has been used to generate 1D and 2D shapes due to the higher rigidity of its structural motifs^[149].

Similarly, the use of peptides as building blocks for their assembly into larger structures is quite extensive. Peptides are very interesting building blocks for the engineering of self-assembled structures because of their versatility in terms of modularity, responsiveness to stimuli, and functional diversity. Peptides have been widely used in order to create nanostructures^[150,151] and functional biomaterials^[152–155], including fibers, tapes and hydrogels^[156–161]. In this sense, most of the examples are related to fibrillar structures. Filamentous assemblies are usually classified into two main groups: α -helix-based and amyloid-like assemblies. On one hand, the designs based on interactions of alpha-helical peptides are usually obtained from *de-novo* sequences. The sequence-to-structure relationship tends to be better defined for these kinds of assemblies. On the other hand, the designs based on amyloid-like peptides can be obtained from naturally occurring and designed sequences^[80]. The design of amyloid-like fibers relies on the general tendency of β -strands to aggregate. There are few examples in which interactions at the molecular-level can be extended to a macroscopic material using these assemblies^[80]. The downside of amyloid-like assemblies is that the assembly is not specific and cannot be modified in a controlled way since all the sequences generate similar assemblies. It is worth mentioning that short α -helical coil-coiled peptides have been used to assemble cage-like particles by means of rational design strategies, encoding specific protein-protein interactions^[162].

Looking at the complexity and sophistication of protein-based structures and materials in Nature, proteins have long been recognized as the most versatile of the biological building blocks with a great potential for material and nanostructure engineering^[141,142,160,163]. Fegan et al. analyzed the role of protein assembly in biological structures to suggest tools to use in the 1-100 nm size range, which is too large to fill with synthetic organic chemistry but too small for the techniques of microfabrication^[164]. Moreover, several recent reviews give an overview on the rational engineering of protein assemblies for nanotechnology^[165–168]. The field focuses on the understanding of the design principles inherent in natural proteins and how these might be exploited to fabricate different structures by bottom-up approaches for different applications in

nanotechnology for biomaterial design, biocatalysis, and synthetic biology. For example, rods and cylinders offer a potential for formation of gels and films, as well as components of motors or nanodevices associated with transport and motility. Closed hollow assemblies afford encapsulation, compartmentalization, and protection from the environment, potentially with controlled release. Planar assemblies suggest applications in protection, molecular filtration, and immobilization of useful functionalities such as enzymes.

Lately, increasing efforts are being invested in designing *de novo* protein-protein association to create new nanoarchitectures from proteins. The analysis of natural interfaces between proteins has established the formulation of some generic rules that govern these associations. As an example, Grueninger et al. in 2008 produced a number of novel assemblies, demonstrating that a given protein can be engineered to form contacts at various points on its surface, resulting in different oligomeric states^[169]. From these results, it was concluded that symmetry is a fundamental factor in protein association because it enhances the multiplicity of the designed contact and therefore minimizes the number of required mutations. Moreover, it was observed that the mobility of the side-chains responsible for the interaction is an important factor in contact design. This work demonstrated that the production of particular contacts is feasible, whereas high precision seems difficult to achieve and provides useful guidelines for the development of future architectures.

Recently, our understanding of how to manipulate the structure of the proteins to create artificial constructs with properties has increased exponentially^[170]. As the understanding on the self-assembly of proteins is growing, the interest of using self-assembling protein-based materials in biomedicine and nanotechnology is progressively increasing, with potential applications as matrices for tissue engineering, drug-delivery systems, sensors, storage devices, and catalysts^[141,171–173]. However, the application of these materials requires good control over self-assembly and material properties. Self-assembly approach has been shown useful to form large nanometric fibers as well as materials such as organized films, lattices with different geometries, and 2D and 3D arrays^[174–178]. The development of computational protein-protein design, the consideration of symmetry concepts and bottom-up self-assembly approaches have given rise to successful generation of protein-based structures with complex symmetries from protein design perspective^[179–181].

However, in contrast to simpler building blocks, such as DNA, RNA and peptides, protein assembly has not been able to fulfill the expectations generated, because of its greater structural complexity and chemical heterogeneity. In spite our increased understanding of interactions that govern assemblies in Nature, in the laboratory it is still a challenge to design proteins that assemble into specific, well-ordered arrays and to make controlled assemblies that span scales over several orders of magnitude^[161].

2.2.2. Repeat proteins: ideal scaffold for protein engineering

The main limitation in the rational protein design is the limited understanding of how protein sequence-structure-function relate. Thus, it is critical to understand the fundamental principles that underlie protein structure, stability and function, and how the structure and function of the proteins are defined by their sequence. In this sense, repeat proteins are interesting scaffolds for protein design because of the simplicity of the system. Repeat proteins are non-globular structures involved in essential cellular processes acting typically as scaffolds to mediate protein–protein interactions. Repeat proteins are composed of a varying number of tandem repeats of a basic structural motif of 18 to 47 amino acids, and their structure is dominated by short-range and regular interactions^[117,182]. Repeat proteins are classified in several families attending to their characteristic signature sequence. LRR (Leucin-Rich repeat), Armadillo (ARM), Ankyrin (ANK), and TPR (tetratricopeptide repeat) are the most studied so far. The modular structure of repeat proteins simplifies the design problem to the level of simple units and to the interactions between the neighboring units, which are local and predictable. Each repeat unit can be used as a building block with individually engineered properties, including stability^[183,184], function^[185–188], and interactions between modules. The understanding and control of the structure and stability of the repeat proteins open the door to use them as scaffolds to generate self-assembled functional structures^[189–191]. Considering the previously described main features of repeat proteins, it is evident that they are ideally suited for protein design and nanobioengineering through modular approaches^[192,193]. Indeed, some recent works confirm the level of understanding of those repeated systems where a rational computational design can be used to engineer proteins with different properties that expand the sequence and structure space observed in Nature^[194–196].

We work on a particular type of repeated unit, the tetratricopeptide repeat (TPR). TPR consists of a 34 amino acid helixA-turn-helixB motif (**Figure 7A**)^[197]. In Nature, TPRs occur in tandem repeat arrays from 3 to 20 repeats to mediate protein-protein interactions in cells and to assemble multi-protein complexes. A consensus TPR (CTPR) sequence was previously designed from the statistical analysis of natural TPRs (**Figure 7A**)^[198]. CTPR sequence includes few highly conserved small and large hydrophobic amino acids, which are involved in the intra- and inter-repeat packing interactions that define the TPR fold^[197,199,200]. At the other positions the sequence is not conserved and can therefore be varied for design purposes^[186,201]. CTPR repeats can be combined in tandem (**Figure 7B**) to form CTPR proteins that present a continuous right-handed superhelical structure with eight repeats per one full turn of the superhelix (**Figure 7B**)^[198,202].

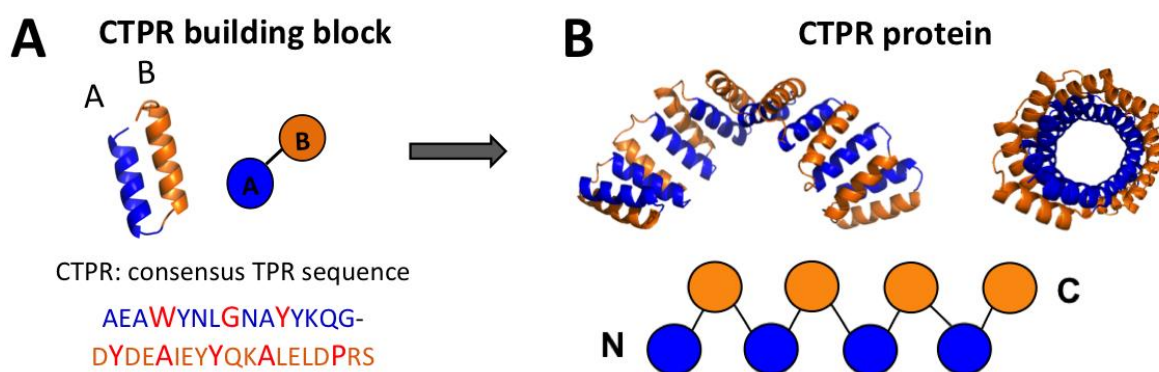


Figure 7. CTPR units as building block for repeat proteins. **A.** CTPR unit structure is represented showing helix A in blue and helix B in orange. On the right, a schematic representation of the structure of the CTPR building block using the same color code. Below: the consensus CTPR sequence with the conserved amino acids highlighted in red. **B.** The crystal structure of a repeat protein composed of 8 CTPR repeats (PDB ID: 2AVP) with A helices colored in blue and B helices in orange. Side and axial views of the CTPR8 are shown. Below: the schematic representation of the CTPR packing from N-terminal to C-terminal.

2.2.3. Protein-based nanotubes

Nanobiotechnology is an emergent field that stems from the intersection of biology and nanotechnology in order to study biological systems at the nanoscale and to design nanoscale structures and materials based on biological components^[203]. The self-assembly of atoms or molecules into more complex higher ordered structures is known as “bottom-up” approach, whereas “top-down” approach refers to nano/microfabrication technologies to fabricate nanostructures and nanodevices^[204].

Typically, self-assembly involves the arrangement of atoms and molecules in a specific way to form a defined structure. In the same manner, biomolecules, including nucleic acids, lipids, peptides, and proteins, can act as building blocks to the self-assembly of higher order structures. The chemico-physical characteristics of nucleic acids enable the precise control of the assembly through robust and predictable base-pair interactions to build structures with precisely control geometries, such as DNA origami nanostructures^[60]. Therefore, it is no surprise that DNA was the first biological molecule to be implemented in nanotechnology, and the great potential shown by DNA origami technology^[205–208]. Similarly, lipids have also arisen as robust tools in nanotechnology given their self-assembly properties that enable the easy formation of nano-films and other structures such as micelles or liposomes^[209]. Most recently, peptides, and proteins are emerging as tools for applications such as tissue engineering, drug delivery, wires for bio-inspired nano/microelectronics, and the development of biosensors^[210–212].

The driving force of self-assembly in protein-based systems is led by non-covalent interactions, *i.e.* hydrogen bonds, electrostatic, hydrophobic, and van der Waals interactions. Although those bonds are relatively weak, the total number of bonds engaged in the interactions result in stable structures. In Nature, those weak bonds are responsible for many interactions in biological systems and promote self-assembly of a vast range of protein structures.

Nanotubes are nanometer-sized tube-like elongated nanostructures that have a defined inner cavity. Nanotubes are attractive because of the large internal surface area and confined inner cavity that provide potential for application in filtration, encapsulation and release of small molecules or drugs^[213,214], catalysis due to the increased local concentrations^[215], optics and electronics^[216,217], among others.

A number of protocols have been reported for the preparation of the non-covalently self-assembled nanotubes using different structures including rod-like units, helical structures, and stacked rings. Up to the date, Fmoc-dipeptides^[218], cyclic β -sheet stacking peptides^[219], lock-washer α -helical bundles^[220–222] and short peptides that self-assemble into spiral tapes^[223,224] have been used as building blocks for nanotubes. Also, recently a generic modular approach to assemble nanotubes from α -helical barrels (α HBs) has been presented^[225–227]. Moreover, recently

systems with tailored inner diameters via the ring size of the peptide have been assembled through the self-organization of β -sheet stacking peptides^[216,228].

Protein-based non-covalent nanotubes have become a subject of major interest due to their properties including facile synthesis, self-organization, and potential control of diameter and size. The potential use of protein nanotubes (PNTs) has great relevance and interest in many applications due to their well-defined structures, assembly under physiologically relevant conditions, and manipulation through protein engineering approaches in addition to biodegradability and biocompatibility^[229].

The design and production of PNTs is still rather challenging given the high complexity of protein folding, the lack of understanding of the sequence-structure relationships in proteins, and even more limited knowledge on the design of novel interfaces. In this sense, various structures from Nature have been used as starting point to develop higher order structures^[230]. In general, these naturally occurring structures consist of ring-shaped monomers, which structure can be redesigned either chemically or genetically engineered to promote their oligomerization, such as RubisCO, trp tRNA-binding attenuating protein (TRAP), *Pseudomonas aeruginosa* Hcp1, stable protein 1 (SP1), and the propanediol-utilization microcompartment shell protein PduA^[231–237]. Recently, alternative approaches have been employed for the design of PNTs. All those have in common the use of proteins which structures enable the precise control of the assembly given their modularity and predictability^[238,239].

Although these works represent an improvement on the control of the biomolecule-based nanotubes formation, most of them used small peptides as building blocks or the stacking of performed ring-shaped proteins. However, there are no significant works in which proteins are applied as molecular units to generate synthetic PNTs. Proteins provide more versatility than peptides, giving the opportunity to expand the applications of the formed nanotubes. In this chapter, we describe the use of repeated CTPR proteins to engineer PNTs by the engineering of novel interacting interfaces at the molecular level. The high symmetry and the modularity of CTPRs permit the design of few contact points that will be extended along the structure for the generation of repeated interacting interfaces. Those interfaces will result on the assembly of stable higher order structures.

2.3. Experimental section

2.3.1. Protein design, molecular engineering, and protein purification

Considering the geometry of the right-handed superhelical structure of CTPR proteins a three dimensional model was generated by manually docking two superhelical CTPR proteins in a parallel orientation form a closed nanotube using Pymol (**Figure 8 and 9**). By detailed inspection of a model that did not show any clashes, two positions were identified in a repeated CTPR unit as the ones that contact repeats from the other CTPR molecule in order to form a closed the nanotube. Those contacts points are located at the two loops in the CTPR repeat at positions 15 and 31 and were selected as the candidates for the generation of the new interfaces. Contacts between position 15 and 31 are extended along the CTPR super helix creating a new interacting interface. The design models for CTPR nanotubes based on electrostatic and aromatic interactions are all based on the design of complementary amino acid pairs at these positions.

Two models were designed to be tested experimentally: An electrostatic model containing interacting aspartic acids and histidines and an aromatic containing interacting tyrosines. Based on a consensus CTPR protein with 6 repeats (CTPR6), single point mutations were introduced depending on the model used. For the electrostatic model, a histidine was introduced in each repeat at position 15 for its interaction with the aspartic at position 31 obtaining C6HD protein. Finally, for the aromatic model, the protein was generated by sequential additions of CTPR1 modified repeats, where the repeats 1 and 2 have only one mutation D15Y; the repeats 3 and 4 have mutations G15Y and D31Y; and the repeats 5 and 6 have one mutation D31Y, generating the C6Y protein.

Single point mutations for each model were introduced in CTPR1WT by quick-change site-directed mutagenesis. The modified CTPR6 genes were generated from the CTPR1 mutated genes by sequential additions of mutated repeats and cloned into pPro-EX-HTa vector. The generated genes were transformed into *Escherichia coli* C41(DE3) and a single colony was used to inoculate an overnight culture of 10 mL of fresh LB medium containing 100 µg/mL of ampicillin and then grown overnight at 37°C in a shaking incubator. 5 mL of overnight culture was used to inoculate 1 L of fresh LB medium containing 100 µg/mL of ampicillin. When the culture reached an optical density of 0.6-0.8 at 600 nm, the expression was induced with isopropyl β-D-1-thiogalactopyranoside (IPTG) (final concentration 0.6 mM). Protein expression was performed

during 5 hours at 30°C. The proteins were purified using standard affinity chromatography methods based on previously published protocols^[199]. The protein samples were dialyzed into PBS (150 mM NaCl, 50 mM phosphate buffer pH 7.4) and were stored at -20°C. The protein concentration was determined by UV absorbance at 280 nm using the extinction coefficient calculated from the amino acid composition^[240].

2.3.2. Gel electrophoresis

SDS-PAGE was performed using 15% acrylamide gels on kuroGEL Verti 1010 electrophoresis system. Identical setup was used for native PAGE, except SDS was withheld. The gels were stained with Coomassie blue.

2.3.3. Size exclusion chromatography

Gel filtration chromatography was performed using an AKTA prime plus Fast Protein Liquid Chromatography (FPLC) equipment (GE Healthcare). The samples were injected into a Superdex 75 HR 10/30 size exclusion chromatography column (GE Healthcare) and ran at 0.5 mL/min in PBS at 4°C. The purified samples were collected in 0.5 mL fractions and stored frozen at -20°C.

2.3.4. Circular dichroism (CD) measurements

CD spectra were measured using a Jasco J-815 CD Spectrometer. CD spectra of the samples in PBS buffer were acquired in a 1 cm path length quartz cuvette. All CD spectra were recorded with a band-width of 1 nm at 1 nm increments and 10 second average time.

Thermal denaturation was performed in a 0.1 cm path length quartz cuvette in PBS. The denaturation curves were monitored by following the CD signal at 222 nm wavelength as a function of temperature from 10°C to 95°C. CD experiments on monomeric and dimeric samples are performed right after FPLC purification and without dilution of the samples to ensure the stability of the forms.

2.3.5. Transmission electron microscopy (TEM)

The protein samples in PBS were deposited at 0.8 μM protein concentration immediately after FPLC purification on glow discharged Cu/Rh grids coated with carbon (Maxtaform Cu/Rh HR26), and negatively stained with 2% uranyl acetate. Micrographs were recorded using Kodak SO-163 film, in a JEOL JEM1200EXII electron microscope with a tungsten filament operated at 100 kV and

at 60 K magnifications. Micrographs were digitalized using a Photoscan TD Zeiss-Intergraph scanner (pixel size 2.33 Å/px).

2.3.6. TEM image processing, particle selection, and 2D classification

In all cases, the CTF (contrast transfer function) was corrected using the CTFFIND3 program^[241], which also calculates potential astigmatism. Micrographs with visible drift and astigmatism were discarded. Single particles were selected manually, extracted from micrographs and normalized using the XMIPP software package^[242]. Two types of algorithms implemented in XMIPP were used to classify single images: ML2D^[243] and CL2D^[112]. In the main text, CL2D classification is presented.

For the theoretical projections of the C6Y dimer based on the PDB of the model structure of the designed protein, pdb2mrc, a program from EMAN software package was used to generate a 3D electron density map from the PDB file. Then EMAN software was used to perform the projections^[113].

2.3.7. Computational analysis based on docking simulations

Computation analysis was carried out in order to verify all the possible interactions between the designed interfaces with the purpose to find a free-energy minimum for the complex that displays a nanotube structure as expected from the initial designs. The models proposed were evaluated using *RosettaDock* and *ClusPro* server in order to perform a local docking search. Each server applies a specific analysis program using different search algorithm, *ClusPro*^[114] based on fast-Fourier transform methods for grid matching and *RosettaDock*^[244] is based on Monte Carlo algorithm. Therefore different outputs may be obtained for each case. According to the results, the proposed designs were accepted attending to the shape and energy stability of the complex formed for both docking analysis programs.

2.4. Results and Discussion

2.4.1. Nanotubes based on repeat proteins: concept and design

CTPR arrays contain multiple repeats that interact through a single inter-repeat interface to form elongated superhelices. In previous works, it was shown that it is possible to form higher order structures such as protein films^[175,176], nanofibers^[177,245] or protein monolayers^[190] based on CTPRs. In these works, the head-to-tail and side-to-side interactions observed in the crystallization of the CTPR proteins were used to promote the assembly of the protein units.

The work presented in this chapter goes a step further and aims to design PNTs by the introduction of a novel interaction interface between two CTPR proteins. The inter-repeat interface allows the interaction between two CTPR units in order to form a linear superhelical structure (**Figure 7B and 8A**)^[177,202]. In this work, we hypothesize that, if an additional interface is introduced in the repeated unit, a 3-dimensional structure will be formed by the supramolecular assembly of two CTPR superhelices (**Figure 8B**), as previously proposed by Nussinov and coworkers^[109]. Since there is a twist between consecutive CTPR repeats that defines the superhelical structure, the introduction of a second repeated interface along the CTPR superhelix would allow two superhelical CTPR molecules to assemble into closed protein 3D nanotubes (**Figure 8B**).

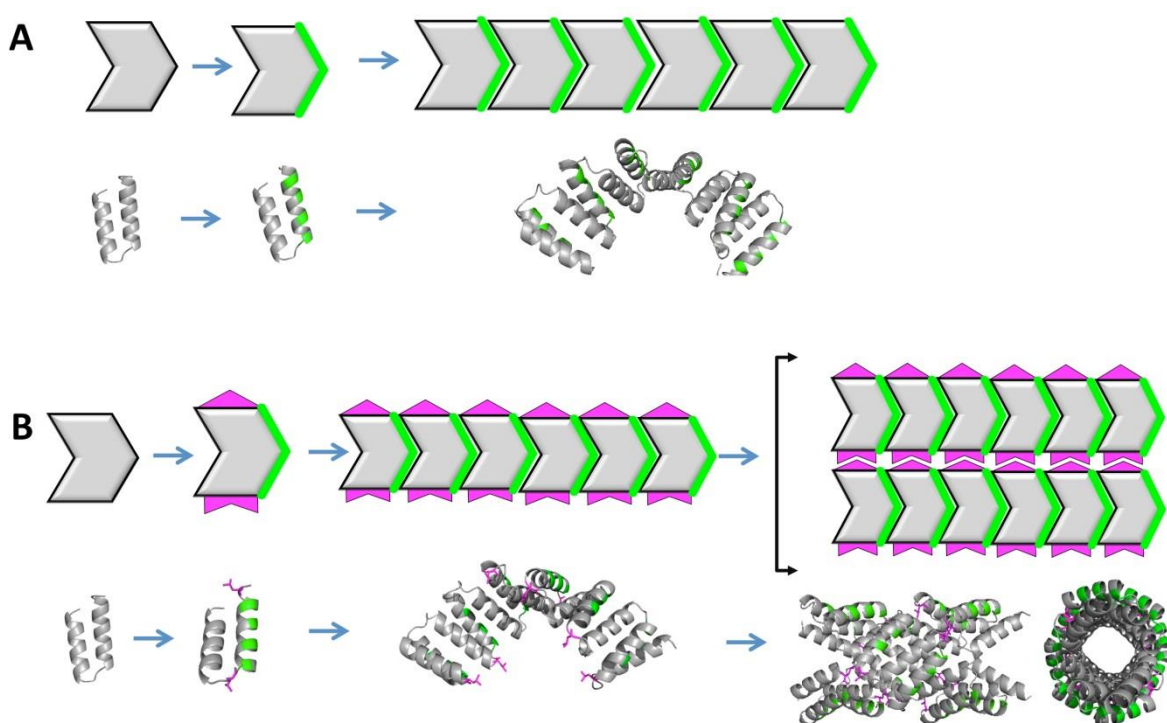


Figure 8. Schematic representation of CTPR proteins inter-repeat interactions. **A.** A single repeat interface in a repeat unit (green) leads to the formation of a linear structure. **B.** Repeat unit with two different interfaces (green and purple) for the formation of a parallel nanotubular structure. The crystal structure of the CTPR6 protein is shown and the nanotube model in both side and axial views.

A structure-based rational design approach was applied to engineer the novel interface. Based on the crystal structure of the CTPR protein, it is hypothesized that mutating the amino acids in the loop of the CTPR protein throughout all repeats in the superhelix, a novel interacting interface would be formed (**Figure 8**). A nanotube model was generated and the positions 15 and 31 located

at the loops were selected for the introduction of the novel interface. We explore two different approaches for the formation of the novel interface: an electrostatic model (**Figure 9A**), where the dimer formation is led by electrostatic interactions between an aspartic acid (negatively charged) and a histidine (positively charged); and an aromatic model (**Figure 9B**), where the dimer formation is led by π - π interactions using tyrosines.

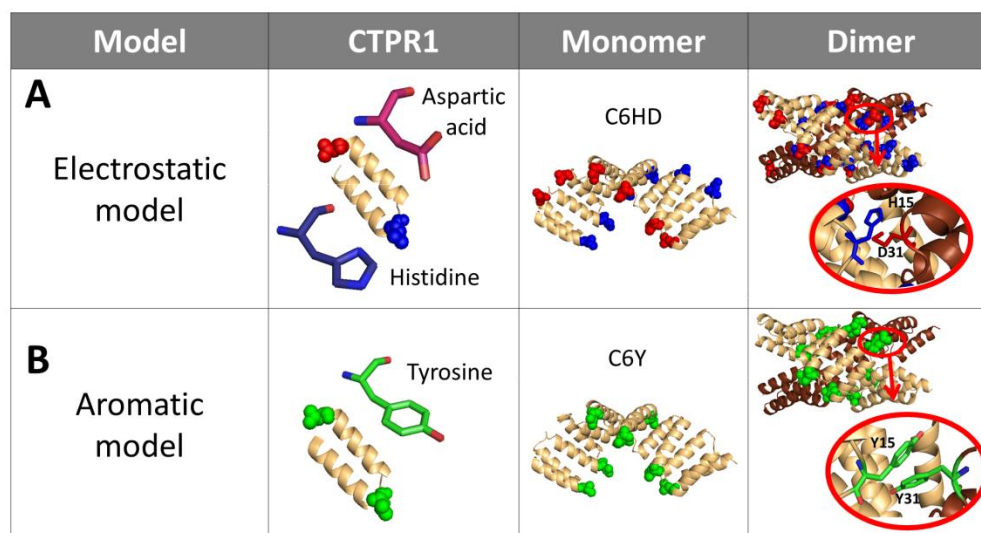


Figure 9. Different approaches for the design of nanotubes based on CTPR proteins. **A.** Electrostatic model, based on electrostatic interactions; **B.** Aromatic model, based on π - π interactions. The second column shows the modifications introduced in a single module (CTPR1), where the residues 15 and 31 are substituted by histidine and aspartic acid, respectively, for the electrostatic approach and by tyrosines for the aromatic approach. Column 3, construction of repeat proteins with 6 repeated units for the different approaches, based on the modules shown in the column 2. Column 4, dimer formation, the zoom-in images show the specific interactions that lead to the nanotube formation in each approach.

2.4.2 Characterization of higher order assemblies

2.4.2.1 Electrostatic model

In this first approach, we designed ionic interactions between two CTPR superhelices to promote the nanotube formation (**Figure 9A**). Given that the amino acid located at the position 31 in CTPR sequence is negatively charged (aspartic acid), it is only necessary to mutate the 15 position to an amino acid with positive charge. Despite the fact that amino acids as lysine and arginine have intrinsic positive charge at physiological pH, they are not suitable at this position because their side chains are too large and would prevent an appropriate packing between two protein chains. For this reason, histidine was selected as a potential pair and based on this model,

a the CTPR protein C6HD with 6 repeats where the amino acid at positions 31 are aspartic acids and the positions 15 are histidines was generated.

Upon protein purification, an electrophoresis gel showed the presence of both monomeric and dimeric states in the sample (**Figure 10A**). Ahead of these results, the dimer probably occurred due to hydrogen bonds between His15 and Asp31 instead of ionic interactions. The pH inside the bacteria is above histidine pka, since *E. coli* maintains the cytoplasmic pH in the range from pH 7.2 to 7.8^[246]. Therefore, the imidazole groups of the histidines at position 15 are mostly deprotonated and cannot establish salt bridges with the negatively charged aspartic acid at position 31.

To analyze the dimer formation and purify the two species, size exclusion chromatography was used (**Figure 10B**). Size exclusion chromatogram shows two elution peaks at elution volumes of 9 and 11 ml, corresponding to the dimeric and monomeric forms, respectively. The C6 wild type protein is run as a control for the monomeric state showing an elution volume of 11 ml (**A1-Figure 7**). Circular dichroism spectrum was performed on both monomeric and dimeric fractions to verify that both species were properly folded and compared with the CD spectra of CTPR6 wild type (**Figure 10C**). The introduced modifications affect the stability of the CTPR protein, when compared with the CTPR6 WT. However, the thermal denaturation curves of monomeric and dimeric species show that upon dimerization the protein becomes more stable and the denaturation transition is clearly more cooperative indicating the interaction between two CTPR monomers (**Figure 10D**). These results show that by applying a simple design approach and introducing charge complementarity dimeric forms of CTPR proteins can be obtained.

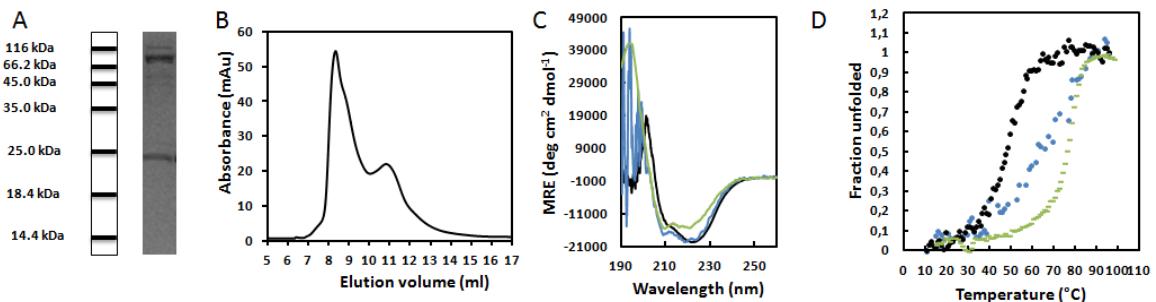


Figure 10. Characterization of the electrostatic model (C6HD) A. SDS-page gel of purified C6HD protein showing two bands that correspond to the monomeric and dimeric states. B. Size exclusion chromatography of the C6HD protein over a Superdex 75 column. The chromatogram shows two main peaks corresponding to the dimeric and monomeric forms of C6HD. C. Circular dichroism spectrum

of the CTPR6 wild type protein (in green) and C6HD monomeric (black) and dimeric states (blue). **D.** Thermal denaturation of the C6WT (green), C6HD (black) and C6HD_{dimer} (blue).

However, the obtained PNTs were relatively transient since the injection of a purified dimeric fraction in a second FPLC column resulted in the re-equilibration of the sample into monomeric and dimeric species (**A1-Figure 8**). Then, we aim to induce the dimer formation through a pH change. Lowering the pH below 6 would produce the protonation of amine group of the histidine and therefore an ionic interaction with the aspartic residue would be formed. However, the monomeric protein precipitated in the range of pH analyzed (5.4 to 5.8).

2.4.2.2. Aromatic model

In order to decrease the hydrophobicity of the designed interface that caused issues with the homogeneity of the nanotubular structures, a design based on π - π interactions mediated by the aromatic ring of tyrosines was proposed (**Figure 9B**). Tyrosine forms π - π interactions mediated by its aromatic ring, and their involvement in oligomerization process in TPR has already been reported^[247]. At this point, rationally designed models were validated using computational analysis. Docking tools were used in order to test the ability of the designed proteins to form stable dimers with the expected structures^[244,248]. In addition, these tests allowed the inspection of other potential structural arrangements of the designed monomers. After several rounds a CTPR model with two tyrosines at position 15 and 31 was selected to form the interacting interface. The model considered that the end repeats that would not interact with each other were not modified to avoid solvent exposed tyrosines at 15 and 31 positions (as described for C6L_2 model). This model resulted in energetically favorable PNTs when tested in *RosettaDock* and in *ClusPro* (**A1-Figure 9 and 10**). Therefore, a G15Y-D31Y-mutant was constructed. As explained above, the mutations were located in the 15 and 31 loop positions of the 4 non-terminal repeats in CTPR6 protein, forming the C6Y proteins, (**Figure 9B, A1-Figure 5**).

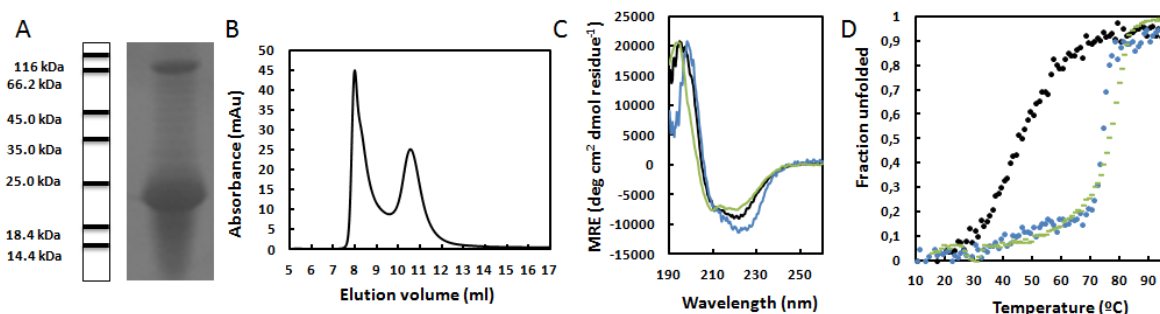


Figure 11. Characterization of the aromatic model (C6Y) **A.** SDS-page gel of purified C6Y protein showing two bands that correspond to the monomeric and dimeric states. **B.** Size exclusion chromatography of the C6Y protein over a Superdex 75 column. The chromatogram shows two main peaks corresponding to the dimeric ($V_e = 8.5$ ml) and monomeric ($V_e = 11$ ml) forms of C6Y. **C.** Circular dichroism spectra of the CTPR6 wild type protein (green), C6Y_{monomer} (black), and C6Y_{dimer} (blue). **D.** Thermal denaturation of the C6WT (green), C6Y_{monomer} (black) and C6Y_{dimer} (blue).

An electrophoresis gel showed the formation of dimers with double the size of the monomeric form (**Figure 11A**). Size exclusion chromatography was used to purify C6Y_{dimer} and C6Y_{monomer}, which had elution volumes in agreement with the ones expected for the monomeric and dimeric conformations (**Figure 11B**). Circular dichroism analysis was carried out to verify that the α -helical secondary structure was maintained in both monomer and dimer, compared with the spectrum obtained for the CTPR6 WT (**Figure 11C**). Finally, the interaction between monomers should provide a higher stability that will be reflected on the thermal stability of the dimer. Therefore, we performed thermal denaturation for both the purified monomer and dimer using circular dichroism (**Figure 11D**). As expected, the dimer denaturation not only required remarkably higher temperature ($T_{m_monomer} = 50^\circ\text{C}$ and $T_{m_dimer} = 79^\circ\text{C}$), but showed a more cooperative transition, indicating that the C6Y_{dimer} is more stable than C6Y_{monomer}. This latest design showed improved properties compared to the previously reported dimeric structures. Similarly to the previous models, when the equilibrium between the monomeric and dimeric forms was studied it was observed that the purified dimer re-equilibrates to a dimer and monomer upon dilution and analysis by size exclusion chromatography (**A1-Figure 11**). It is worth noting that the monomer population is likely to increase over the time in to extend and as a result of that the measurements must be done immediately after the purification and keeping the samples in ice whole time in order to minimize the shift towards monomeric form.

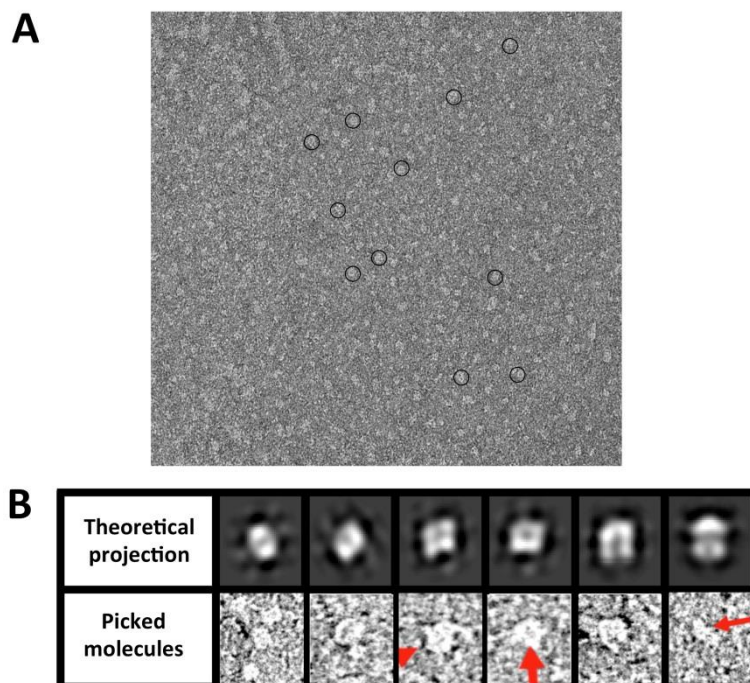


Figure 12. TEM characterization of the C6Ydimer. **A.** TEM image of C6Y_{dimer} at 0.8 μM . Negative stain was used to increase the protein contrast (uranyl acetate at 2%). **B.** Matching between theoretical 2D projection based on the PDB of the designed dimer, on the top, and the structure of some molecules picked from the TEM image, on the bottom.

Finally, TEM images were acquired in order to evaluate whether the shape and size of the protein dimer are related to the predicted model. In spite of this certain heterogeneity, in TEM could be observed individual particles with structures of similar size and shape to the theoretical design which are highlighted with black circles (**Figure 12A**). Those particles were selected and compared with the theoretical projections expected from the C6 nanotube (**Figure 12B**), indicating structural similitude between them. Therefore, those results show a structural correlation between theoretical model and the experimental structures, and thereby point to certain specificity of the designed protein-protein interaction. On the other hand, TEM images also showed the presence of larger protein polymeric structures, indicating the potential of the designed modules to form supramolecular assemblies larger than the designed discrete dimeric nanotubes, which needs to be further investigated.

2.5. Conclusions

In conclusion, we describe a strategy for protein-based nanotube formation through rational design, based on the knowledge and control of CTPR protein structure and stability. We showed how, by modifying the protein building blocks, we introduced novel interacting interfaces in the

scaffold to encode defined higher order structures. The introduction of a novel interface in the CTPR protein was designed to promote the interaction between two protein monomers to form dimers that were more stable and energetically favorable than the monomeric conformation. The modifications were introduced in a single CTPR module and extended over all the CTPR repeat structure. Because of the superhelical structure of the CTPR proteins, the generated dimers were expected to form a closed protein nanotube. The designs were tested in the context of a CTPR with six repeats (CTPR6) but could be extended to longer CTPRs since the novel interface will be extended along the superhelix.

Design of quaternary structure is considered a current challenge in protein engineering, since it involves the control over the preferential formation of the desired structure versus alternate conformations, which may have similar stability. Coiled-coil assemblies are examples for which the design rules are well-established and impressive advances on protein engineering have been achieved recently^[249]. Coiled-coil assembly design showed the formation a plethora of possible structures including trimmers, tetramers, pentamers, hexamers^[250], and heptamers^[251]. However, some of the design works led to various oligomerization states, similarly higher order assemblies based on coiled-coils resulted in heterogenous assemblies^[162], showing the complexity of designing specific quaternary structures. In the present work, despite the fact that the parallel nanotube assembly is the most favorable structure, it is important to note that other type of alternate configurations could be formed as discussed before.

We analyzed the nanotube structures obtained by two different approaches: electrostatic interactions and π - π interactions. The dimers are formed during the protein expression in the bacteria and are mostly stable in native gel. The two monomeric and dimeric species for the two models were purified. In all the cases the designed proteins retained their characteristic alpha helical secondary structure, comparable to the wild type CTPR6 protein both in the monomeric and in the dimeric forms. Also, it is worth mentioning that dimers are disassembled in monomeric species upon dilution and that the process is not reversible, since the concentration of monomeric species did not lead to the formation of dimers. The electrostatic dimer C6HD displayed less stability and showed prompt dissociation, which makes it difficult to purify the dimer in sufficient quantities for its characterization. By contrast, aromatic design was stable enough to be isolated and characterized. Moreover, protein concentration should be carefully established to ensure the maintenance of the dimeric form during potential applications. In all cases the dimeric forms

showed greater stability, determined by thermal denaturation, than the monomeric forms as expected from the interaction of two identical units. The thermodynamic stability of the dimeric structures depended on the model. The dimer formed by π - π interactions in the aromatic model (C6Y) showed higher cooperativity and stability ($T_m = 79^\circ\text{C}$) than the dimer formed by electrostatic ($T_m = 69^\circ\text{C}$). The change in the stability of the different dimers probably derives from the specificity of the interactions between the two subunits. This work shows that higher order structures based on repeated modules can be formed relatively easily through the introduction of protein-protein interactions of different nature. However, high-resolution structural studies by TEM revealed that it is not straightforward to design modules that assemble into well-defined homogeneous structures. In this sense, applying computational modeling tools during the design and selection process showed great potential in order to consider designs that minimize potential alternative states.

The development showed in this work about the formation of PNTs based on the repeat proteins by introduction of novel interfaces between the monomeric units will be the basis for the design of new interaction models. We aim to improve the stability and specificity of the dimeric forms by combining different types of interactions, in order to overcome the drawbacks presented in those models and the potential alternate conformation by forming specific covalent staples between the two chains. Moreover, it could be possible to apply these strategies to repeat proteins that display different twists^[194,252], thus forming PNTs with different internal diameters. Considering both the length and the superhelical twist of the repeated monomers, it will be possible to form PNTs with different properties in terms of length and diameter size.

The control in the formation of nanotube structure using repeat proteins is interesting for several applications such as filtration, encapsulation, and release of small molecules or drugs^[214]. Moreover, the possibility of functionalization the CTPR protein in a controlled way opens the door to introduce different functional groups inside the tube that are interesting for applications such as catalysis, optics, and electronics^[215-217].

Chapter 3

**Engineered protein-based functional
nanopatterned materials for bio-optical
devices**

3.1. Background

3.1.1. CTPR protein films

The structural characterization of the CTPR proteins was achieved by crystallography establishing the structure of each repeat motif TPR in the consensus TPR protein (CTPR) and of the overall protein. Through this structural analysis was demonstrated that CTPR protein adopts right-handed superhelical structure forming a complete turn of the superhelix with eight repeats. In the crystal structures of CTPR arrays, individual molecules stack “head-to-tail” to form virtually continuous superhelix. In addition, “side-to-side” interactions are also observed^[88,95,96,177] (**Figure 1**). These interactions have been exploited for the generation of highly ordered CTPR-based materials. Therefore, it is possible to form homogeneous and transparent protein films upon evaporation of the aqueous solvent. This process resulted in solid macroscopic films in which the protein assembled by specific contacts between superhelices similar to the ones present in the crystalline forms^[253]. On contrary, this type of higher order structures are not observed in solution, since even though the interaction occurs without a covalent staple it is not strong enough to maintain the supramolecular structure in solution.

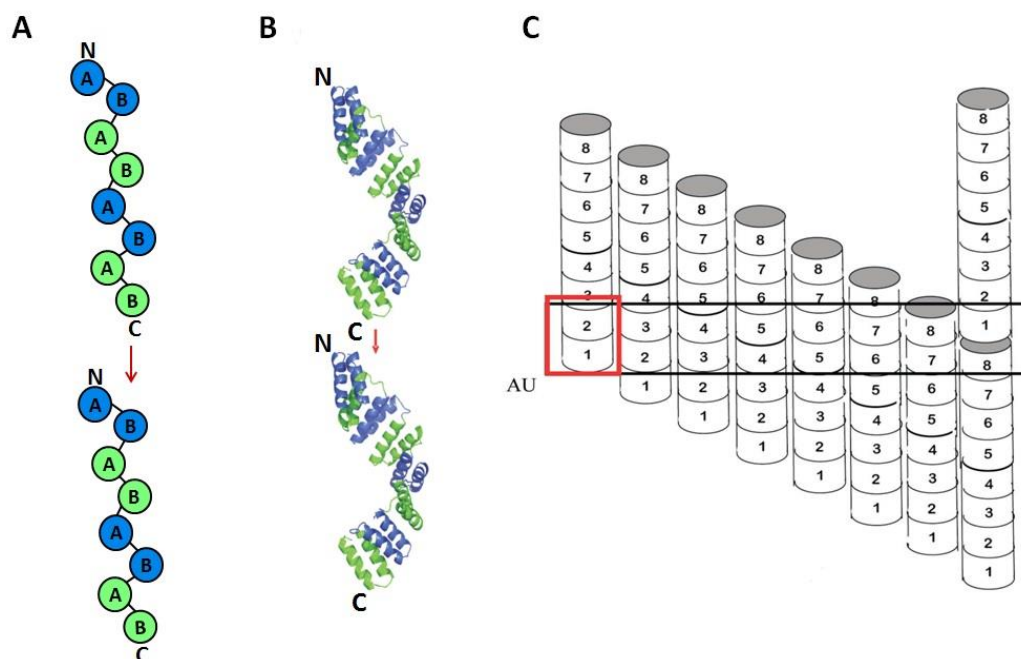


Figure 1. Schematic representation of the crystal-packing interactions between superhelical molecules. A) Schematic illustration of the stacking of helices between repeats of individual molecules. Each repeat is colored in green and blue alternatively. The first

repeat (in blue) of the next molecule must always pack against the last repeat of the previous molecule (in green). B) Ribbon representation of the superhelical stacking with each single repeat colored green or blue. C) As an example, in the $P4_12_12$ crystal form there are two repeats (numbered 1–8) within the asymmetric unit (indicated as AU; red box). For this arrangement there are eight equally possible two-repeat arrangements for the asymmetric unit. Figure from^[96].

The macroscopic order in the final material was verified using several techniques. On the one hand, X-ray diffraction (XRD) technique provides information about alignment of the protein in the film, showing characteristic peaks of diffraction ($2\theta = 10.82, 21.64$ and 32.05) that correspond to lamellar packing with a periodical d-spacing of 8.18 \AA (**Figure 2A**). On the other hand, circular dichroism (CD) technique provides information about the secondary structure of the protein. Thus, as it is depicted in the figure both spectra have the same shape typical of the alpha-helix structure (**Figure 2B**). Therefore, it was demonstrated that the secondary structure does not seem to be affected upon evaporation. Additionally, fluorescence anisotropy adds extra information about order of the film. In this experiment, a CTPR protein was used as scaffold to bind fluorophore-labeled peptide, *i.e.* the MEEVD peptide that interacts with the protein that contains a binding site for the peptide. In this manner, it was possible to determine that fluorophore-labeled peptide has preferential directional fluorescence emission when it is bound to the protein and excited with a specific angle, resulting in a sine-shaped plot. The specific arrangement of the CTPR helices in the film guides the orientation of the binding. Those values indicate that the material is anisotropic and, therefore, protein has a specific alignment and order (**Figure 2C**). Finally, atomic force microscopy (AFM) was used to obtain a detailed roughness of the film surface, demonstrating lack of roughness and, in turn, supporting the idea of intrinsic order in the film (**Figure 2D**).

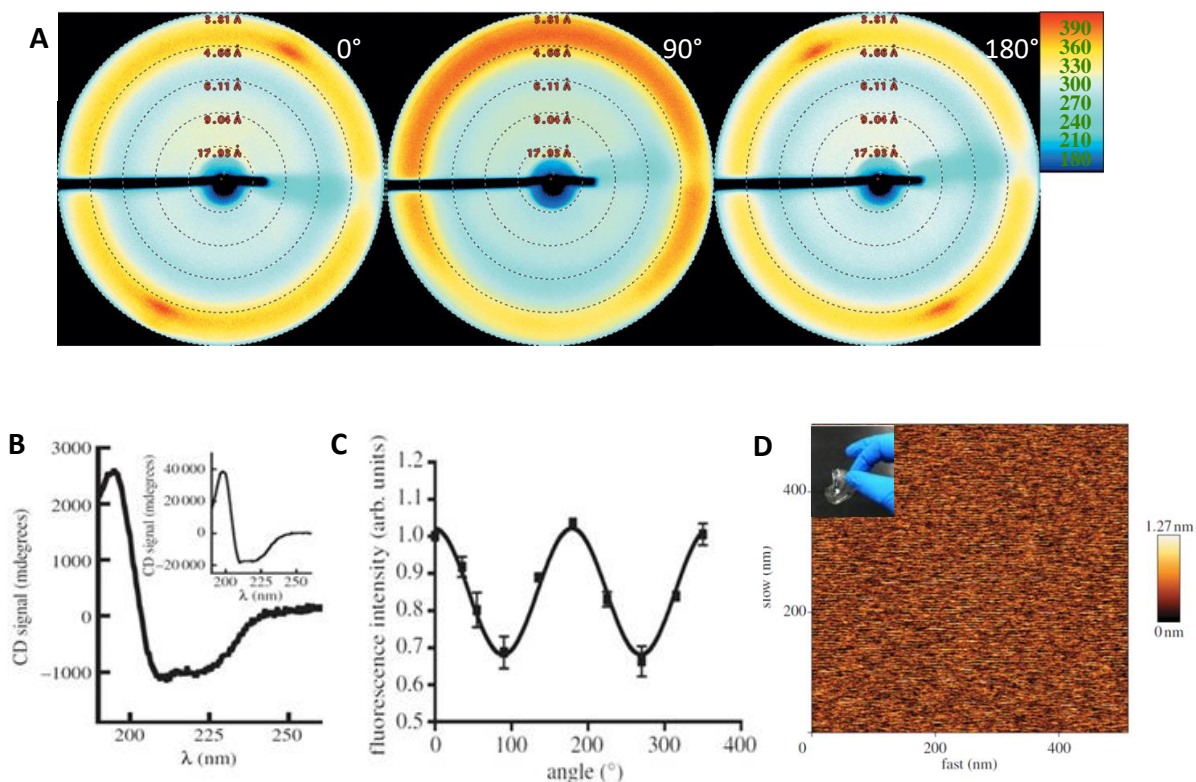


Figure 2. Structural characterization of CTPR18 protein films. A. XRD of the film at 0°, 90° and 180°. B. CD spectra of protein film and solution (inset). C. Fluorescence anisotropy of the film bound to the peptide ligand. D. AFM images. Figure from^[253].

The intrinsic properties of the CTPR protein, *i.e.* modularity and ordered packing and the preservation of the structure on the solid state, make them suitable for the rational design and assembly of functional biomaterials. Moreover, the thermal stability of the CTPR adds an extra characteristic highly demanded for the fabrication and use of optics devices. The differential scanning calorimetry (DSC) thermograms of CTPR proteins and thermodynamic parameters calculated from them, clearly showed the high thermal stability of the proteins and how the modularity of these TPR proteins affects to the thermal stability depending on the number of repeats^[254] (**Figure 3**).

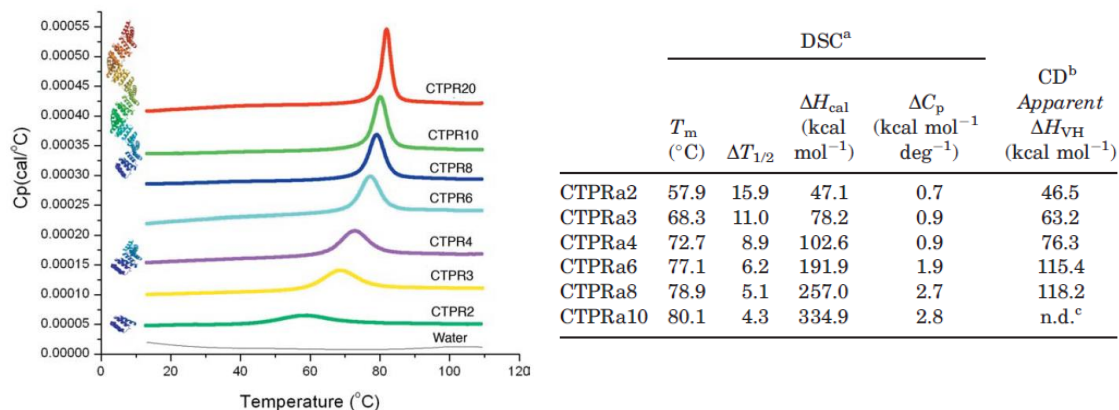


Figure 3. A. DSC thermograms of the proteins CTPR2 to CTPR20. The excess heat capacity is plotted versus temperature for CTPR2 (green), CTPR3 (yellow), CTPR4 (magenta), CTPR6 (cyan), CTPR8 (blue), CTPR10 (light green), and CTPR20 (red). Ribbon representations of the structures of three CTPR proteins within the series (CTPR2, CTPR4, and CTPR20) are shown. **B. Thermodynamic parameters for CTPRs unfolding by DSC and CD.** ^aThe thermodynamic data has been calculated from the DSC thermograms using a model free analysis in microcal origin. A progress baseline was used to setup the baseline before using the integration function to calculate ΔH_{cal} , T_m , and $\Delta T_{1/2}$. A step baseline was applied to calculate approximate ΔC_p values. The apparent ΔH_{VH} was calculated from the CD data assuming a two state model with linear extrapolated baselines for the native and unfolded states. ^bThe apparent ΔH_{VH} is the slope of the linear fit to the Van't Hoff plot ($\ln K$ vs. $1/T$). ^cn.d. not determined. Figure from^[254].

3.1.2 Functional proteins films

The fabrication of functional biopolymers-based optics devices is a current challenge since those biopolymers, in addition to encoded desired properties of biological materials such as the lack of toxicity, degradability and biocompatibility, they must resist harmful conditions as high temperatures. Amplified spontaneous emission (ASE) and Distributed feedback (DFB) laser are photo-physical phenomena exploited in a wide range of processes, such as light-emitting diodes (LEDs), sensing or optical communications^[255–258]. The physics behind them are based on the spontaneous and stimulated emission, which under population inversion, *i.e.* most of the electrons are in the excited state, is possible to produce light with define properties in terms of coherence (constant phase, same frequency, and waveform), and directionality (**Figure 4**). In particular, DFB lasers are a type of laser diode, devices similar to LEDs that under certain conditions emit coherent light. The active region of the device needs a periodically structured element or diffraction grating which acts as a mirror (Bragg reflector) reflecting only a narrow band of wavelengths (**Figure 4A**). Similarly, ASE or superluminescence is based on the same physics phenomenon but, in contrast to DFB, ASE does not have a feedback provided by cavity with mirrors (e.g. diffraction grating) and thus it does not produce coherent light. As a result, the emission peaks usually are slightly wider

than the ones obtained by DFB laser. However, the light bandwidth is considerably narrow and pure enough to be considered interesting for different applications^[259].

There are a plenty of examples in which biological sources have already been used in the fabrication of materials for ASE and DFB laser as DNA, silk fibroin, Green fluorescent proteins (GFP) or gelatin molecules^[260–263]. However, just a few cases have achieved to produce those phenomena properly due mainly to detrimental effect of photo-degradation and poor thermal and mechanical stability that hamper the proper function of lasing^[264].

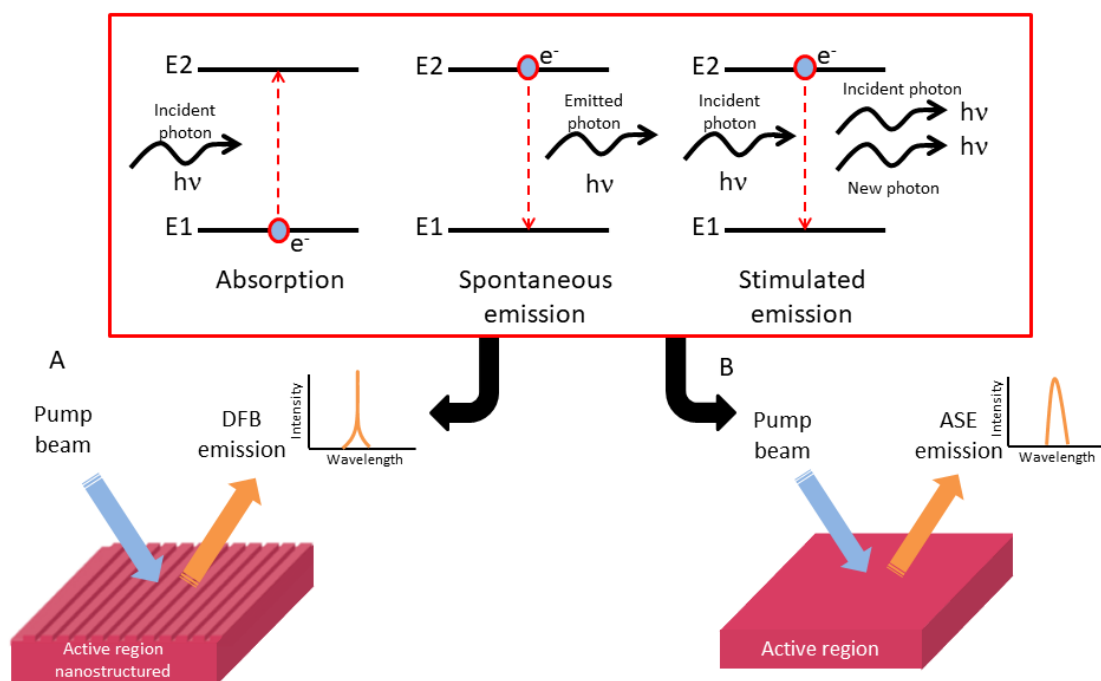


Figure 4. Photo-physical phenomena of ASE and DFB laser describing the interaction between electrons and photons (on top). A simplified schematic representation of ASE and DFB laser, including the active region, the light pumping and the aforementioned phenomena (bottom). **A.** Active periodic grating confines the light giving rise to DFB laser emission (coherent light). **B.** A simply non-structured active region produces ASE emission (non-coherent light).

In principle, unless the biomolecule itself displays fluorescence, as GFP, the material needs an active lasing molecule. There are many types of dyes that may cover all visible spectra and beyond. However, just few are really suitable for lasing, due mainly to the spectroscopical properties required, *i.e.* high quantum yield and photo-stability^[265]. Rhodamine 6G (Rh6G), that belongs to the family of xanthene dyes, fulfills those aforementioned requirements and it has been widely used in biotechnological applications such as fluorescence microscopy, flow cytometry, and fluorescence correlation spectroscopy^[266,267]. Rh6G has a strong tendency to form aggregates which may drastically modify the optical properties of the dye^[268,269]. Engineered CTPR protein

function by a Cys enables to conjugate Rh6G in an easy manner so that it can organize Rh6G into a protein film and hamper the detrimental effect of aggregation. Derived commercial of Rh6G can be designed to have a specific functional group. In particular, maleimide group an imide heterocycle that is one of the more widely used in bioconjugation (**Figure 5**). The fast kinetics and high specificity toward thiol groups of maleimide permit a straightforward conjugation with cysteines residues within proteins^[270].

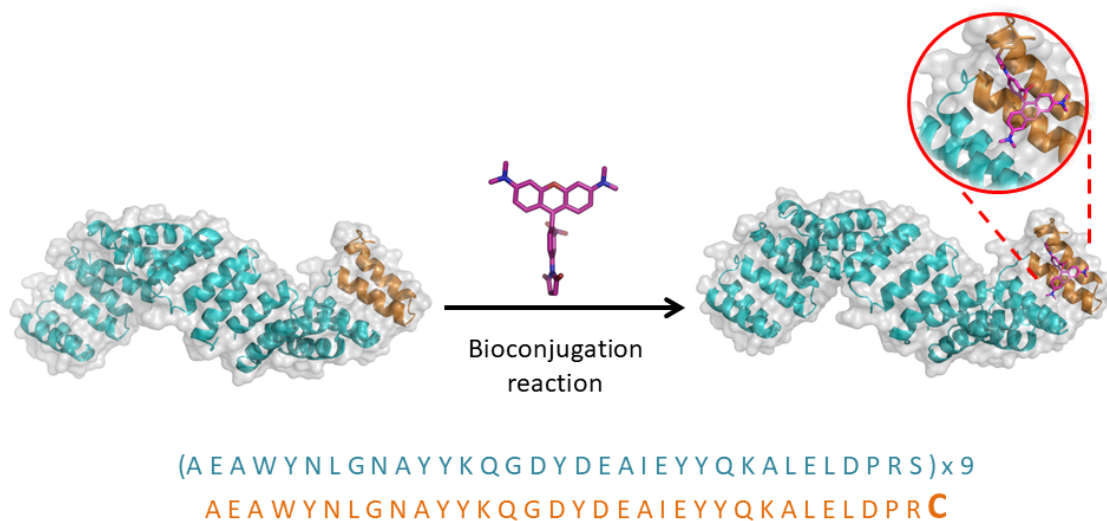


Figure 5. Reaction of bioconjugation between Rh6G and CTPR10Cys (top). CTPR10 amino acids sequence showing the Cys mutated in the C-termini (bottom).

Given the properties of CTPR proteins, we hypothesized that CTPR protein might be an excellent candidate to organize Rh6G in a protein film with outstanding laser properties based on ASE and DFB laser, and this is the experimental demonstration that is covered in this chapter.

3.2. Introduction

Active biocompatible materials and devices are emerging as a new stone corner in multiple sectors including healthcare, energy, lighting, information, computer technology, and environmental monitoring^[271–273]. A variety of bioinspired strategies have recently emerged to develop universal fabrication methodologies to create new functional biomaterials with improved properties and potential uses^[274–277]. Bioinspired materials are capable of recreating processes that occur in Nature, where complex structures emerge from the combination of small components through self-assembly, to exhibit and display a broad variety of functionalities. Although these bioinspired fabrication approaches have opened new routes toward the scalable production of

biocompatible multifunctional systems in biooptics^[271] and lighting^[271,278], the development of protein-based devices is still in its infancy. Significant progresses have been made using proteins that encompass the building blocks of natural protein-based materials, mostly silk fibroin^[279]. Silk fibroin materials have been fabricated using various strategies, including spin coating, soft lithography, inkjet printing, and contact printing, of silk solutions^[280–283]. These pioneering works illustrated the great potential of bioinspired building blocks for the fabrication of active functional materials. However, the use of natural materials usually requires several pre-processing steps, which are often complex and involve costly equipment, hampering their reproducibility in low-resource laboratories^[284]. Although there is an increasing understanding of the interactions and processes that govern the structuration of biomolecules^[144,285], it remains still insufficient, and the state-of-the-art research in the field of fabrication of hybrid biomaterials and devices relies on trial-error assays.

Protein engineering enables the creation—in addition to the naturally occurring building blocks—of protein-based synthetic building blocks, which significantly enhances reproducibility rates and facilitates the rational design and assembly of functional biomaterials^[192,274]. Modular building blocks with simple intermolecular interactions allow for better control of the assembly^[189,286], to obtain different nanomaterials^[157], and even 3D structures^[287] by using simple building blocks with well-described intermolecular interactions, such as coiled-coils and amyloid peptides^[80,162]. Engineered building blocks enable the control over the organization from the simplest to more complicated structures. This is achieved using a bottom-up strategy based on highly specific biomolecular interactions, which facilitates the nanometer-scale arrangement of bio-components, tailoring their final features and functionalities^[141,142,190,288]. Moreover, engineered proteins display similar biocompatibility, biodegradability, and water-processability than their naturally occurring counterparts. Owing to their easily tunable structure, stability, self-assembly properties, and functional reactivities, engineered proteins constitute a promising biocompatible alternative for the fabrication of the next generation of bioinspired functional materials.

To study how small engineered proteins perform as building blocks for material engineering, we chose a well-characterized system based on an engineered repeat protein domain, the consensus tetratricopeptide repeat proteins (CTPRs)^[197]. CTPR proteins are formed by a variable number of identical repeated modules, each one comprising 34 amino acids that fold in a helix-

turn-helix motif^[96,289]. Their modular architecture allows the elongation of the basic structural unit by varying the number of repeats. CTPR proteins adopt a superhelical structure with eight repeats per superhelical turn^[96,289,290], whose stability is determined by the number of repeats^[184,289]. In previous studies, we demonstrated the self-assembly properties of CTPR proteins into nanofibers and thin films, which maintained the architectural and functional features of the individual proteins under these conditions^[177,253]. In particular, CTPR-based solid films are mechanically robust and present hierarchical anisotropic mechanical properties that can be tuned by the constituent molecules^[175,291]. This adds an extra advantage over other broadly studied biomaterials like, for example, those based on silk fibroin. In addition, we have shown that CTPR-based proteins can encode diverse recognition activities^[187,292,293], and can be further endowed with other functional elements,^[192,294,295] which can be exploited to introduce new functionalities in the final biomaterial.

In combination with bottom-up self-assembly approaches, it is interesting to explore simple top-down fabrication techniques that are usually applied to polymeric materials, such as replica molding, in the context of protein-based materials. Providing these biocompatible functional materials with nanoscale structures will add an extra level of complexity and open the door to applications that require nanostructuration, such as the development of optically active devices. However, many current techniques in nanofabrication take place in semiconductor and electronic industry^[296], and their adaptation to other fields of research such as biology^[297,298], organic electronics^[299], plasmonics^[300], or catalysis^[301,302], in which unconventional, soft, or degradable materials and substrates are used, represents a challenge^[303].

Unconventional nanofabrication techniques, such as soft lithography performed using elastomeric stamps, provide a simple, affordable, and versatile alternative to traditional lift-off methods to produce micro- and nano-scale patterns over large areas^[296,304,305]. Particularly, soft replica molding enables the simple transfer of nanostructures from a patterned polydimethylsiloxane (PDMS) stamp to a substrate placing a molding agent—typically referred as “ink”—between the stamp and sample. With the appropriate choice of stamp, the final resolution of soft replica molding at room temperature it is only limited by Van der Waals forces^[296]. A variety of soft lithographic techniques have been proposed to pattern biological material, such as biomolecules, proteins, or nucleic acids, providing also control over the surface chemistry of the patterned substrate^[306,307]. Similar approaches have already been applied to control the structure

of cellulose and silk-based materials^[308,309], but have not been implemented in engineered building blocks.

Here, we explored the potential of engineered proteins to develop photoactive protein-based devices using a fabrication strategy that combines a bottom-up (functionalization of the protein-based unit cells) and a top-down (topographically-guided molding) approaches. This novel system combines the advantages of soft nanolithographic techniques and self-assembly of modular repetitive proteins as building blocks. In addition, we developed a mild crosslinking protocol that preserves the topographical features in aqueous environment. The strategy is fully performed in aqueous environment, preserving the structure and function of the constituent protein building blocks, and allowing the direct incorporation of different functional moieties. Thus, we were able to introduce a new functionality focusing on laser applications by incorporating a lasing dye into the functionalized protein films to provide the capability to absorb, emit, confine, and amplify light. The results of this work open up new perspectives for light-management in devices based on engineered recombinant proteins with a broader range of applications given the versatility of the methodology presented, and its potential implementation to other protein systems that may add different competitive advantages.

Overall, our technique to fabricate flexible and conformable nanopatterned protein layers over large areas has the potential to unveil new concepts at the interface of protein engineering, material sciences, and biocompatible functional nanodevices. The possibility of generating fully biodegradable protein materials patterned at the nano scale will pave the way towards the development of biosensors, bio-optics, lasers, nanoelectronics, plasmonics, implantable devices, tissue engineering, and fundamental studies in cell biology.

3.3. Experimental section

3.3.1. Protein production and purification

The gene encoding CTPR proteins were previously generated based on a consensus CTPR protein^[190]. The encoding gene was ligated into the His tag expression vector pPROEX-HTa vector, that produces a His-tag fused protein for affinity purification^[199]. The plasmid was transformed into BL21 (DE3) *Escherichia coli* cells. Cells were grown in LB with 0.1 mg/ml of ampicillin in agitation to an O.D. between 0.6 and 0.8. Protein expression was induced with 0.6 mM IPTG for 5 hours, and

after this, cells were centrifuged at 4500 rpm and resuspended in 300 mM NaCl, 50 mM Tris pH=8.0 Lysis buffer with 1 mg/ml of lysozyme, 5 mM β -mercaptoethanol, and 1 μ l/ml of protease inhibitor. The resulting lysate was sonicated during 2 minutes with 30 second intervals, and centrifuged at 10000 rpm for 45 min. Protein purification was performed by affinity chromatography using high density cobalt ABT beads. The eluted protein was dialyzed overnight in PBS (150 mM NaCl, 50 mM phosphate buffer pH=7.4 with 2.5 mM β -mercaptoethanol). Then, the protein was concentrated and purified by FPLC gel filtration chromatography over a Superdex 200 HiLoad column. Fractions containing the protein were analysed in 15% acrylamide gels to confirm the purity of the protein. Finally, protein was concentrated until the desired concentration, from 50 to 300 μ M, using the estimated molar extinction coefficient at 280 nm from the amino acid composition^[240].

3.3.2. Generation of nanopatterned protein films

In order to prepare the PDMS stamps, a section of a DVD was cut off with scissors. Carefully, the two polymer layers are peeled, keeping the polycarbonate layer as master piece. Then, a 10:1 mix of Slygard prepolymer and curing agent was poured over the master piece and left curing at 70°C for an hour. Finally, the PDMS stamp ready for use was removed with a razor blade. The approximate area of each stamp was 2.5 cm² and the gratings can be defined based on the application. In this work we used gratings with period of 700 nm and 416 nm and a height of 140 nm. The diffraction grating had a groove density of 1500 grooves/mm.

The PDMS stamps were washed with distilled water and ethanol 70% and dried at room temperature (ideally under a N₂ flow, to avoid watermarks). Two approaches were used for the generation of nanopatterns on the protein films. First, for the generation of free-standing CTPR protein-PMMA films, a PDMS stamp was placed with the pattern facing-up over a plastic piece on a microscope slide. The plastic piece was useful to avoid the adhesion of the stamp to the slide. As shown in Figure 6, protein solutions of 300 μ M CTPR and 1% (w/v) PEG-400 were deposited over the PDMS stamp and left to dry for at least 4 hours at room temperature to ensure the formation of the film. PEG is used as plasticizer as previously described^[253]. Once the film was formed, a solution of 10% PMMA 950KDa in GBL (gamma butyrolactone) was deposited over the film and left until solidification at 70°C. GBL was used as solvent since it does not affect the protein film during its evaporation. PMMA layer was added with two objectives: i) to provide a back support that will

facilitate handling of the films; ii) to be used as an adhesive to transfer the patterns to other surfaces. A second approach was the generation of CTPR films directly on a variety of substrates, such as glass, quartz, or plastic. In this latter case, a protein solution with PEG-400 was deposited on the selected substrate and the PDMS stamp placed over the drop for drying the film at room temperature. Films were readily released from the PDMS stamp without requiring functionalization or surface treatment of the elastomer. The PDMS stamps were used several times to fabricate protein films without degradation in their performance.

3.3.3. Crosslinking of the nanostructured protein films

Glutaraldehyde at 0.5% was used as crosslinking agent for a gentle vapor diffusion crosslinking^[310]. The reaction was carried out in wells of 1 ml for 24h at room temperature. At bottom of well was added 500 μ l glutaraldehyde solution while the protein film was fixed on a cover slip used to seal the well. After the reaction, the films were recovered and dipped into water solution to monitor the potential release of the protein into the solvent in order to evaluate the cross-linking efficiency.

3.3.4. Structural characterization of the nanostructured protein films

Scanning electron microscopy (SEM) Carl Zeiss AURIGA CrossBeam FIB/SEM was used to image the surface patterning of the films. Films were mounted over a carbon tape and imaged under vacuum conditions, applying an electron high tension (EHT) of 3.00 kV, WD of 5.8 mm and an aperture size of 20 μ m.

Atomic force microscopy (AFM) to determine the groove height, surface roughness and thickness of the patterned films, was performed using a JPK NanoWizard II, coupled to a Nikon Eclipse Ti inverted fluorescence optical microscope. An Olympus commercial silicon nitride cantilever tip (OMCL-RC800PSA) with a force constant of 0.76 N/m and a resonant frequency of 71 kHz was employed in dynamic mode. Surface morphology of the patterns was studied under ambient conditions in air environment. To remove large area background, 1st to 3rd order polynomial fitting was applied using JPK Data Processing software.

Film thickness was measured using a mechanical profilometer “Dektak XT” with 2.5 mm radio stylus. The applied strength was the minimal (around 1mg), and the length of analysis was 7500 μ m.

Circular dichroism experiments to determine the secondary structure of the CTPR components within the films were performed using a Jasco J-815 spectropolarimeter. The solid films were deposited on a sandwich quartz cuvette (0.1 mm path length). The CD spectra were acquired at 1 nm increments and 10 seconds average time over a wavelength range of 190 to 260 nm.

X-ray diffraction was performed in a PANalytical X'Pert PRO diffractometer with Cu tube ($\lambda = 1.54187 \text{ \AA}$) operated at 45 kV, 40 mA, Ni beta filter, programmable divergence and anti-scatter slits working in fixed mode, and fast linear detector (X'Celerator) working in scanning mode.

3.3.5. Optical characterization of the nanostructured protein films

Optical images of the patterned films were acquired on a Leica DMI 3000 B optical transmission microscope using a 63x objective lens, or using an Olympus optical microscope Model (BX51) with an objective of 100X (Nikon) and numerical aperture of 0.70. Images were processed using ImageJ software for background subtraction.

Ellipsometry measurements were performed in spectroscopic rotating compensator ellipsometer (*M2000V, Woollam, NE, USA*) at room temperature ($21 \pm 1^\circ\text{C}$), operating in a wavelength range from 380 to 1000 nm, using an angle of incidence at 70° . The protein sample was deposited on silicon wafers (SiO_2) using a spin coating method (*Laurell Technologies corporation Model WS-400B-6NPP/LITE*) at 1000 rpm during 10 min. First, the silicon surface was cleaned in pure acetone to remove coated surface, rinsed thoroughly with milliQ water. Second, it was cleaned with 96% v/v ethanol and rinsed with water. Finally, the surface was dipped into 2% w/v solution of SDS for 30 min and after rinsed with water. In order to ensure the complete surface cleaning from organic molecules UV/ozone treatment was carried out using a UV/ozone ProCleanerTM (*Bioforce Nanosciences*). To calculate the refractive index the data were processed using the software CompleteEASE (*Woollam, NE, USA*) and the Cauchy model was used to fit the results.

$$n(\lambda) = A + \frac{B}{\lambda^2} + \frac{C}{\lambda^3}$$

The steady-state transmittance and emission measurements were performed in both solution and thin films using Varian Cary 50 UV-VIS (spot size of 1 mm² in the 200-700 nm spectral region) and FS5 (Edinburgh) spectrophotometer (spot size of 1 mm² and excitation at 500 nm) coupled with integrating sphere for PLQY measurements. The photostability of both CTPR-Rh6G films was performed using home-made system that consists of a high power excitation station - LED WINGER® WEPGN3-S1 Power LED Star green (520 nm) 3 W – 120 lm (505 nm and 6.6 mW/cm²) - coupled to an IR camera (FLIR FS5), and a detection station consisting of spectrophotometer (Avaspec-ULS2048L-USB2). Both temperature and emission changes of the films are monitored over time.

Bending assays were performed with DMA Q800 from TA Instruments in a multi-frequency-strain module with single-cantilever clamp. The experiment was made with 0.1% strain and 1Hz of frequency at room temperature in size sample of 17.5mm x 5.2mm x 0.2mm.

Time-resolved photoluminescence emission measurements were performed using a pulsed laser diode (405 nm, 80 ps, LDH Picoquant) as photoexcitation. The emission intensity of the sample (in 10⁻² mbar vacuum) was collected in free space, subsequently dispersed by the grating of a 1/2 m monochromator and detected with a PMT assembly (PMA – Hybrid from Hamamatsu Photonics) coupled to a Picoquant Hydrharp time-correlated single photon counting system.

Laser action in distributed feedback (DFB) lasers based on CTPR-Rh6G proteins were performed exciting with a fraction of the 532 nm output provided by a narrow-band OPO (Continuum Sunlite, bandwidth 0.075 cm⁻¹, pulse width 3 ns) pumped by a seeded frequency-tripled Nd:YAG laser (Continuum Powerlite PL8000) and equipped with a frequency doubler (Continuum FX-1). The pump beam was focused under oblique incidence on the DFB surface (placed in vacuum) using a 200 mm focal length spherical lens, with the sample placed slightly out of focus (9.4 10⁻² cm²). Laser action emitted perpendicularly from the DFB surface was detected with a spectrometer (SP2500, Acton Research) equipped with a liquid nitrogen cooled back-illuminated deep depletion CCD (Spec-10:400BR, Princeton Instruments). A 533 nm notch filter was placed in front of the spectrometer slit to selectively remove pump laser scattering. Intensity dependent measurements were performed upon pump beam attenuation with a set of neutral density filters. Amplified spontaneous emission (ASE) measurements on CTPR-Rh6G protein films were performed with the same photoexcitation as lasing measurements but using a 200 mm focal length cylindrical lens and a 3 mm slit width to define a photoexcited rectangular area of 700 μm x 3 mm on the sample and the photoluminescence (PL) was collected from the edge of the sample (90° respect to incidence)

and sent onto the spectrometer. The pump thresholds for laser action and ASE were obtained as the incident fluences at which the FWHM linewidth falls to half of the difference between the linewidths of the PL and laser and ASE spectra respectively.

3.3.6. Distributed feedback (DFB) lasers from nanostructured CTPR-Rh6G films

In order to obtain a DFB protein based system, nanostructured protein films doped with a laser dye were fabricated. For this purpose two approximations were tested: 1) mixing of the laser dye with the protein solution and 2) covalent coupling of the laser dye to the protein unit. In the first approach, to obtain nanostructured protein films doped with Rh6G, 15 μl of CTPR10 300 μM were mixed with PEG 1% (w/v) and Rh6G 1 mg/ml. The solution was mixed gently during 10 min and left in dark during the formation of the nanostructured film following the procedure described above. In the second approach, a CTPR10 protein with a single cysteine at the C-terminal end was used to generate a CTPR-Rh6G covalent conjugate for a better organization of the Rh dye in the protein films. Tetramethylrhodamine-5-maleimide (Sigma-Aldrich) was attached to the CTPR10-cys protein following previously described protocols^[311,312]. Nanopatterned films for DFB lasers were produced using a solution of the CTPR-Rh6G conjugate at 300 μM and PDMS stamps with 416 nm period as described above.

For efficient lasing an optimized nanoimprinting process was required. A grating with 416 nm period was fabricated by thermal nanoimprinting lithography (T-NIL) on a soft material, frequently used as an intermediate polymer stamp (IPS[®], Obducat), (**Figure 12D**). The pattern was replicated from a Si master mold (NIL Technology) by using an EITRE Nano Imprint Lithography system (Obducat) as schematically depicted on A2-Figure 10. The imprinting parameters were adjusted according to the manufacturer specifications. The T-NIL was accomplished in a sequential process. Temperature and pressure profiles during the process are described in A2-Figure 6. Initially, the temperature was raised up to 155°C, then the pressure was increased sequentially to 20 and 40 bar and kept constant during the rest of the process. After 3 minutes at 155°C the temperature was decreased in two steps down to 100°C and 70°C before releasing the pressure. Finally, the sample was cooled down to room temperature before unmolding. Subsequently, CTPR-Rh6G protein films were deposited on top by spincoating protein solutions (CTPR-Rh6G at 500 μM) in PBS on top of IPS templates. A SEM vertical cut of CTPR-Rh6G on nanostructured IPS (**Figure 12C**) depicts a fibrillar protein network which replicates the ripples underneath.

3.4. Results and discussion

To explore the potential of designed proteins to create nanopatterned biomaterials capable of acting as active optical devices, we use a designed protein system that exhibits large-scale self-assembling properties. Figure 6 shows the topology-guided self-assembly strategy followed to create flexible nanopatterned films of engineered proteins. We casted a 0.4-3% water solution of CTPR protein onto the nanopatterned surface of the elastomeric stamp and allowed the water of the solution to slowly dry at room temperature, similarly to previously described protocols for generating CTPR protein films—see experimental section for more details^[176]. After 5h, the solvent evaporates and generates a thin CTPR film ($\sim 5 \mu\text{m}$) that can be easily transferred to wet surfaces via moisture-induced adhesion. A thin layer of polymethylmethacrylate (PMMA) was deposited onto the unpatterned side of the film while this was still on the stamp to facilitate its handling (**Figure 6C and D**). CTPR thin films can also be directly printed over any substrate by pressing the aqueous protein solution with the elastomeric stamp during 5h over the target surface (**Figure 6E**). After the protein film is dry, the PDMS stamp was easily peeled from the film exposing its patterned surface. We combined structural and optical methodologies to verify the structural integrity and high-resolution successful patterning of the protein films.

The optimum protein concentration required to create homogeneous nanopatterned films is a trade-off between the large protein packing degree to completely fill the nanofeatures on the stamp and the viscosity required to facilitate the appropriate flow of molecules inside the stamp channels (**Figure 6A, 6B**). Bearing this in mind, a range of 0.4 to 3% (w/v) of purified CTPR10 protein, a consensus CTPR protein with 10 identical repeats^[254,289], were tested in the formation of nanopatterned films. The generation of continuous and homogeneous patterned protein films was first evaluated under optical microscope, confirming the formation of patterned films at CTPR10 concentrations from 0.4% to 3%. Protein concentration below 0.4% leads to heterogeneous discontinuous films. A 1.5% CTPR10 concentration was chosen for a detailed characterization, as it led to the highest film homogeneity and reproducibility with the lowest film thickness ($\sim 1 \mu\text{m}$).

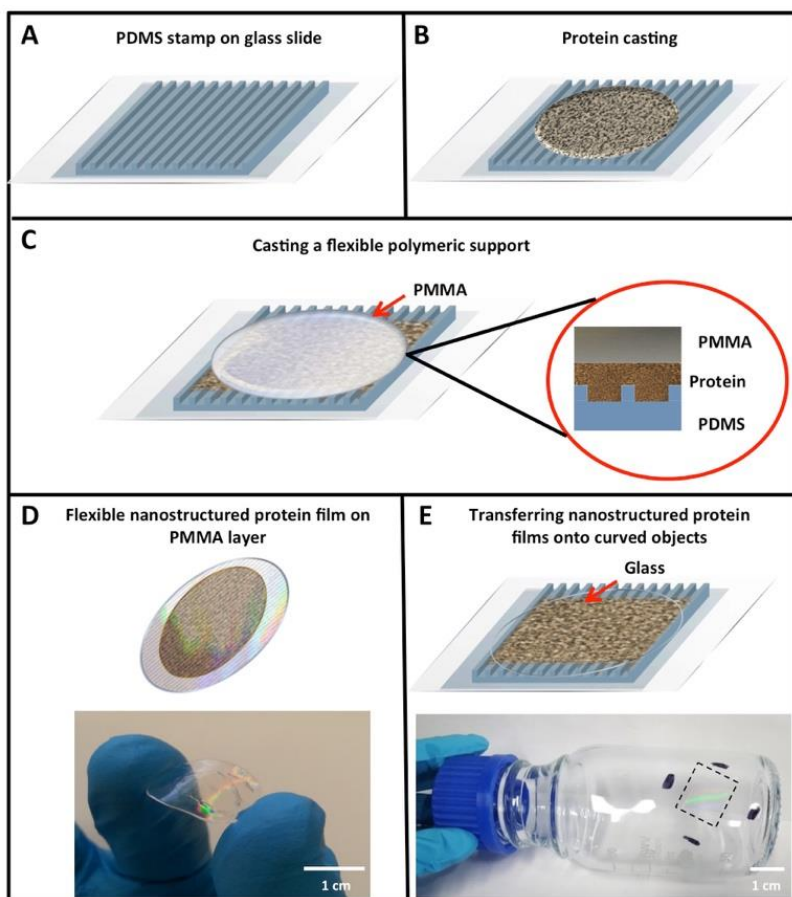


Figure 6. Schematic strategy for obtaining nanostructured protein films. **A.** PDMS stamp over a microscope slide covered with a plastic film in order to facilitate the stamp removal. **B.** A solution of concentrated protein with PEG is deposited over the PDMS stamp and dried at room temperature. **C.** Once the protein film is formed, a drop of liquid 10% PMMA is deposited over the film and dried at 70°C. **D.** When dried, the PMMA-protein film is easily peeled from the PDMS stamp. **E.** As proteins display good adhesion properties, a glass support can be used instead of PMMA, in this case the proteins film is directly transferred to the surface of the glass. As example, a protein film has been stamped on a glass bottle.

The nanopatterned CTPR films prepared by replica molding are highly transparent and flexible (**Figure 6D**). Immediately after peeling the stamp from the nanopatterned CTPR film, characteristic iridescent reflections can be observed due to the diffraction of the light by the protein nanostructures on the film (**Figure 6D and 6E**). We used this observation as the first evidence to verify that the molding process worked effectively. It is worth highlighting that adding a PMMA layer as a back support for the nanopatterned CTPR film is only required to facilitate the manipulation of the films, and that the free-standing protein films can also be fabricated and transferred to surfaces by simply omitting this back support. Also, as proteins display excellent adhesion properties, we can generate the films directly onto substrates like quartz, polymers, glass, etc. Figure 6E shows the lateral wall of a glass bottle coated by a nanopatterned CTPR film,

demonstrating the good adhesion and conformability of CTPR films created on hydrophilic curved surfaces.

Importantly, the protein structure was neither altered during the film casting process, as demonstrated previously^[176], nor during the nanopatterning process. We evaluated the protein structure in the patterned films by circular dichroism observing that the secondary structure of the CTPR protein remained helical, showing no evidence of structural alteration during the casting and drying processes (**Figure 7A**). Furthermore, X-ray diffraction of patterned films showed a most intense broad signal at 2θ around 20° and a minor peak around 10° (**Figure 7B**), those values with a d-spacing of about 1 nm, as has been previously reported for the CTPR unpatterned films, which confirms the presence of the signature peaks ascribed to lamellar packing of CTPR proteins and indicates the directional order^[176,294]. These results are critical for further ordered functionalization of the protein films using the protein structure as a template to fabricate precisely organized functional elements.

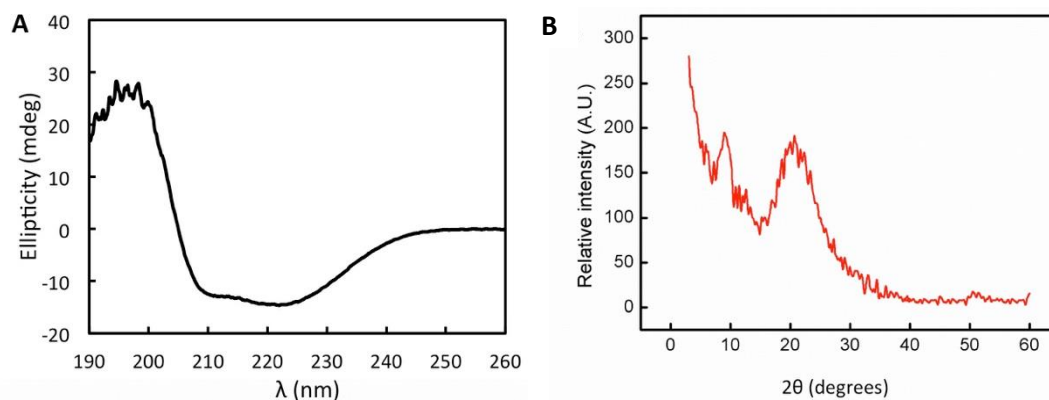


Figure 7. Structural characterization of the protein films. A. Circular dichroism spectra of nanostructured CTPR protein film deposited on a sandwich quartz cuvette. B. X-ray diffraction spectra of the nanostructured CTPR protein film.

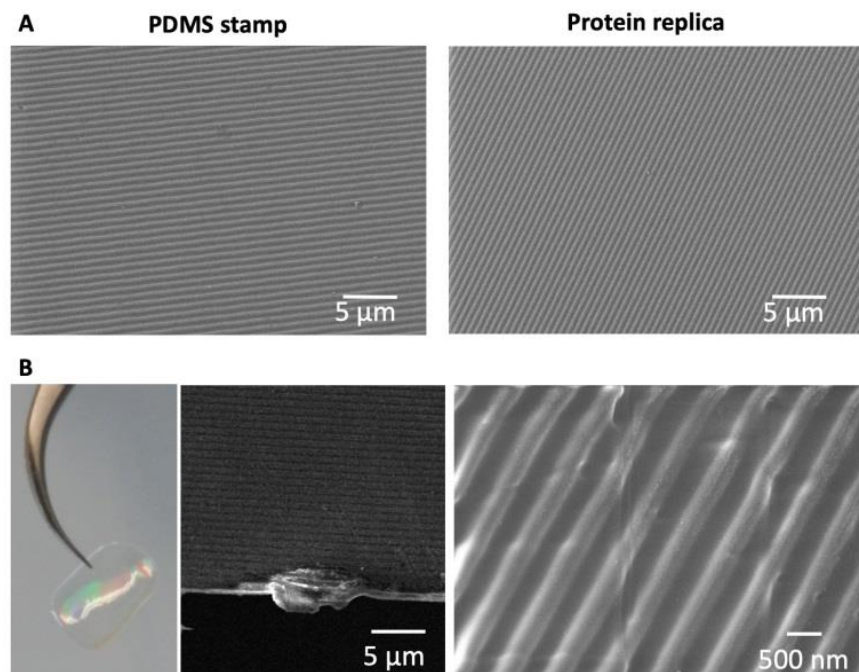


Figure 8. Scanning electron microscopy characterization of the nanostructured protein films. **A.** SEM micrographs showing a comparison of the surface of the PDMS stamp and the surface of the protein patterned film, in which the nanostructure patterns are perfectly replicated. **B.** From left to right, optical image and SEM image of the film cross section the patterned protein films are self-standing. On the right a higher magnification SEM image of the protein film is shown.

The nanopatterned protein films were first imaged after removal of the PDMS stamp under optical transmission microscope, revealing in the samples patterned surfaces as large as 1 cm^2 . The surface morphology, topography, and roughness were characterized by scanning electron microscopy (SEM) and atomic force microscopy (AFM) techniques. SEM images revealed that the protein films accurately replicated the nanopatterns on the PDMS stamp (**Figure 8**), and that the films are free-standing (**Figure 8B**). Additionally, the nanopatterned film maintained the structural integrity at least 6 months after fabrication, which provides additional value to the system (**A2-Figure 1**). Using AFM, an area of $50 \times 50 \text{ } \mu\text{m}^2$ was imaged (**Figure 9**). The profiles of four different areas of $10 \times 10 \text{ } \mu\text{m}^2$ scattered across a larger zone, demonstrate the uniform topology of the protein nanopatterns through the film. The protein nanofeatures exhibit a height of $\sim 120\text{-}130 \text{ nm}$, while the nanoscale features on the PDMS stamp used as a template for the self-assembly of the protein have a height of $\sim 140 \text{ nm}$. This difference in height may be due to the shrinking caused by the evaporation of the water from the protein structure of the film (**Figure 9A**). The nanostructures of both the stamp and the molded protein film exhibited a pitch of 700 nm . We compared a section and the reconstruction of $2 \times 2 \text{ } \mu\text{m}^2$ of the PDMS stamp (**Figure 9B**) and the

patterned protein film (**Figure 9C**). Using high-resolution AFM microscopy, we found that the root-mean-square roughness of the protein film is below 10 nm across the film.

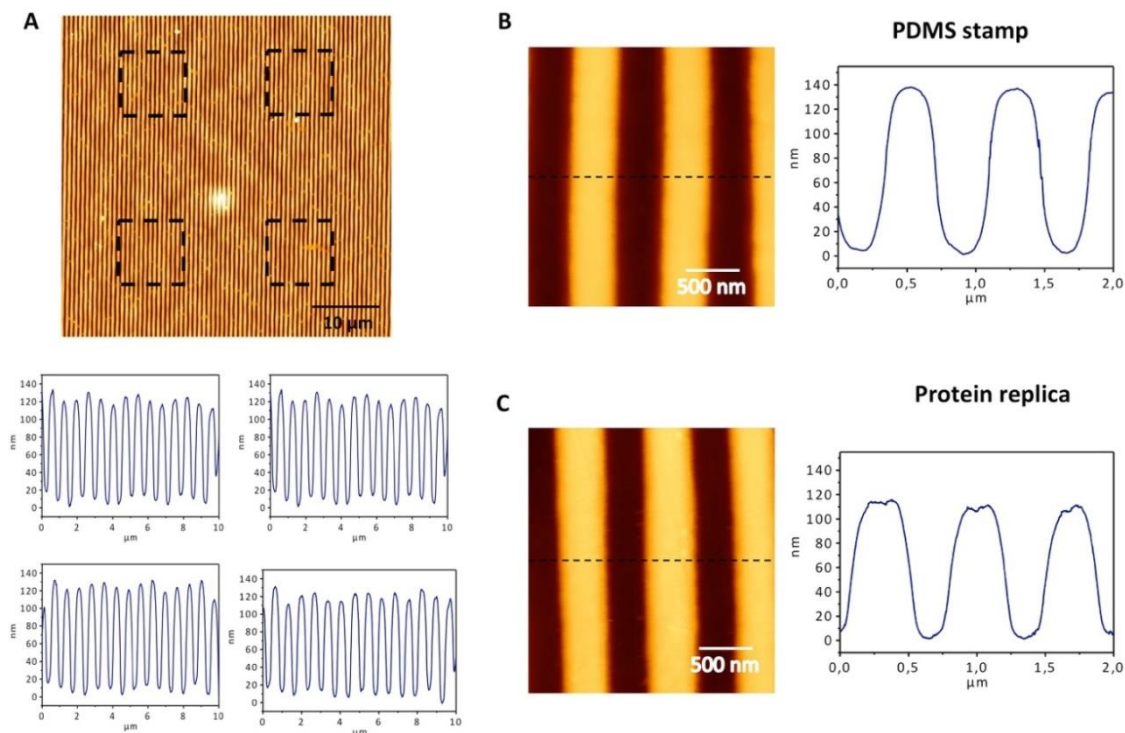


Figure 9. AFM characterization of the nanostructured protein films. For a PDMS stamp (**A**) and the protein replica (**B**), AFM images of $2 \times 2 \mu\text{m}^2$ and a height profile are shown. Cross-section of the replica shows a perfect replication of the nanopatterns on the protein film, with a height of approximately 140 nm and a periodicity of 700 nm. **C**. The top panel shows a $50 \times 50 \mu\text{m}^2$ image acquired by AFM, in which the film patterns can be observed. The black squares show the four areas of $10 \times 10 \mu\text{m}^2$ that were selected to evaluate the topography of the surface. The bottom panels show the AFM profiles of the four areas selected, revealing a regular topography, with heights around 140 nm.

The low feature variation that soft replica molding provides over the relatively large area of the nanopatterned CTPR film enables the development of uniform bioactive elements for optical applications. UV-Vis characterization showed that the film presents high transmittance values (up to 95%) across the visible region (from 300 to 800 nm) (**Figure 10A**). As expected for a protein film, absorption from the high content of aromatic amino acids was observed in the 200-300 nm range, in which the characteristic peak corresponding to the absorption of the proteins appeared at 280 nm (**Figure 10A**). These parameters are similar in patterned and non-patterned protein films, presenting in both cases the characteristic high transmission of CTPR protein films. The real part of the refractive index of the material at different wavelengths shows a characteristic tail (**Figure 10B**) with refractive index values ranging 1.518–1.552 across the visible spectrum. These optical

parameters lay in a similar range as most transparent optical glasses^[313], thus allowing the implementation of the nanopatterned CTPR films in conventional optical applications requiring from highly transparent materials with a well-defined refractive index.

Some interesting biomedical applications for these nanopatterned films involve their use in aqueous environment. In their current form, nanopatterned CTPR films quickly degrade in contact with any aqueous solution due to the high solubility and weak non-covalent interactions of the integrating proteins. This property can be advantageous for the development of transient washable devices, however for other applications there is the need of water-resistant films.

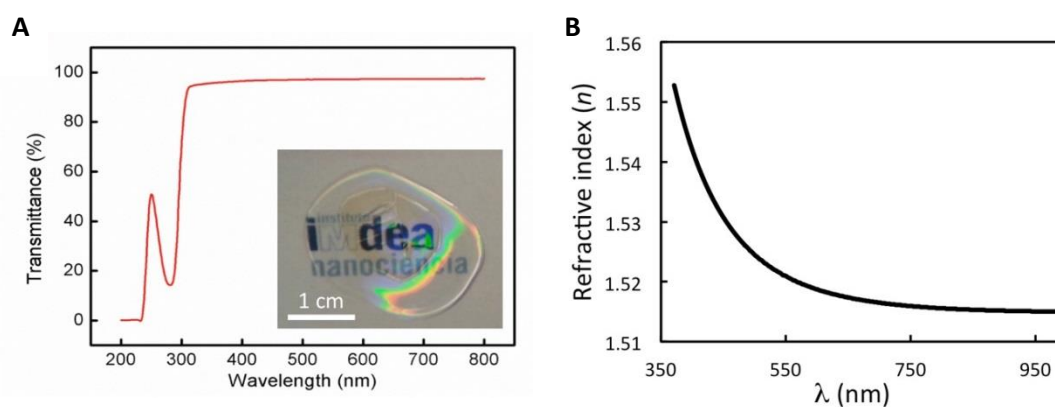


Figure 10. Optical properties of protein films. **A.** Transmittance spectrum of a nanopatterned CTPR protein film of approximately 1 μm thickness over the UV-visible range showing values up to 95%. The inset shows the high transparency of the protein film. **B.** Wavelength dependence of the refractive index of a spin-coated protein film. Plot obtained from measurements of ψ and Δ at each wavelength in the ellipsometer.

We infuse glutaraldehyde (GA) through vapor diffusion over the nanopatterned CTPR film before its unloading from the PDMS stamp to create a mild chemical crosslink across the proteins that render the nanostructured CTPR films water resistant—see experimental section for more details. We characterized the structural integrity of the nanostructures of the GA-crosslinked CTPR films using optical microscopy. The height and pitch of the nanopattern was unaltered and remained uniform throughout the entire film after GA exposition (Figure 6B), when compared to untreated films (**Figure 11A**). Likewise, optical features like transmittance and refractive index remained constant. We tested the efficiency of the chemical cross-linking process by immersing the films into a large amount of stirred warm water ($\sim 37^\circ\text{C}$) for 1 h. The structural integrity of the nanopattern CTPR film remained unaltered after this solubility test (**Figure 11C, A2-Figure 2**).

Moreover, it is worth mentioning that lamellar packing of the film is also unaltered upon cross-linking and even under moisture conditions as shown by x-ray diffraction (**A2-Figure 3**). Finally, the circular dichroism spectrum of the crosslinked film showed that mild GA crosslinking did not affect the protein structure (**Figure 11D**). Therefore, this crosslinking procedure makes it possible for these protein films to be used in applications requiring the presence of aqueous media, further expanding the potential uses of nanostructured CTPR films.

After demonstrating the possibility to control both the topology and the solubility of the CTPR films, we expand the functionality of these systems from the mere biomolecular recognition surfaces. We transformed nanostructured CTPR films into active optical component using a simple yet effective bottom-up approach consisting of the fabrication of nanostructured protein films using CTPR proteins functionalized with Rhodamine 6G (Rh6G) (**A2-Figure 4**), an efficient organic fluorescent dye commonly used in laser cavities^[314].

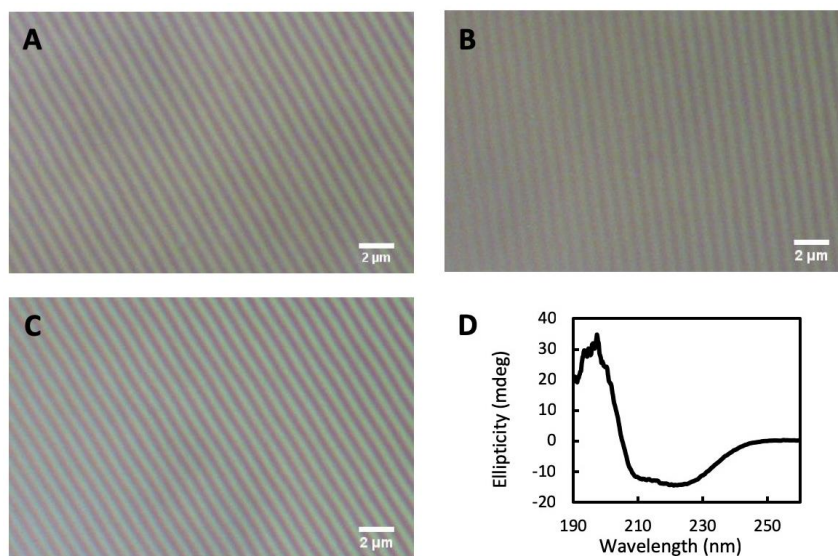


Figure 11. Crosslinking of protein films. Optical microscopy images of nanostructured protein film (A), the film after the crosslinking reaction with glutaraldehyde (B), and the crosslinked film after immersion in water (C). **D.** Circular dichroism spectrum of crosslinked proteins film showing the characteristic signal for the alpha-helical protein structure unaltered after wetting (in comparison with the non-crosslinked dry protein films, see Figure 11A).

Note that our first top-down attempt to dope CTPR films with Rh6G resulted in a heterogeneous distribution of dye molecules within the protein film, significantly decreasing their efficiency as optical elements^[311,315]. We then used a bottom-up approach to achieve the covalent attachment of the dye to the protein following a procedure that proved to be successful for the

functionalization of CTPR with porphyrins^[294,316]. The self-assembly properties of the CTPR-Rh6G conjugate proteins remained unaltered, allowing for the generation of nanopatterned protein films using the replica molding method described above. The resulting nanopatterned CTPR films exhibit structural features indistinguishable from those of the nanopatterned CTPR protein films. The emission features of Rh6G in the nanopatterned films were characterized to determine that their integration in the protein material did not hamper its function for lasing application—see experimental section for more details. Protein films with covalently linked Rh6G exhibited an excitation and emission spectra peaking at 556 and 591 nm, respectively (**A2- Figure 5**).

Both spectra resemble the corresponding of CTPR-Rh6G conjugate solutions except for slight dielectric red-shift and broadening in film, confirming minor dye aggregation in protein films (**Figure 12A**). This is also confirmed by comparing other figures like the radiative rate constants and photoluminescence quantum yields (PLQYs). In short, the PLQY of the Rh6G in solution is ca. 32 %, whereas in thin films for lasing applications a significant reduction up to < 1 % due to aggregation-induced emission quenching. In stark contrast, the CTPR-Rh6G conjugate showed a PLQY 24.5 % in solution and 17 % in thin films. In addition, time-resolved fluorescent constants are similar in solution and films for the CTPR-Rh6G conjugates, concomitant to an increase in the non-radiative decay rates in film ($6.2 \cdot 10^8 \text{ s}^{-1}$) respect to solution ($2.5 \cdot 10^8 \text{ s}^{-1}$) (**A2-Figure 6 and A2-Table 1**). Furthermore, the photostability of the films was studied under constant irradiation at 505 nm (6.6 mW/cm^2) in air, showing a remarkable stability of ca. 100 h. The mechanical stability of these films was tested taking into account optical (emission band shape and PLQY values) and morphological (roughness and crack formation) changes under bending stress (single cantilever, 0.1% strain and 1 Hz, 10,000 cycles). As shown in **A2-Figure 7**, the emission band of both the CTPR and Rh6G as well as the PLQY values hold constant upon bending tests. This is in line with the neglectable changes in the film morphology, lacking a critical change in roughness and/or crack formation (**A2-Figure 8**). Finally, the PLQY of CTPR-Rh6G film was not altered upon cross-linking and after water exposure demonstrating the optical stability and usability of the material (**A2-Figure 9**).

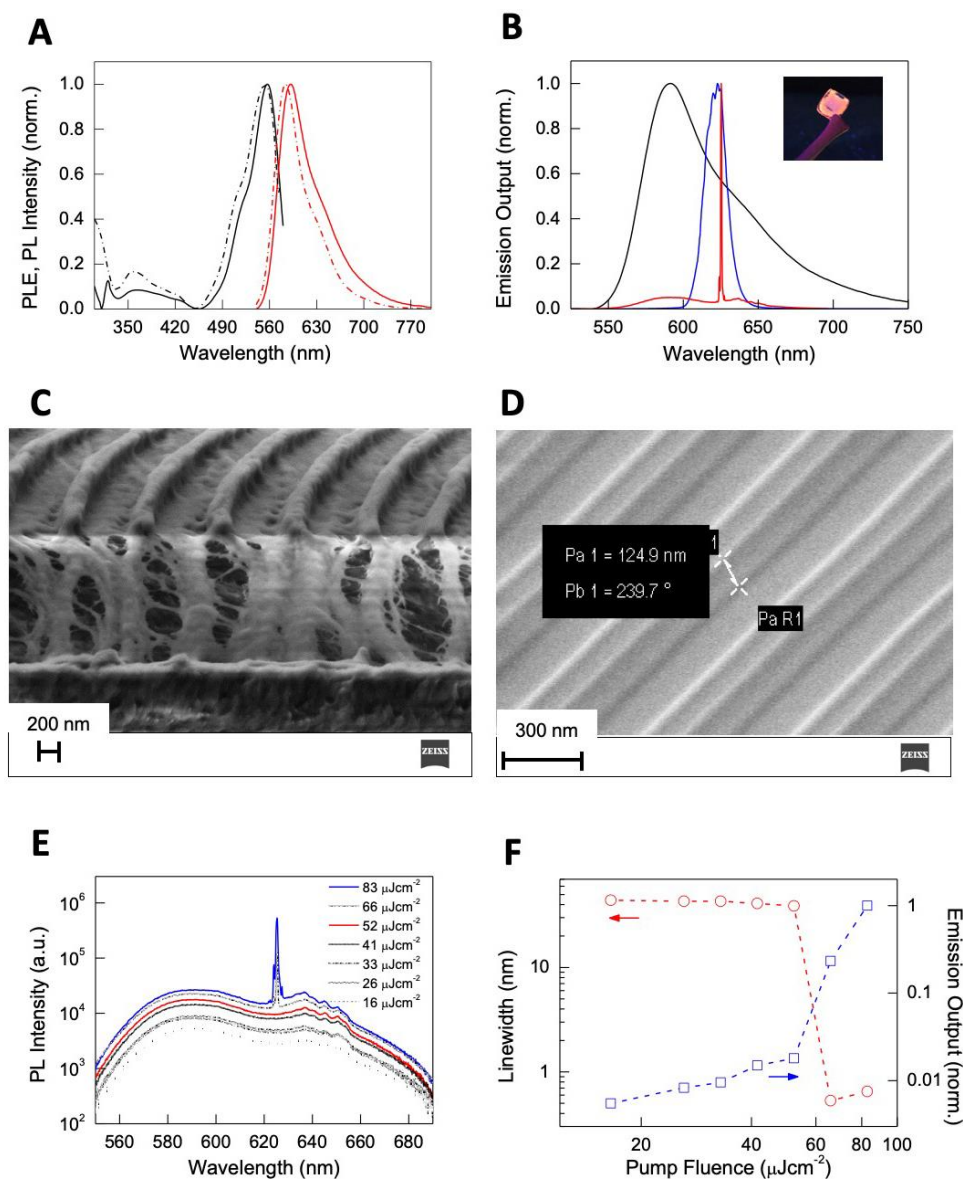


Figure 12. **A.** Normalized photoluminescence excitation PLE (black) and photoluminescence (PL) (red) spectra of CTPR-Rh6G protein solutions (dashed) and films (solid). **B.** Normalized PL (black) and ASE (blue) spectra from CTPR-Rh6G protein films and laser emission (red) from nanostructured CTPR-Rh6G protein films. Inset shows a picture of a CTPR-Rh6G film under UV illumination. **C.** Vertical cut SEM image of a nanostructured CTPR-Rh6G on top of IPS with 416 nm periodicity. **D.** SEM image of an IPS template showing lines of 125 nm height and 416 nm period. **E.** Log-lin plot of the PL spectra as a function of excitation fluence. **F.** Log-log plot of the PL linewidth (circles, left Y-axis) and emission output normalized by the output at the highest fluence (squares, right Y-axis) as a function of excitation fluence, (red and blue arrows indicate respectively their corresponding Y axis).

The emission features, photostability, and homogeneity of CTPR-Rh6G films give rise to the possibility of observing light amplification upon photoexciting the film with laser pulses. Upon pumping the protein films with a pulsed stripe (532 nm, 4 ns, 10 Hz, 3 mm x 700 μm size) above a

certain fluence threshold (2.5 mJcm^{-2}), we observe emission linewidth narrowing due to the appearance of amplified spontaneous emission (ASE) at 621 nm arising from the edge of the film (**Figure 12B**). Nanostructured protein films (**Figure 12C**) obtained by depositing the protein on IPS grating templates of 416 nm periodicity (**Figure 12D**) behaved as second order surface emitting distributed feedback (DFB) lasers leading to a sharp emission line (0.5 nm linewidth) centered at 625 nm (**Figure 12A**). The onset for laser action measured upon changing the excitation density (**Figure 12E**) indicated a linewidth collapse from 44 to 0.5 nm and a sudden change in the slope of the emission output (**Figure 12F**) at fluences above a $55 \mu\text{Jcm}^{-2}$ lasing threshold, (see Appendix 2 for a description on how the lasing threshold was obtained). This value is below those reported in DFB lasers based on chemically unbound Rh6G on different hosts (refer for instance to 1.7 mJcm^{-2} found on Rh6G-doped silk fibroin or $140 \mu\text{Jcm}^{-2}$ observed in Rh6G-doped cellulose acetate)^[261,317]. Our approach benefits from a combination of enhanced Rh6G emission in solid state and efficiently supported feedback provided by the highly defined periodical patterning^[318].

Owing to its large fluorescence quantum yield (0.94)^[319] and outstanding optical gain properties, Rh6G has been the choice as optical gain medium to develop optically-pumped lasers upon its dispersion on a myriad of organic matrices including for instance mesoporous silica^[320,321], aerogel^[322,323], latex^[324], PMMA^[325], methyl methacrylate copolymers^[326,327], cellulose nanofibers^[314] or cellulose acetate^[328,329], among many others. The solid-state biological lasing platform demonstrated in this work offers attractive assets for integration of light sources in biological medium aiming for instance at in-vivo imaging or diagnosis. Furthermore, our approach opens up possibilities to combine lasing and protein functionalities through protein engineering such as their unique recognition capabilities which can be exploited for highly sensitive and selective bio-sensors.

3.5. Conclusions

Bioinspired approaches to produce biocompatible protein-based devices are highly promising, however protein-based devices are not a reality yet. The use of bottom-up approaches to produce biocompatible protein-based surfaces has proven to be useful to fabricate variety of biomaterials^[274,330]. Unfortunately, the applicability of these protein-based materials as active devices has been limited by the difficulty to tune their microstructure using top-down approaches

without altering the self-assembly of its constituents. Here, we explored the potential of engineered proteins to develop protein-based optically active materials using a fabrication strategy that combines a bottom-up (functionalization of unit cells) and a top-down (topologically-guided self-assembly) approaches. In addition, compared to previous reports, inspired on naturally existing protein-based materials such as silk, we provide a significant step further, using engineered recombinant proteins as platforms for the generation of active materials.

We reported the generation of nanopatterned protein films using simple designed modular proteins. We achieved macroscale materials composed of structured nanoscale elements ordered across different size scale. In addition, these materials were mouldable using a cost-effective top-down soft-nanolithography technique. The protein material replicated with high fidelity the pattern of the stamp, resulting in a bio-compatible nanopatterned films. Those are flexible, easy to handle, and highly transparent. We improved the stability of the protein materials for their use in aqueous environments by mild cross-linking without affecting to the optical or structural properties of the material. Finally, we exploited the unique modularity and designability of the protein scaffold of choice to introduce an optical functional element, *i.e.* an active laser dye, in the material. This resulted in nanopatterned DFB laser based on protein thin films with good lasing efficiency.

Hence, we demonstrate a biocompatible and cost efficient technology to fabricate functional materials by a combination of bottom-up and top-down approaches. Active elements are integrated in the basic structural unit of this material, in addition to bottom up approaches to result in an ordered protein material, top-down soft nanolithography approaches can be implemented for a next level of organization. We present a cost-efficient and easy-to-follow technology for patterning nanostructured thin films using PDMS stamps that can embed different functional elements of industrial interest maintaining their functionality. This work represents a starting point to implement this technique in the future to produce protein-based materials with a set of different topologies and patterns, by using molds with different shapes ranging from few nanometres to the limits of microfabrication. Furthermore, the properties of these scaffold proteins can be easily tuned to embrace different functionalities and protein variants can easily be expressed recombinantly, making the described process versatile, affordable and scalable.

This work is a step toward the development of bioinspired multifunctional devices. Overall this work has deep implications in the design of new bioinspired devices and functional materials based on a combination of bottom-up and top-down approaches using simple protein based scaffolds. Further research is needed in order to establish the real potential of these approaches in material sciences. The application of this strategy could drive the design of next generation biomaterials following a combined bottom-up/top-down strategy and choosing between a variety of engineered proteins, shapes, topologies, and functionalities, to be applied in very diverse fields including regenerative tissue medicine, nanobiocatalysis, photonics, bioelectronics, biosupporting or biosensing.

Chapter 4

**Biocatalytic protein-based materials for
integration into energy devices**

4.1. Background

4.1.1. Nanogenerators as a source of clean energy

Energy resources such as fossil fuels, mineral fuels, nuclear, and hydroelectric sources are finite, unsustainable and/or harmful, while others such as renewable energy sources are sustainable over the relatively long term and without any impact on public health. The energy and climate crisis are forcing a change of paradigm related to the energy resources in our society. The current energetic demand is increasing exponentially due mainly to population growth and, consequently to the industrial development (*i.e.* agrarian and agricultural overexploitation) in a society more and more energy-dependent. This energetic demand is promoting the increase of pollution and global warming, and conversely cutting down the main energy sources^[331]. Therefore, new eco-friendly and renewable energy approaches to replace the existent energy demand are mandatory. Nanotechnology is arising as tool to develop new alternative sources of energy including solar cells, hydrogen generation, hydrogen storage, and fuel cells^[332,333].

Among those developments, during the last two decades new devices based on the piezoelectric effect have been developed, commonly known as nanogenerators. Those devices are able to convert mechanical energy into electric energy. Various materials have been showed to have this piezoelectric behavior, such as wurtzite materials, zinc blende materials, perovskite materials, and even polymers. In general, these materials have one main characteristic in common: dipole moments created by naturally formed positive and negative charge centers^[334]. In particular, the most common nanogenerator is, due to its high mechanical-electrical energy conversion, Lead zirconate titanate (*i.e.* $\text{Pb}[\text{Zr}_{1-x}\text{Ti}_x]\text{O}_3$ or PZT, being $0 \leq x \leq 1$), which has perovskite-type structure. Such structure presents a small cation in the center of the unit cell (*i.e.* Ti^{4+} and Zr^{4+}). The structure is slightly deformed when vibration or pressure occurs on its surface, which leads to a displacement of the cations relative to the O^{2-} . As a result of this charge displacement an electric field is built-up (**Figure 1**), and this electric field can be harnessed as electric voltage^[335].

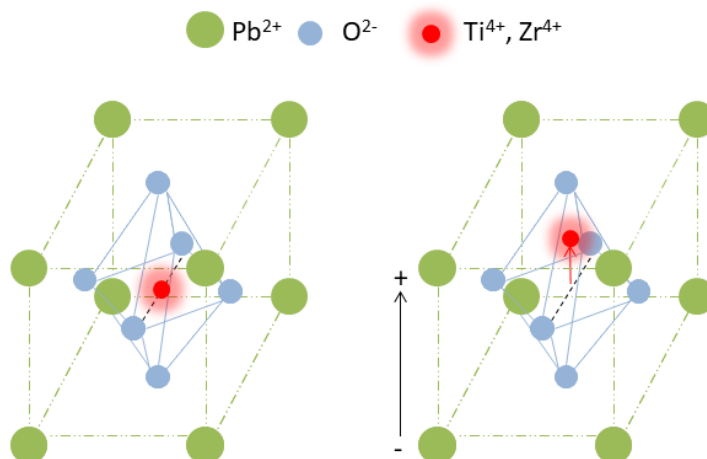


Figure 1. Unit cell of perovskite. A. Octahedron structure. B. Distortion of octahedron upon polarization.

4.1.2. Bioinorganic generator: Catalase as a source of mechanical energy

In a pioneering work researchers developed a methodology to produce eco-friendly energy from renewable fuel sources, using nanogenerators based on PZT disc (*i.e.* two electrodes, top-silver and bottom-cooper, and the PZT in between) coupled to a multi-enzymatic reaction (*i.e.* bioinorganic generator)^[336]. Unlike traditional generators, this system produces mechanical energy through enzyme-driven gas production which generates mechanical strain that is converted into electricity by the action of a piezoelectric component properly integrated into the device (**Figure 2**).

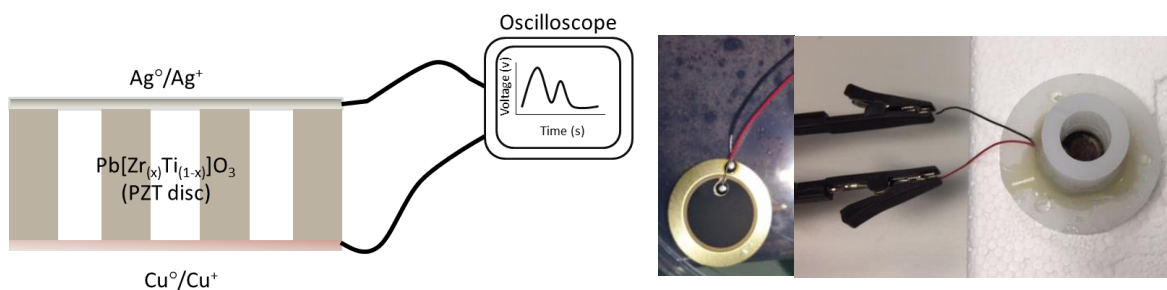


Figure 2. Piezoelectric disc and bioinorganic generator. A. Scheme of inorganic piezo-electric material composed of two electrodes (Ag/Cu) and lead zirconate titanate (PZT disc) in between. B. Optical image of the piezoelectric disc and bioinorganic nanogenerator.

The source of this gas-bubbling comes from different substrates as glucose, ethanol, or amino acids, which conversion is catalyzed by a subset of enzymes that ultimately leads to gas production as byproduct. In particular, catalase (CAT) is the main responsible for gas-releasing in the multi-

enzymatic system (*i.e.* oxidase-catalase pairs) in which oxidases as glucose oxidase (GOX), alcohol oxidase (AOX), D-amino oxidase (DAO) and L-amino oxidase (LAO) engage in the hydrogen peroxide byproduct^[336]. CAT is a well-known enzyme which catalyzes the disproportionation of H_2O_2 into water and O_2 (**Figure 3**). The oxygen-bubbles produced trigger the mechanical stimulus that prompts the electric current generation when bubbles get in touch with the PZT surface.

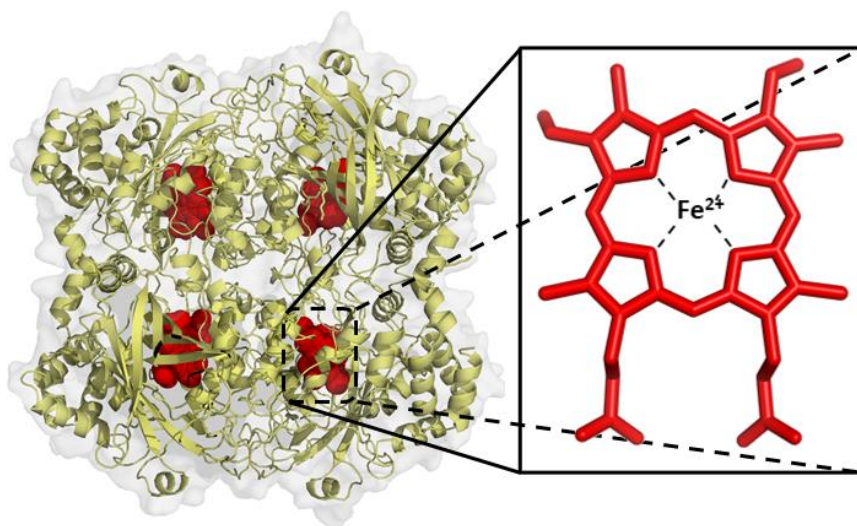


Figure 3. Three-dimensional structure of CAT consisting of 4 subunits and heme prosthetic group in each subunit shown in red spheres. Zoom in of the heme structure (PDB ID: 1TGU)^[337].

4.1.3. Enzyme immobilization

Despite the fact that energy harvesting enables to produce clean energy from a mixture of enzymes, homogeneous catalysis brings some drawbacks that can limit their usability and slow the energy production down. For this reason, an evident approach goes through enzyme immobilization. Some of the advantages of this strategy compared to homogeneous catalysis using soluble enzymes are related to the economic cost, the enzyme reusability, and the improvement in stability^[338,339]. Several methods have been carried out up to date, such as adsorption, covalent binding, affinity immobilization, entrapment or encapsulation, and enzyme cross-linking^[340,341]. Most of them require carrier matrices made of inert polymers and inorganic materials, even though alternate carrier-free immobilization has been shown to be as efficient and useful, providing the advantage of cutting down production cost and increasing enzymatic activity^[342]. However, each method displays some drawbacks and advantages, and therefore, the choice of a

particular immobilization methodology depends on the intended purpose. Moreover, the effect of a specific matrix compound may disturb enzyme activity and/or substrate diffusion^[340]. Therefore, new strategies to develop novel heterogeneous biocatalysts are desirable^[343].

In the recent decades, biopolymers have been successfully used in different fields with the aim to develop cost-efficient and sustainable processes. These approaches require properties such as biocompatibility, biodegradability, and nontoxicity^[344,345]. In this context, proteins can serve as a basis of the polymeric supports because, apart from fulfilling all the aforementioned requirements, they can also provide diverse reactivity and specific environment suitable for the enzyme. Moreover, the use of proteins as scaffolds will potentially allow the control over the spatial organization of active elements without drawbacks present in synthetic materials. In particular, tetratricopeptide proteins (TPR) have been demonstrated to be an exceptional scaffold since consensus TPR (CTPR) proteins form ordered films, due mainly to the side-to-side and head-to-tail interactions, which can also be observed in the crystal structure^[176,346]. Therefore, scaffolds and materials composed of CTPR proteins show a great potential for the ordered entrapment and immobilization of enzymes toward the generation of novel heterogeneous biocatalysts. In particular, in this chapter the catalase immobilization in CTPR proteins films is explored as a new approach for its implementation in the harvesting eco-friendly and renewable energy through PZT disc.

4.2. Introduction

Large efforts are currently being made in the field of fabrication of new functional biomaterials and their integration into technological devices^[347–350]. A variety of bioinspired strategies have recently emerged to create biomaterials with tailored functionalities, improved properties and potential uses^[347,351–353]. These strategies include the bottom-up approaches for the generation of supramolecular biomaterials^[2], with particular efforts devoted to achieve protein-based materials due to the amazing structural and functional diversity of these biomolecules^[351–355].

Of particular interest to the field of active biomaterials is the fabrication of catalytic materials in which active enzymes are immobilized^[356]. Several immobilization methods have been used up to date, including adsorption^[357], covalent linkage^[358], affinity immobilization^[359], entrapment^[360], encapsulation^[361], or enzyme cross-linking^[362]. Among them, the simple entrapment offers easy fabrication and handling and endows high stability to the immobilized enzymes^[363]. Regarding the

support, using natural materials as scaffold provides advantages as biocompatibility, chemical versatility, and biodegradability that organic or inorganic support materials do not offer. In this regard, proteins play a key role since they fulfill all these characteristics and their use for the fabrication of protein-based materials has been already demonstrated^[355,364]. However, the robust fabrication of functional protein-based materials films that preserve both structural integrity and functionality of the entrapped enzymes remains a challenge in biomaterials research. In fact, few examples of enzymes immobilized on protein-based materials have been successfully reported up to now^[365].

Several scaffolding proteins can be used for the fabrication of biomaterials. However, engineering proteins provide clear advantages in terms of tunability, reproducibility, scalability and rational design of the final properties of the material^[349]. Modular building blocks with simple interactions allow for better control of the final assemblies through the implementation of bottom-up approaches. Engineering repeat proteins present these inherent features that make them suitable candidates to be used as scaffolding proteins^[253,366]. In particular, tetratricopeptide proteins (TPR) have proven as exceptional scaffolds since consensus TPR (CTPR) proteins form ordered films, due to well characterized side-to-side and head-to-tail interactions^[253]. The basic CTPR unit consists of 34 amino acids with a helix-turn-helix motif. CTPR proteins have a modular structure in which the repeats can be combined in tandem to form highly stable CTPR proteins that display a right-handed superhelical structure, with eight repeats per one full turn of the superhelix^[96,102]. These features make these repeat protein scaffolds ideal building blocks for numerous applications^[90,367], as previously demonstrated through the fabrication of functional protein-based materials^[105,106]. Similarly, we hypothesize that materials based on CTPR proteins will be applicable for the ordered entrapment and immobilization of enzymes toward the generation of novel heterogeneous biocatalysts readily integrated into devices.

Catalase (CAT) is an excellent candidate to be entrapped into protein-based materials since is extensively used for technological applications where biocatalyst robustness is often demanded. CAT catalyzes the hydrogen peroxide disproportionation releasing water and molecular oxygen as innocuous products^[368].

Such catalytic reaction makes this enzyme industrially relevant for the development of biosensors^[364], preventing food oxidation^[369], removing hydrogen peroxide from residual

water^[370], and intensification of oxidase-driven biotransformations^[371,372]. In a pioneering attempt to expand the CAT applications, our group has recently exploited CAT in solution to produce bubbling upon H₂O₂ disproportionation reaction as a source of mechanical energy then harvested by coupled piezoelectric materials to generate electricity^[357].

Since the described system integrated a soluble CAT that formed bubbles within a reaction chamber, the reaction mixture, and consequently the enzyme, must be removed once the fuel (H₂O₂) is consumed and maximal energy is produced. Moreover, the soluble enzyme normally becomes inactive after one operational cycle after being exposed to the high concentration of H₂O₂ required for the energy generation process. Hence, the current bio-inorganic generator is limited to only one cycle of energy generation, which precludes the reusability and the continuous operation of the system. In this emerging field, enzymes could play a key role since they are able to catalyze reactions whose by-product may be used as source of mechanical energy. However, the coupling of enzymatic systems and nanogenerators would require automatic, independent and reusable systems so as to minimize costs and enhance the efficiency. For the aforementioned reasons, the physical immobilization of CAT on the surface of the piezoelectric material would make the enzyme more robust and recyclable, overcoming the major limitations of the current system for energy harvesting and ease the automation and integration of this bio-inorganic generator into more complex devices. Although enzyme immobilization is often considered as one of the most effective methods to increase the biocatalyst robustness, the preservation of the enzymatic activity into the materials during the immobilization process is still a challenge^[373]. This limitation arises mainly from loss of catalytic activity due to enzymes undergoing denaturing conformational changes, intermolecular aggregation, steric hindrance of the active sites, lack of dynamical freedom, and mass transport restriction of reactants imposed by the structure of the solid materials^[374]. In addition, depending on the immobilization methodology the enzyme might be leached to the reaction media resulting in activity loss of the immobilized biocatalyst. Hence, the immobilization of enzymes on solid materials shall be optimized according to their final use, seeking for protocols that maintain the activity and increase the stability relative to the enzyme in solution.

To advance in the fabrication of novel bio-inorganic generators based on CAT, this chapter describes the development of a novel protein-based biomaterial that can be readily coupled with piezoelectric materials to increase the operational life span of the energy harvesting process. This

increased life span has been possible because the protein environment of the CTPR scaffolding protein forming the biomaterial stabilized the entrapped CAT as demonstrated by thermal inactivation studies. The solid self-standing biomaterial with catalase activity was casted into a piezoelectric disc and proven to produce electricity from H₂O₂. Although the entrapped CAT presents lower apparent catalytic efficiency than the enzyme in solution, the proximity of the bubbling enzyme to the piezoelectric surface improves the energy outcome at large operational volumes compare with the system using the enzyme in solution.

4.3. Experimental section

4.3.1. Materials

Reagents and substrates including the hydrogen peroxide and 2,2'-azino-bis(3-ethylbenzothiazoline-6-sulfonic acid (ABTS), and the enzymes catalase (CAT) from bovine liver and horseradish peroxidase (HRP) were purchased from Sigma-Aldrich (St. Louis, MO). The piezoelectric material (PZT disc) (diaphragm, 6.3 kHz, 1 K Ω , 0.01 μ F, 20 mm \times 0.42 mm, cat. 7BB-20-610, Murata) was acquired from Farnell Element14 Components (Barcelona, Spain).

4.3.2. Protein expression and purification

The gene encoding CTPR10 protein was previously generated based on a consensus CTPR protein and cloned into the pPROEX-HTa vector for the expression as a His-tag fusion for affinity purification^[97,375]. The protein was expressed and purified as described previously^[102]. Briefly, the plasmid was transformed into BL21 (DE3) *Escherichia coli* and the cells were grown in LB with 0.1 mg/ml of ampicillin in agitation to an O.D. between 0.6 and 0.8. Protein expression was induced with 0.6 mM IPTG for 5 hours at 30°C, then the cells were centrifuged at 4500 rpm and resuspended in 300 mM NaCl, 50 mM Tris pH=8.0 Lysis buffer with 1 mg/ml of lysozyme, 5 mM β -mercaptoethanol, and 15 μ l DNase stock solution. The resulting lysate was sonicated during 5 minutes with 30 second intervals and 40% of amplitude, and centrifuged at 10000 rpm for 45 min. Protein purification was performed by affinity chromatography using Ni²⁺ His-TrapTM column. The eluted protein was dialyzed overnight in PBS (150 mM NaCl, 50 mM phosphate buffer pH=7.4 with 2.5 mM β -mercaptoethanol). The protein was concentrated and purified by FPLC gel filtration chromatography over a Superdex 75 HiLoad column. Fractions containing the protein were analyzed in 15% acrylamide gels to confirm the purity of the protein. Finally, protein was

concentrated until the desired concentration, from 50 to 400 μM , using the estimated molar extinction coefficient at 280 nm from the amino acid composition.

4.3.3. Protein thin films fabrication

A 20 μl protein solution of 400 μM CTPR10 (18.1 mg/ml) and 4 μM CAT (1 mg/ml) were deposited over a hydrophobic non-porose material by drop casting and left to dry for at least 4 hours at room temperature to ensure the formation of the protein thin film. A second approach to obtain thinner films was using spin-coating to deposit the films. In this case, a drop of 15 μl of 400 μM CTPR10 and 4 μM CAT were deposited over a quartz slide of size 1x1 mm^2 by spin-coating method using a Laurell Technologies corporation Model WS-400B-6NPP/LITE, at 1000 rpm for 10 min with an acceleration of 3000 rpm/s. Stereomicroscope LEICA S8APO was used to image of the biomaterial at macroscopic level.

4.3.4. Scanning electron microscopy (SEM)

SEM JEOL JSM-6490LV was used to image the surface of the protein thin film. The film was mounted over a carbon tape and imaged under vacuum conditions, applying an electron high tension (EHT) of 5.00 Kv WD of 2.5 mm and an aperture size of 15 μm . Sputter coating technique was performed in all samples using a metallization of Au/Pd alloy.

4.3.5. Circular dichroism

Circular dichroism (CD) was used determine the secondary structure of the CTPR10 units within the films. CD was performed using a Jasco J-815 spectropolarimeter. The solid films were deposited on a sandwich quartz cuvette (0.1 mm path length) by spin coating. The CD spectra were acquired at 1 nm increments and 10 seconds average time over a wavelength range of 190 to 260 nm.

4.3.6. Crosslinking of the protein thin films

Glutaraldehyde (GA) at 1% was used as crosslinking agent for a gentle vapor diffusion crosslinking^[376,377]. The reaction was carried out in wells of 1 ml for 24h at room temperature. At bottom of well 500 μl glutaraldehyde solution were added while the protein film was fixed on the cover slip used to seal the well. After the reaction, the films were recovered and, in order to evaluate the cross-linking efficiency, dipped into water solution to monitor the potential release

into the solvent. The biomaterial was dipped into a water solution for different times, 1h, 24 h, and one week and the amount of protein in the supernatant was quantified at each time by Bradford assay using the spectrophotometer Varioskan Flash spectral scanning multimode reader (Thermo Scientific).

4.3.7. Distribution of CAT in thin films by fluorescence imaging and fluorescence anisotropy

CAT was fluorescently labeled using rhodamine B isothiocyanate (Sigma-Aldrich). The labeling reaction was performed for 24 h at 37°C under constant shaking. The enzyme was purified from the free dye by a NAP-5 column (GE Healthcare) and concentrated with Amicon® ultra-0.5 ml centrifugal filter MWCO 10K (Merck Millipore). The enzyme concentration was calculated measuring the absorbance at 280 nm ($\epsilon_{280\text{nm}} = 246000 \text{ M}^{-1} \text{ cm}^{-1}$) using a UV-vis spectrophotometer (ThermoFisher). Fluorescence confocal microscope (ZeissNLO 880) was performed to determine the homogeneity of the biomaterial CAT-rhodamine labeled. The image was acquired using an excitation wavelength of 550 nm and with a magnification of 20x. The z-stack for the 3D reconstruction was acquired with 40x oil objective using an excitation of 561 nm and emission between 565-700 nm, 40 μm Z-slides and an Airyscan detector at maximum intensity projection and 512x512 frames. Fluorescence anisotropy of the solid film was measured using a fluorimeter Perkin Elmer (LS55) with automated polarizers. A film of CTPR10 and CAT labeled with rhodamine was used and the polarization was determined using excitation and emission wavelengths of 550 and 572 nm, respectively.

4.3.8. Enzymatic activity measurements

The catalase activity either in solution or in the thin protein film was indirectly analyzed by quantifying the amount of hydrogen peroxide produced along the time. Samples of the catalase reaction were withdrawn at different times and incubated with peroxidase and ABTS ($\epsilon = 36000 \text{ M}^{-1} \times \text{cm}^{-1}$) for a fixed time. Herein, the peroxidase (HRP) uses the catalase-produced H_2O_2 to oxidize ABTS increasing the absorbance of the reaction mixture at 420 nm. The increase in absorbance was measured using a Varioskan Flash spectral scanning multimode reader (Thermo Scientific) and quantified to determine the H_2O_2 concentration upon the catalase action. For the soluble enzyme, 20 μl of the enzyme at 0.01 mg/ml was mixed 980 μl of substrate solution (35 mM H_2O_2 in 100 mM phosphate pH 7.4), aliquots of 50 μl was collected at different times and heated at 90°C for 2 min in order to inactivate the enzyme. Upon enzyme inactivation, 20 μl of each sample were mixed

with 200 μl of 0.066 mg/ml ABTS and 0.013 mg/ml HRP in 100 mM phosphate pH 7.4 at room temperature and incubated for 5 min. In the case of the immobilized catalase, a sample of supernatant (20 μl) from the film incubated with substrate solution was mixed with 200 μl of 0.066 mg/ml ABTS and 0.013 mg/ml HRP in 100 mM phosphate pH 7.4 at room temperature and incubated for 5 min. The hydrogen peroxide consumed in the reaction was calculated using calibration curve. The specific activities of both in solution and entrapped CAT were determined from the time-course curves obtained through monitoring the H_2O_2 concentration along the time (Figure S3). The initial reaction rates were obtained from the slope of the curve, considering a zero-order kinetic, and converted to specific activity considering the total amount of enzyme tested. The kinetic parameters of the immobilized and in solution catalase were determined by measuring the reaction rates at various H_2O_2 substrate concentrations ranging from 0.25 to 168 mM at pH of 7.4, while keeping the amount of enzyme constant. The kinetic parameters K_m and V_{max} were calculated from Michaelis-Menten fit. To determine the thermal stability of the enzymatic activity, incubations at 50°C at different times were carried out to measure the decay of activity. The activity of each sample withdrawn at each inactivation time was measured through the HRP-coupled colorimetric assay described above and fixing the catalase reaction time in 15 and 3 minutes for the immobilized and soluble enzyme, respectively.

4.3.9. Electric Energy Output Measurements

SiO_2 thin films were deposited with nonreactive and reactive magnetron sputtering on PZT disc (1.25 cm^2 active piezoelectric surface) using an AJA-ATC 1800 system with a base pressure of 10^{-7} Pa. The deposition of the films was done with three separate 2 inch elemental targets, with a purity of 99.999% for carbon (Demaco-Holland), 99.95% for Nb (AJA International-USA) and for SiO_2 , in a confocal configuration at a pressure of 0.25 Pa of pure Ar. The substrate bias voltage and substrate holder heating facility were turned off during depositions; the distance between target and substrates was about 15 cm. Prior to deposition, the substrates were sputter-cleaned with a negative bias of 180 V (25 W) in a 4 Pa Ar atmosphere for 10 min. SiO_2 films were deposited in an Ar/ O_2 atmosphere (10 sccm Ar + 20 sccm O_2) at total pressure of 0.4 Pa and applying a d.c. power of 230 W to the Si target. CAT-protein thin films were deposited over the SiO_2 on the PZT surfaces and connected to an oscilloscope (Siglent model SHS806) to monitor the open-circuit voltage versus time as described before^[378]. Different chamber volumes were obtained by varying the liquid fuel volume inside the open chamber (0.2, 0.4, 0.6, 1, 1.5 and 2 mL). When in solution

enzyme was assessed, an enzyme solution that contained catalase in 50 mM sodium phosphate buffer at pH 7 was placed inside the chamber. The reaction was initiated by the addition of the fuel, H₂O₂ at the indicated concentrations. Before triggering the reaction, the system was equilibrated until the voltage signal reached 0 V. The energy of the electrical outputs according was calculated with eq. 1^[379].

$$E = \int_{t_1}^{t_2} \frac{V^2(t)}{R} dt$$

Where E , is the generated electrical energy and V is the generated voltage from the start (t_1) to the end (t_2) of a cycle at a constant resistance load (R). The R value was fixed to 60 M Ω (experimentally determined at the maximum produced voltage by the enzymes).

4.4. Results and Discussion

4.4.1. Protein-based biomaterial fabrication and characterization

Here we report the fabrication of a bioactive material based on the self-assembly of CTPR proteins which irreversibly entraps CAT as functional unit and its casting on piezoelectric materials to give rise the new generation of energy harvesting devices based on the previously reported ones (**Figure 4A**)^[378]. The formation of this active biomaterial relies on the self-assembling properties of CTPR and its ability to form self-standing ordered protein thin films. As previously described by our group^[253], the protein thin film fabrication requires 3% (w/v) protein concentration of a CTPR10 variant (a consensus CTPR protein with 10 identical repeats) to ensure the appropriate packing and handling of the resulting film. The biocatalytic protein film was prepared under these conditions by homogeneously mixing the CTPR10 and CAT in the selected ratios, and then casting the film through two different strategies: using spin-coating in a piece of quartz, or using drop casting method over a hydrophobic material (see experimental section for further details) (**Figure 4A,4B**). The resulting self-standing protein films quantitatively entrapped CAT and led to a stable, flexible, easy to handle and transparent material (**Figure 4B**). The homogeneity and surface uniformity of the material is evident from the SEM image (**Figure 4C**), and the SEM cross-section images revealed a thickness of approximately 20 μm for these fabrication conditions (**Figure 4C, A3-Figure1**). Expectedly, the functionalized protein film showed

a peak at around 400 nm that corresponds to the maximum absorption of heme group of the catalase, which provides the film a light green color (**Figure 4D**). The CD spectrum of the protein film entrapping CAT shows the characteristic signal of the alpha-helical structure of the scaffolding protein that agrees with results previously observed by our group where the secondary structure of the CTPR10 is preserved^[253]. CD data are only revealing the secondary structure of CTPR since the protein stoichiometry in the film is 1:100 CAT:CTPR, thus being the contribution of the CAT to the CD spectrum negligible (**Figure 4E**).

It is well-known that CTPR proteins present intrinsic properties to form nanostructured ordered films since they macroscopically align by head-to-tail and side-to-side interactions^[88,96]. However, the mobility and order of entrapped enzymes in the biomaterial is unknown. To shine light on these two parameters, fluorescence polarization studies were performed by firstly labeling the amine groups of CAT with the fluorescent dye rhodamine. Through fluorescence microscopy, we demonstrated that entrapped CAT is homogeneously distributed across the protein film (**Figure 5A**). Moreover, we showed by confocal microscopy that the CAT is also homogeneously distributed throughout the film thickness (**Figure 5B, A3-Figure 2, A3-Figure 3**). To show the tumbling freedom and potential order of the CAT in the biomaterial (**Table 1**), fluorescence anisotropy was measured, observing that catalase-rhodamine conjugate in solution showed a higher anisotropy than free rhodamine as expected from its larger mass. Interestingly, rhodamine-labeled CAT entrapped into the solid protein film presented a large anisotropy value, which indicates that the confined enzyme is significantly less mobile than its in solution counterpart. Next, the organization of CAT within the protein film was determined by measuring the fluorescence of the rhodamine-labelled enzyme with plane polarized light. The fluorescence intensity changed when the excitation and emission polarizers were move from horizontal to vertical. These changes indicate that labeled CAT entrapped into the protein film exhibits a directional macroscopic order within the material; that order is imposed by the anisotropic arrangement of the CTPR scaffolding protein (**Figure 5B**).

The ordered self-assemble material as described above is soluble in aqueous media since it is formed mainly due to the non-covalent interactions between CTPR proteins, which are too weak to maintain the integrity of the macrostructure. For operational purposes the disassembly of the film and the lixiviation of the entrapped protein need to be minimized. Therefore, the biomaterial was cross-linked using glutaraldehyde at 1% for 24 h by means of vapor diffusion method to result

in a material stable in water. Upon cross-linking the biomaterial was immersed into a buffer solution and showed no lexiviation of the protein in the medium, keeping more than 95% of protein upon 7 days of immersion, which indicates an effective crosslinking (**Figure 6A**). Moreover, the mild crosslinking reaction did not affect the structural properties of the protein as it is shown in the dichroism spectra, thus the material is expected to also preserve the activity after the reaction (**Figure 6B**).

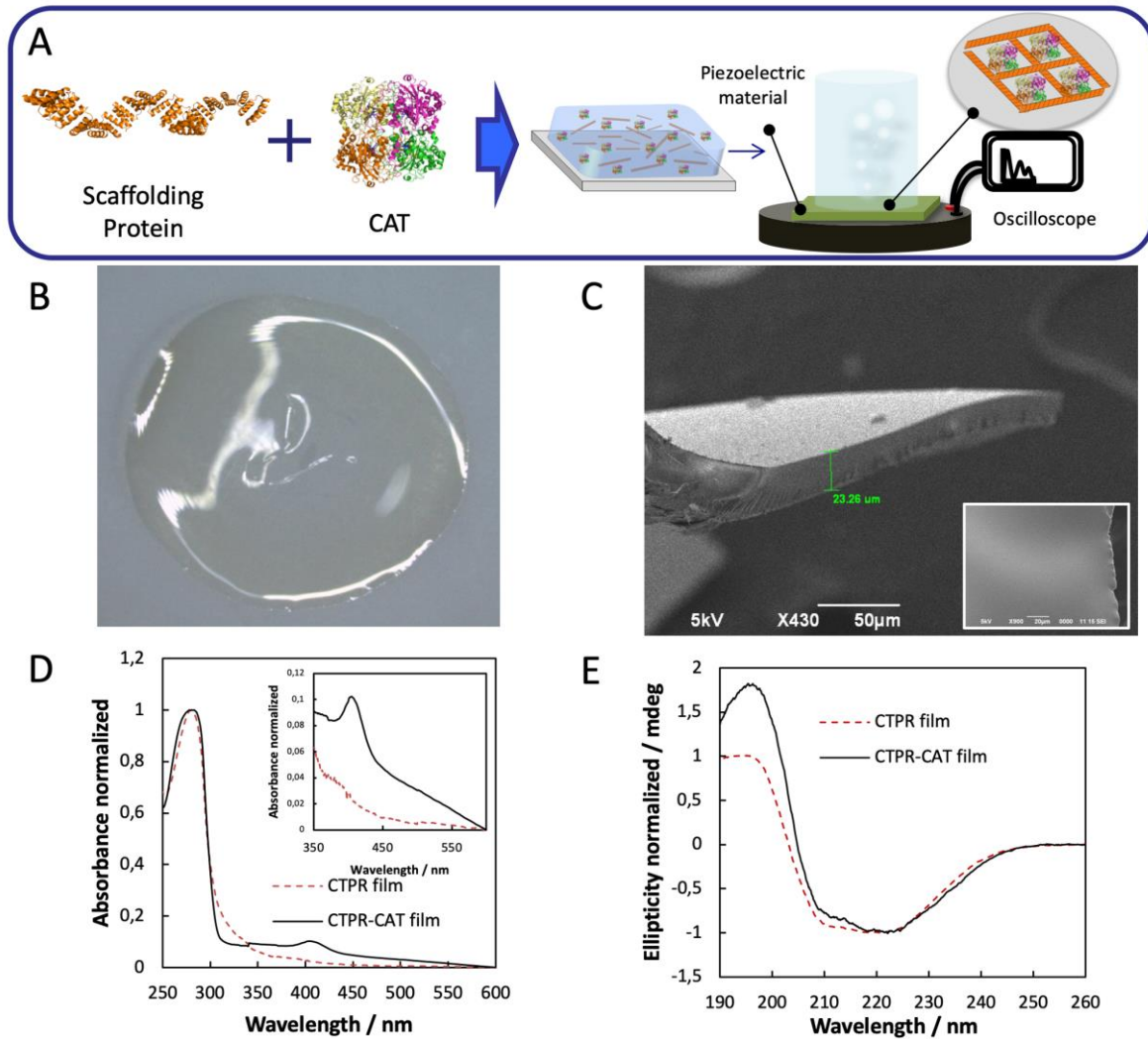


Figure 4. Catalytic protein-based biomaterial composed of CAT and scaffolding protein (CTPR). A. Schematic representation of the generation of the protein-based catalytic biomaterials and their coupling with piezoelectric discs to fabricate a second generation of bio-inorganic generators. B. Optical microscopy image of the protein thin film. C. Scanning electron microscopy (SEM) image of the protein thin film showing the cross section and thickness of the film and the surface in the inset. D. Absorbance spectra of protein films of scaffolding protein (dashed red line) and the CAT containing thin films (solid black line). The inset shows a zoom in the region of the absorption band of heme group. E. Circular dichroism spectra of nanostructured CTPR protein film (dashed red line) and the thin film with CAT entrapped (solid black line).

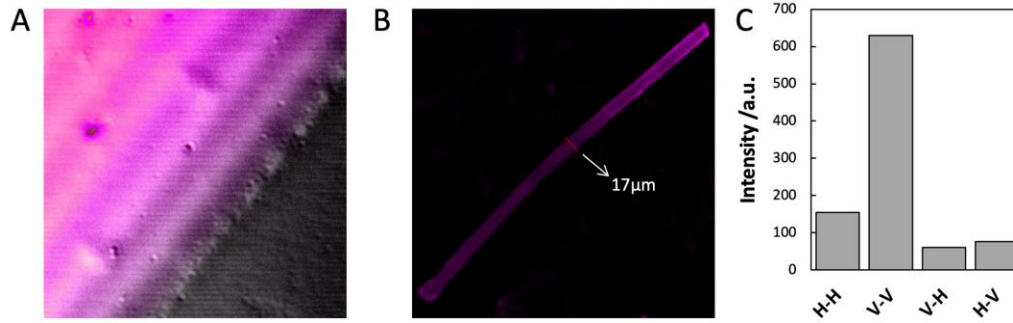


Figure 5. Fluorescence characterization. A. Overlay of the bright field image and the confocal fluorescence image of the biomaterial generated using rhodamine labeled CAT. B. Intensity of fluorescence depending on the polarizing direction.

Table 1. Fluorescence anisotropy measurements of CAT in solution and in solid film with the standard error of the mean.

Sample	Anisotropy
Rh control	0.052 ± 0.006
CAT-Rh solution	0.166 ± 0.003
CAT-Rh film	0.819 ± 0.001

4.4.2. Activity and stability of CAT entrapped into the CTPR protein film

The functional properties (activity and stability) of CAT immobilized on the protein-based material described above were determined through an indirect colorimetric assay coupling peroxidase to titrate the concentration of H_2O_2 upon the CAT action.

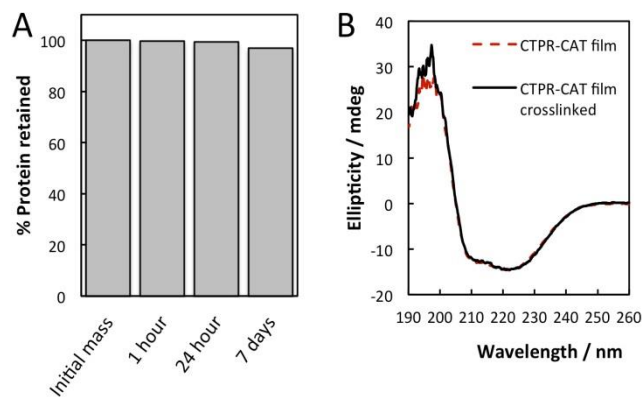


Figure 6. Crosslinking of the CAT-biomaterial. A. Percentage of protein retained in the cross-linked material after incubation in solution. B. Circular dichroism spectrum of biomaterial before (dashed red line) and after the crosslinking reaction (solid black line).

The enzymatic activity was assayed at room temperature for the biomaterial and the enzymatic solution in the same conditions. It is worth mentioning that the swelling of film was observed upon immersion into the aqueous solution, a 0.5 mg film absorbed approximately 1 μl of water. The apparent specific activity of the entrapped CAT was 0.08 Umg^{-1} compared to the 6.7 Umg^{-1} observed for the enzyme in solution under the same experimental conditions. Moreover, the activity for different film thickness was evaluated keeping CAT:CTPR ratio constant. These results showed that the total catalase activity is maximized when using the standard thickness of 20 μm , thicker films showed lower activity and significantly lower specific activity (**A3-Figure 4**). Additionally, the apparent kinetic parameters (K_M and V_{max}) of the immobilized enzyme were determined through a Michaelis-Menten fit (**A3-Figure 5**) and compared to the values calculated for the soluble enzyme under the same conditions. Table 2 shows that the apparent K_M and k_{cat} for the entrapped CAT towards H_2O_2 were 3.6-fold higher and 370 times lower than for the soluble enzyme, which resulted in that the confinement and cross-linked of CAT within the protein biofilm decreased the catalytic efficiency 1519 times. According to the specific activity and apparent kinetic parameters of entrapped CAT, the crowded environment of the protein film may limit the conformational flexibility of entrapped CAT to perform catalysis. Moreover, the higher apparent K_M values of entrapped CAT suggest mass transport issues that may hamper the diffusion of substrates towards the enzyme active sites. These issues can be related to 1) the enzyme entrapment in the compact protein film that makes it less accessible to the medium^[380]; and/or 2) the bubbles generated on the surface of the material by the oxygen released during the reaction that hamper the substrate diffusion^[381]. These bubbles grow over the surface and due to the hydrophilic nature of the protein material, the bubbles stay at the film-solution interphase, thus hampering the diffusion of the substrate properly. In addition, this change in activity could be partially attributed to the loss of catalytic activity due to the immobilization or/and the crosslinking processes. Noteworthy, the time-course curves show a lag-time of around 400-500 sec when the CAT is entrapped, while that lag is not appreciated in the time-course of the soluble enzyme (**A3-Figure 6**, **A3-Figure 7**). Mass transfer issues are also supported by loading experiments where specific activity of entrapped enzymes linearly increases with the reduction of CTPR:CAT ratio (**A3-Figure 8**). Total apparent activities of films with different ratios are similar, but the specific activity of lower ratio is dramatically reduced. It seems that under high load conditions, the substrate molecules can not reach all the entrapped enzyme molecules due to transport limitation rather than conformational changes related to the entrapment or crosslinking.

A population of inaccessible enzyme molecules might explain the low catalytic efficiency observed for the entrapped CAT. Lower CAT loadings ameliorate this effect since a larger enzyme population actively participates in the H₂O₂ disproportionation because of the improved substrate accessibility. These diffusional restrictions have also been observed when CAT is randomly aggregated and irreversibly cross-linked in presence of a feeder protein through cross-linked enzyme aggregate (CLEA) technology^[382]. Unlike the entrapment into thin protein films, CLEAs of CAT have not proven the order of the enzyme within the solid material as demonstrated in this work using scaffolding proteins.

Table 2. Kinetic parameters of CAT in solution and in the solid protein thin film. * Apparent parameters.

Sample	K_M / mM	V_{max} / mM s ⁻¹	k_{cat} / s ⁻¹	k_{cat}/K_M / s ⁻¹ mM ⁻¹
CAT in solution	84.02 ± 31.46	10.21 ± 2.74	2.55x10 ⁶ ± 0.68x10 ⁶	3.04x10 ⁴ ± 1.40x10 ⁴
CAT in film	301.89 ± 175.12	0.24 ± 0.10	6000 ± 2500	19.87 ± 14.19

In spite of exhibiting low catalytic efficiency, the entrapped CAT is still active enough for further applications, illustrating the potential and biocompatibility of this simple immobilization strategy. To assess the robustness of the functional biomaterial, we first tested the thermal stability of the entrapped CAT in comparison with the soluble enzyme. Figure 7 shows that the immobilized CAT was significantly more thermostable than its soluble counterpart since it retained approximately 100% of its initial activity after 3 hours incubation at 50°C while the soluble enzyme lost 70% of its initial activity under the same inactivation conditions, which represents a stabilization factor of 3.5. Accordingly to other immobilization protocols, CAT could be stabilized by entrapment CTPR-protein thin films demonstrating its potential as heterogeneous biocatalyst able to be reused for several operational cycles^[383].

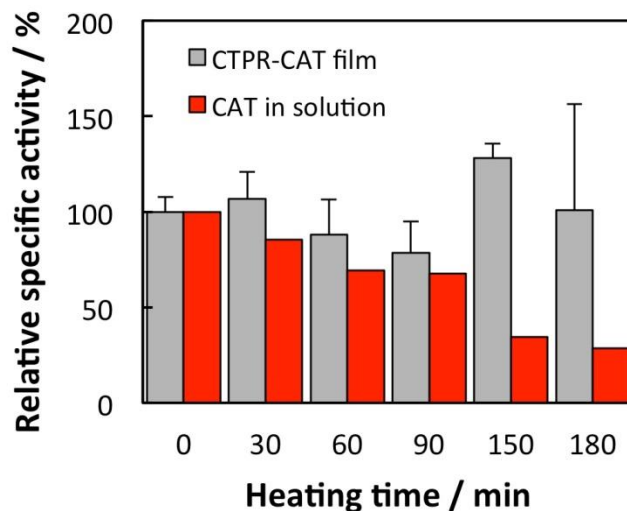


Figure 7. Enzymatic thermal stability of CAT in solid thin film (black) and in solution (red).

4.4.3. Energy output measurements

Recently, our group described the production of electric energy from chemical energy by using bioinorganic generators^[378]. Such devices are able to convert the chemical energy stored in renewable molecules (as carbohydrates, aminoacids, alcohols, etc) into mechanical energy (in form of gas bubbles) which is further harvested by a piezoelectric material based on PZT disc (Lead zirconate titanate) and transduced into open circuit voltages that are finally transformed into an energy using an oscilloscope. This concept has proven using soluble catalase that disproportionate hydrogen peroxide into oxygen and water, forming oxygen bubbles that trigger a mechanical stimulus further harvested by the piezoelectric material. The drawback of the reported system is its disposal character that avoids the enzyme reutilization after one energy generation cycle. To make these systems reusable, protein films entrapping CAT were casted at the surface of the piezoelectric surface coated with a nanometric inorganic layer with the aim at fabricating bioinorganic generators that can be repeatedly used for the continuous production of electric energy to achieve a more sustainable process. Hence, we entrapped soluble catalase into a CTPR film that is subsequently cross-linked with glutaraldehyde as above described. Primarily, we assessed the effect of coating of the piezoelectric surface with CTPR protein layer on the energy outcome. Using the soluble enzyme as catalyst, we observed that the energy generated was reduced only 25% regarding to the naked piezoelectric surface, demonstrating that the

biomaterial layer slightly affects the performance of the piezoelectric surface, but still allows the conversion of mechanical into electrical energy. When the CAT was entrapped in the protein film, the energy outcome (at 750 mM H₂O₂) was 70 nJ x cm⁻²; a value 3 and 1.6 times lower than the soluble enzyme acting over the naked piezo and the piezo casted with the protein film, respectively (**Figure 8A**). The optimal fuel concentration for the system using the soluble enzyme was 50 mM H₂O₂ whereas the system with the immobilized enzyme required 750 mM H₂O₂. In spite of that lower output and the more fuel demanded, the entrapment of the catalase enables its repeated use, maintaining more than 50% of the initial energy production after 10 energy generation cycles, replacing the fuel (H₂O₂) and rinsing the reaction chamber after every use; which is not possible with soluble catalase (**Figure 8B**). These results demonstrate that the catalase remains active in the protein film and can effectively convert the chemical energy into an electrical output.

Although the bioinorganic generator functionalized with the entrapped CAT generates 3 times less energy than the previously reported system using the soluble catalase with 0.2 mL reaction volume, this effect is ameliorated when the reaction volume in the chamber increases (**Figure 8C**). Similar electric power output responses are reached when working with 1 mL (5 nJ x cm⁻²), while the immobilized enzyme using 1.5 mL reaction volume was able to produce 2 times more energy than the soluble enzyme working under the same conditions. This effect suggests that the immobilized CAT is consuming all fuel and therefore generating all the bubbles (mechanical energy) at the interface with the piezoelectric surface, maximizing the energy harvesting. This fact explains that the more fuel (the larger reaction volume), the higher electrical output. On the contrary when the catalase is freely diffusing through the reaction volume, part of the mechanical energy is not harvested because the vast majority of the bubbles are produced far from the piezoelectric surface. This effect explains the observed plateau for the energy generation at increased reaction volumes using the soluble enzyme. Therefore, future bioinorganic generator designs must contemplate major enzyme-piezoelectric component contact across the entire chamber in order to maximize the harvesting of mechanical energy.

To optimize these new generation of bio-inorganic generators, different CAT concentrations were entrapped into CTPR protein films and casted on the piezoelectric surface (**Figure 9A**). Bioinorganic generators with immobilized catalase generate higher electric power outputs as the

immobilize catalase load increases until reaching saturation conditions at 60 μg of immobilized catalase. Finally, we studied the response of bio-inorganic generators (with 30 μg of immobilized CAT) for different H_2O_2 concentrations. . Figure 9B shows that the larger H_2O_2 concentration, the larger the energy output. The maximum electrical output was found at 750 mM, meaning that performance of the system is optimal under that conditions generating $76 \text{ nJ} \times \text{cm}^{-2}$ as maximum energy.

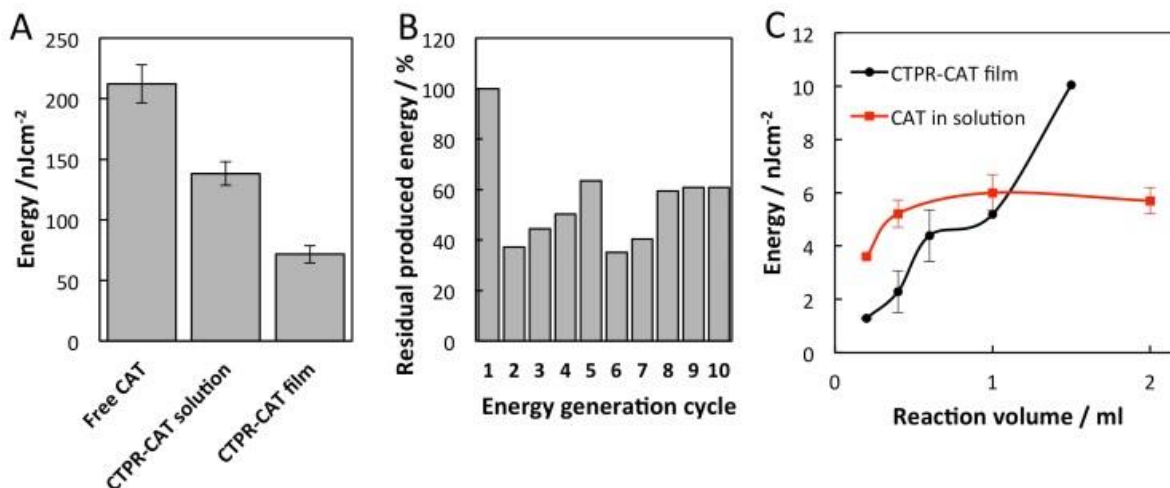


Figure 8. A) Electric energy output of bioinorganic generators with soluble and immobilized enzyme. In all cases 30 μg of soluble or immobilized catalase on SiO_2 coated piezoelectric surface. 710 μg of CTPR protein were used when immobilized catalase. Reaction mixture consists in 0.4 mL chamber volume at 750 mM H_2O_2 in 50 mM sodium phosphate at pH 7. B) Reusability of bioinorganic generators with immobilized enzyme. 710 μg of CTPR protein were used to immobilized catalase. Reaction mixture consists in 0.4 mL chamber volume at 50 mM H_2O_2 in 50 mM sodium phosphate at pH 7.0, for SiO_2 . C) Effect of reaction volume in the produced electric energy of bioinorganic generators with soluble and immobilized enzyme. In all cases 30 μg of soluble or immobilized catalase on SiO_2 coated piezoelectric surface. 710 μg of CTPR protein were used when immobilized catalase. Reaction mixture consists in 750 mM or 50 mM H_2O_2 in 50 mM sodium phosphate at pH 7.0 when immobilized or soluble enzymes were used, respectively.

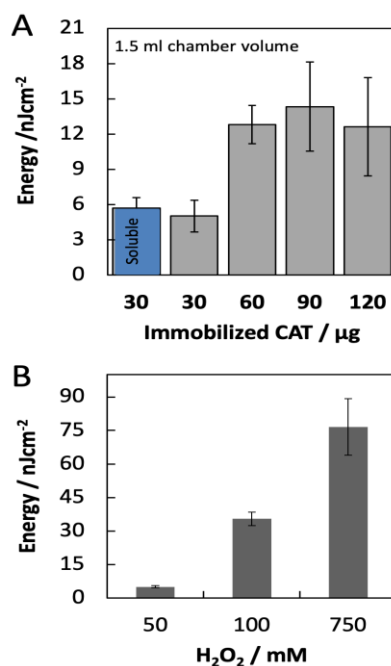


Figure 9. A) Effect of different immobilized enzyme loads in the produced electric energy of bioinorganic generators with immobilized enzyme. In all cases SiO_2 coated piezoelectric surface was employed. 710 μg of CTPR protein were used when immobilized catalase. Reaction mixture consists in 1.5 mL of 50 mM H_2O_2 in 50 mM sodium phosphate at pH 7. B) Effect of hydrogen peroxide concentration in the produced electric energy by bioinorganic generators with immobilized enzyme. In all cases SiO_2 coated piezoelectric surface was employed. 710 μg of CTPR protein were used when immobilized catalase (30 μg). Reaction mixture consists in 1.5 mL of hydrogen peroxide at de indicated concentration in 50 mM sodium phosphate at pH 7.

4.5. Conclusions

In summary, we report a simple methodology for the immobilization of enzymes in solid protein-based biomaterials that can be casted into devices like bio-inorganic generations for the electricity production. The developed methodology has been proven with CAT as model enzyme. Herein, we describe a simple protocol that involves only mixing and drop casting of the target enzyme with a scaffolding protein followed by a mild crosslinking to yield a robust and functional biomaterial. The biomaterial shows the same intrinsic properties of protein films generated only with the scaffolding protein^[105]. Upon the complete fabrication process, the entrapped CAT maintains its functionality and displayed macroscopic order within the biomaterial. In fact, this functional biomaterial was active and successfully integrated into bio-inorganic generators that convert chemical energy into electricity. The device, as previously described using CAT in solution^[357], is based on the conversion of the chemical energy of the CAT reaction into mechanical energy associated to the production of oxygen bubbles and the downstream harvesting of this

mechanical energy by a piezoelectric material to produce an electrical output as open circuit voltage. Here, we demonstrate the effective functionalization of the piezoelectric surface with biocatalytic material, advancing in the fabrication of bio-inorganic generators based on a novel concept that chemical energy transforms into electricity through mechanical energy harvesting. This biomaterial allows the reusability of the device otherwise impossible using the soluble enzyme, although the energy harvesting was not as efficient as the previously reported system with CAT in solution. In addition, the CAT load entrapped into the protein film is a crucial parameter to tune the electric power output of the bioinorganic generators herein developed. Remarkably, we found that the electric power output of bio-inorganic generators with immobilized CAT was maximized by increasing the reaction volume without reaching a saturation point, unlike the system using the soluble CAT that became saturated with sub-milliliters reaction volumes. We envision the potential of this technology to advance the fabrication of more robust bio-inorganic generators where the bioactive phase is in close contact with the piezoelectric transducer. Furthermore, the application of the described biocatalytic protein-based biomaterials can be expanded to the heterogeneous biocatalysis field to improve chemical manufacturing as well to the biosensing field to develop more sensitive devices.

General conclusions

Overall this PhD thesis has mainly focused on the design of protein-based nanostructures and biomaterials. A first approach tackles the design of supramolecular structures based on proteins. In a second part macroscopic protein-based structured and functional materials are fabricated for applications in optics and energy. The current scenario of the design and develop of complex structures lies in the control of the assembly at different length scales. In Nature exists a vast range of supramolecular structures and materials based on biomolecules that emerge from a precise control of the assembly of simple structural elements. In particular, the most sophisticated materials in Nature come from the self-assembly of proteins, *e.g.* ring-shape structures, ordered materials, nanocages with different geometries, nanostructured materials with outstanding mechanical or photophysical properties. For this reason, inspired by Nature we explored the idea of using proteins as building blocks in order to organize and fabricate new structures and new materials with a specific properties. In this sense, we have employed a type of repeat proteins, consensus tetratricopeptide repeat protein (CTPR), which modular and hierarchical structure allows us to produce designed proteins at will.

The main conclusions of this thesis can be summarized in three points:

1. CTPR proteins can be rationally designed to control their self-assembly for the generation of supramolecular structures. In particular, it is described the introduction of novel interacting interfaces in the CTPR scaffold to encode defined higher order structures, under the premise of inducing the formation of protein nanotubes (PNTs). The structures generated from the two models proposed, electrostatic and aromatic models, were fully characterized by techniques of biochemistry, including electrophoresis, FPLC, CD, and electron microscopy (TEM). The PNT obtained through electrostatic interactions displayed less stability and showed prompt dissociation, which made difficult to purify the dimeric form in sufficient quantities for its characterization. In contrast, the PNT obtained through aromatic interactions was stable enough to be isolated and characterized. The structural characterization by TEM showed the correlation between the conformations observed and the projections predicted based on the PNT model, demonstrating specificity in the protein-protein interaction. Therefore, in this work we showed a methodology for the formation of PNTs based on the repeat proteins which opens the door to future applications such as filtration, encapsulation, confined catalysis, and release of small molecules or drugs.

2. Nanostructured self-standing protein films can be fabricated with CTPR proteins. The potential of engineered proteins to develop protein-based optically active materials using a fabrication strategy that combines a bottom-up (functionalization of unit cells) and a top-down (topologically-guided self-assembly) approaches is explored. In a first step, the unique modularity and designability of the protein scaffold is exploited to introduce an optical functional element, *i.e.* an active laser dye (Rhodamine 6G), in the material. The organization of this dye in ordered film gave rise to the generation of light amplification upon photoexcitation of the film with laser pulses, *i.e.* Amplified Spontaneous Emission (ASE). In addition, nanopatterned protein films can be fabricated using top-down soft nanolithography approaches for a next level of organization. In this sense, the nanopatterned surfaces can be replicated on the protein film by using elastomeric gratings with different periodicities as template. The combination of the bottom-up approach, to introduce functionality in the CTPR protein, with the top-down approach to impose another level of nanostructuring led to the generation of Distributed Feedback (DFB) laser effect. Both, ASE and DFB, are phenomena highly desired for applications in optics such as sensing or telecommunications. Therefore, this work depicts an important step toward the fabrication and use of bioinspired multifunctional devices.

3. Functional protein-based materials can be fabricated using scaffolding proteins. A simple methodology for immobilization of enzymes in solid protein-based materials was developed, the materials were finally integrated into devices for the production of energy. The methodology developed has been demonstrated using catalase (CAT) as model enzyme. Herein, a simple protocol that involves only mixing and drop casting of the target enzyme with a scaffolding protein followed by a mild crosslinking, yielded a robust and functional material. The entrapped CAT maintained its structural properties and functionality and displayed macroscopic order within the material. In fact, this functional material was active and successfully integrated into bio-inorganic generators that converted chemical energy into electricity. The device is based on the conversion of the chemical energy of the CAT reaction into mechanical energy associated to the production of oxygen bubbles and the downstream harvesting of this mechanical energy by a piezoelectric material to produce an electrical output. These biocatalytic films allow the reusability of the device otherwise impossible using the soluble enzyme, although the

energy harvesting was not as efficient as the previously reported system with CAT in solution. However, the CAT load entrapped into the protein film is a crucial parameter to tune the electric power output of the bioinorganic generators herein developed. Remarkably, the electric power output of bio-inorganic generators with immobilized CAT was maximized by increasing the reaction volume without reaching a saturation point, unlike the system using the soluble CAT that became saturated with sub-milliliters reaction volumes. The potential of this technology is expected to advance the fabrication of more robust bio-inorganic generators where the bioactive phase is in close contact with the piezoelectric transducer. Furthermore, the application of the described biocatalytic protein-based materials can be expanded to the heterogeneous biocatalysis field to improve chemical manufacturing as well to the biosensing field to develop more sensitive devices.

In summary, in this thesis have been explored three different systems based on CTPR proteins. On the one hand, PNTs were designed through the self-assembly of CTPR proteins by introducing novel protein-protein interfaces with protein design approaches. On the other hand, given the intrinsic capabilities of CTPR proteins to form ordered self-standing films, a step forward was made to apply them for the fabrication of functional materials and their integration into optically active or energy-production devices.

Appendixes

Appendix 1

Self-assembly of repeat proteins: Concepts and design of new interfaces

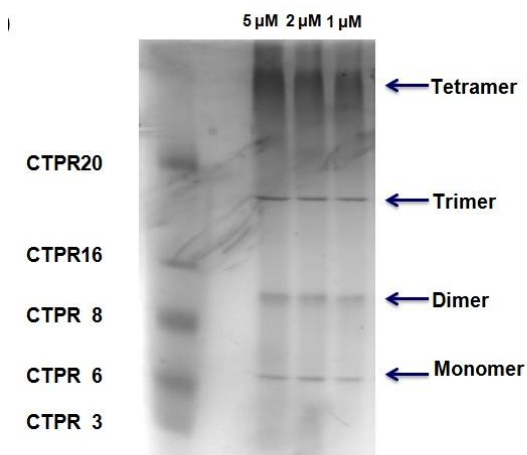


Figure 1. Native gel of the C6L_{dimer} at different protein concentrations. From left to right C6L dimeric fraction loaded at 5 μ M, 2 μ M and 1 μ M protein concentration. In the gel, bands that correspond to the size of C6L monomers, dimers, trimers, and tetramers are observed. In the first line, a mixture of monomeric wild type CTPR proteins with different number of repeats (CTPR3, CTPR6, CTPR8, CTPR16, and CTPR20) are shown as a molecular weight marker.

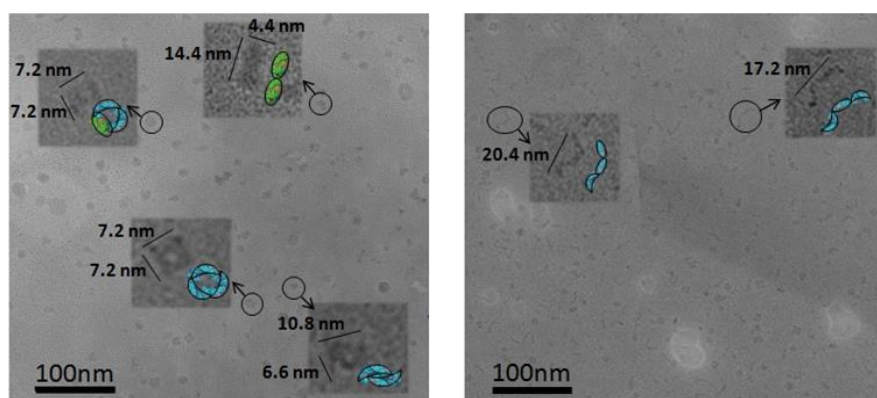


Figure 2. TEM images of the C6L_{dimer} sample. C6L_{dimer} in 10 mM NaCl, 10 mM Tris pH=7.5 buffer are deposited and negative stained using uranyl acetate. The TEM micrographs show that the C6L_{dimer} dimer sample is not homogeneous, since different oligomeric states including dimers, trimers, and tetramers are observed. Zoom in images show the different structures that appear in the TEM image of the C6L_{dimer} sample, highlighted with black circles. In the zoom-in images are represented the structures of the possible conformations that are observed in the TEM image based on potential

arrangements of C6L monomers. The representations are shown as surface and display potential monomer colored in blue and potential dimers colored in green.

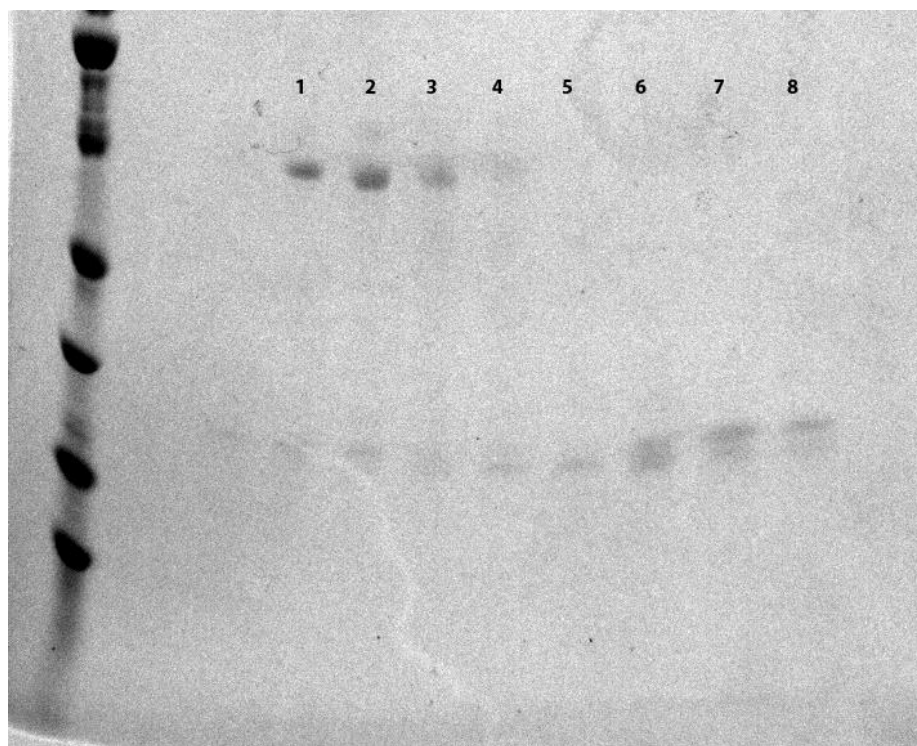


Figure 3. SDS-PAGE gel analysis of the FPLC fractions obtained for C6L (Figure 2B of the manuscript). Lanes 1, 2, 3 correspond to elution volumes from 8 to 9.5 ml (dimeric fraction) and lanes 5, 6, 7 and 8 correspond to elution volumes from 10 to 12 ml (monomeric fraction). MW markers from the bottom to the top correspond to 18.4, 25.0, 35.0, 45.0, 66.2 and 116.0 kDa.

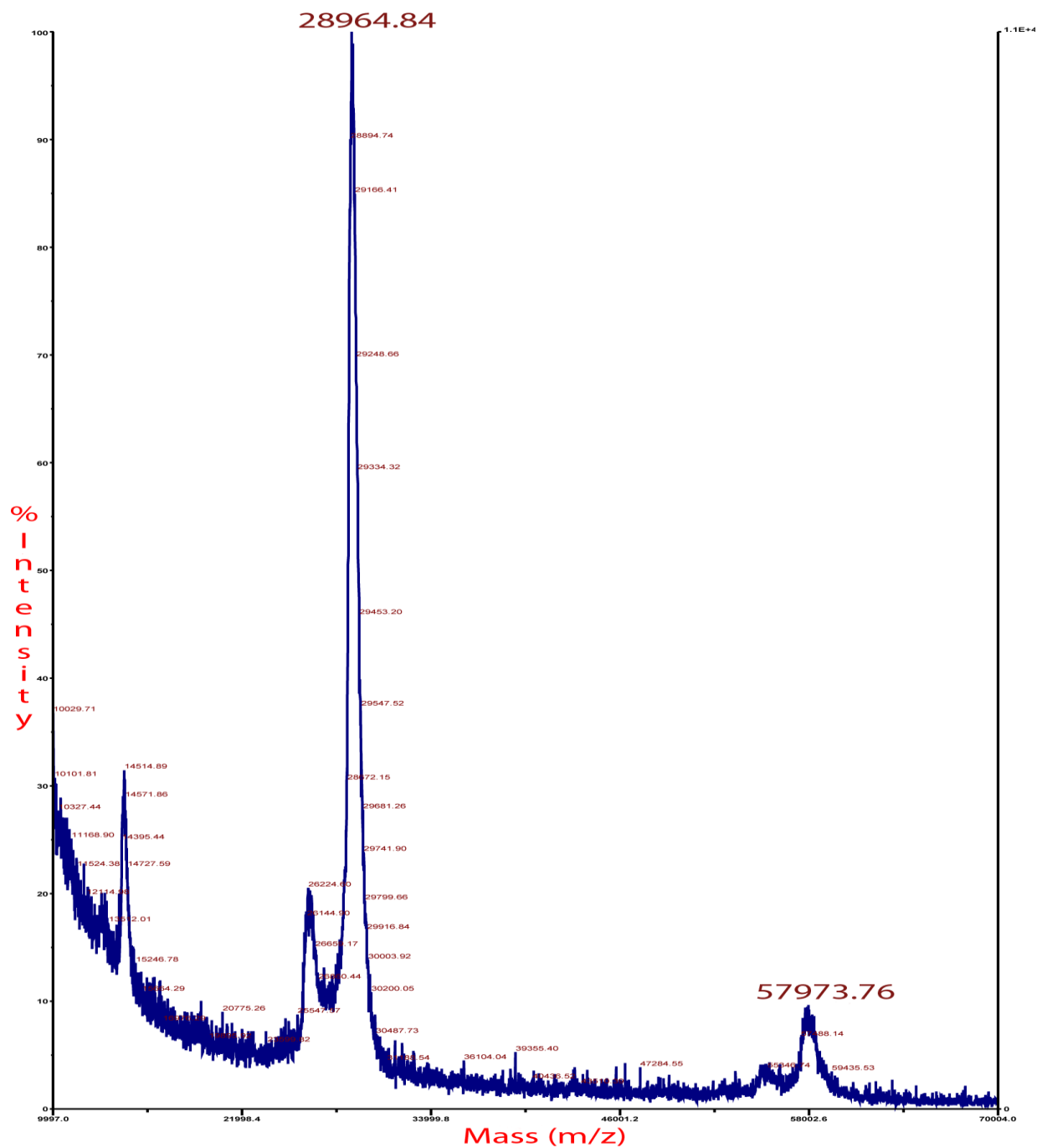


Figure 4. Mass spectrometry spectrum of FPLC purified C6L dimer. The spectrum shows a main the peak that corresponds to the C6L monomer (28164 kDa) and another that corresponds to double the size (57973 kDa).

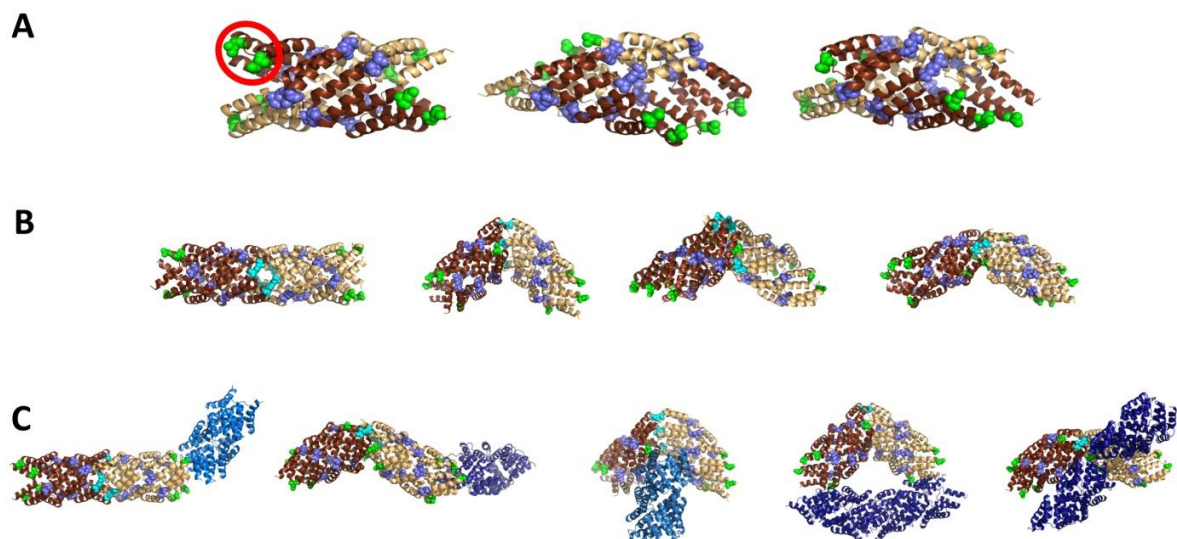


Figure 5. Different potential conformations that could be obtained from the designed C6L model using Cluspro program. **A.** 3 different possible stable dimers. The designed leucines from the novel interface that are interacting are highlighted as blue spheres and the leucines from the novel interface that are solvent exposed are highlighted in green. The two proteins forming the dimer are colored in dark and light brown to distinguish one from the other, but they are identical. **B.** 4 different stable tetramers that could be formed by the interaction of the dimers shown in A. The interacting leucines are highlighted in light blue light and the leucines that are solvent exposed highlighted in green. **C.** Different examples of stable conformations that could be formed by the interaction of the tetramers shown in B, colored in brown and stable dimers and tetramers obtained from A and B, colored in blue.

[Protein] 0.5 μ M 0.7 μ M 1 μ M 2 μ M 3 μ M 4 μ M 5 μ M

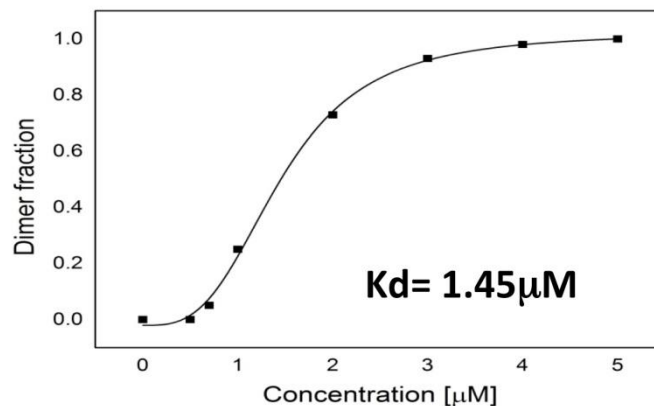
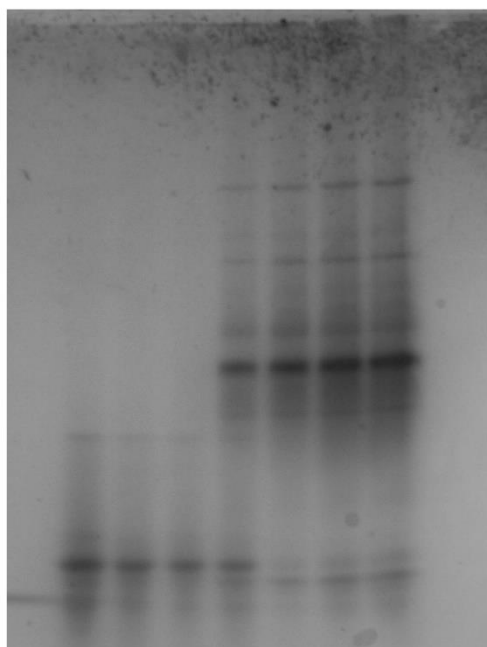


Figure 6. C6L_2 higher order species dissociation studies. Purified C6L_2_{dimer} was run on a native gel at different concentrations from 5 to 0.5 μ M. The gel shows the dissociation of the purified dimeric and higher order species form into monomer. Right panel shows the fit of the bands corresponding to the dimer/monomer fractions quantified from the gel to a two state dissociation.

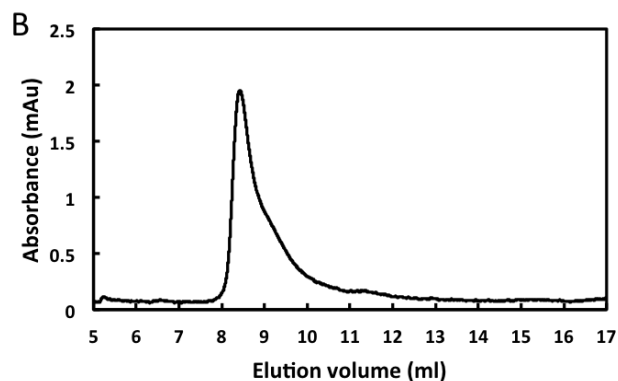
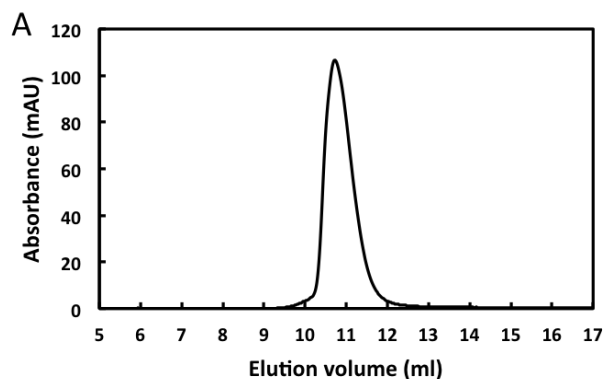


Figure 7. Size exclusion chromatography of monomeric and dimeric forms of CTPR6. **A.** Size exclusion chromatogram over a Superdex S75 column of monomeric wild type CTPR6. The monomeric protein elutes at 10.6 ml. **B.** Size exclusion chromatogram over a Superdex S75 column of a purified CTPR6 dimer of C6Y model. The dimeric protein elutes at 8.4 ml.

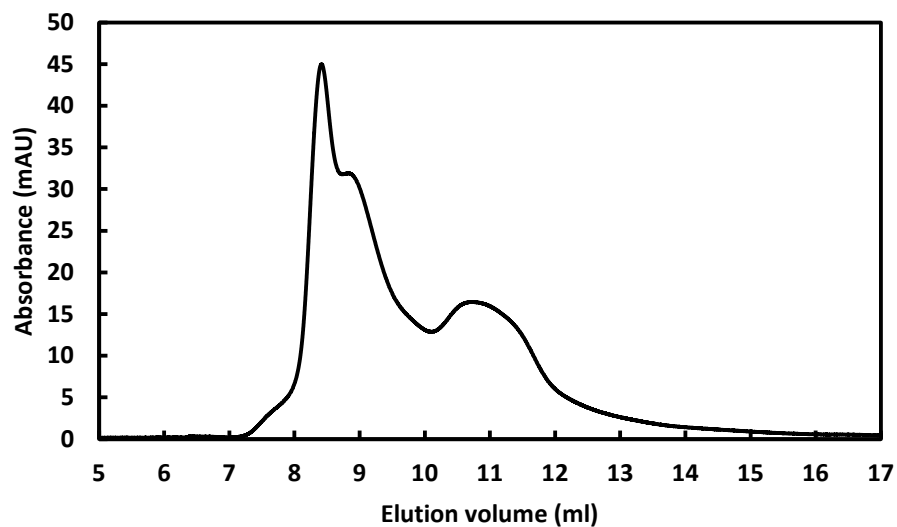


Figure 8. Size exclusion chromatography of purified C6HD dimer. Size exclusion chromatogram over a Superdex S75 column of purified C6HD dimer. The chromatogram shows two peaks corresponding to the dimeric and monomeric forms of C6HD at elution volume of 8.5 ml and 11 ml, respectively. This result shows that upon dilution the dimeric sample reequilibrates into monomeric and dimeric forms.

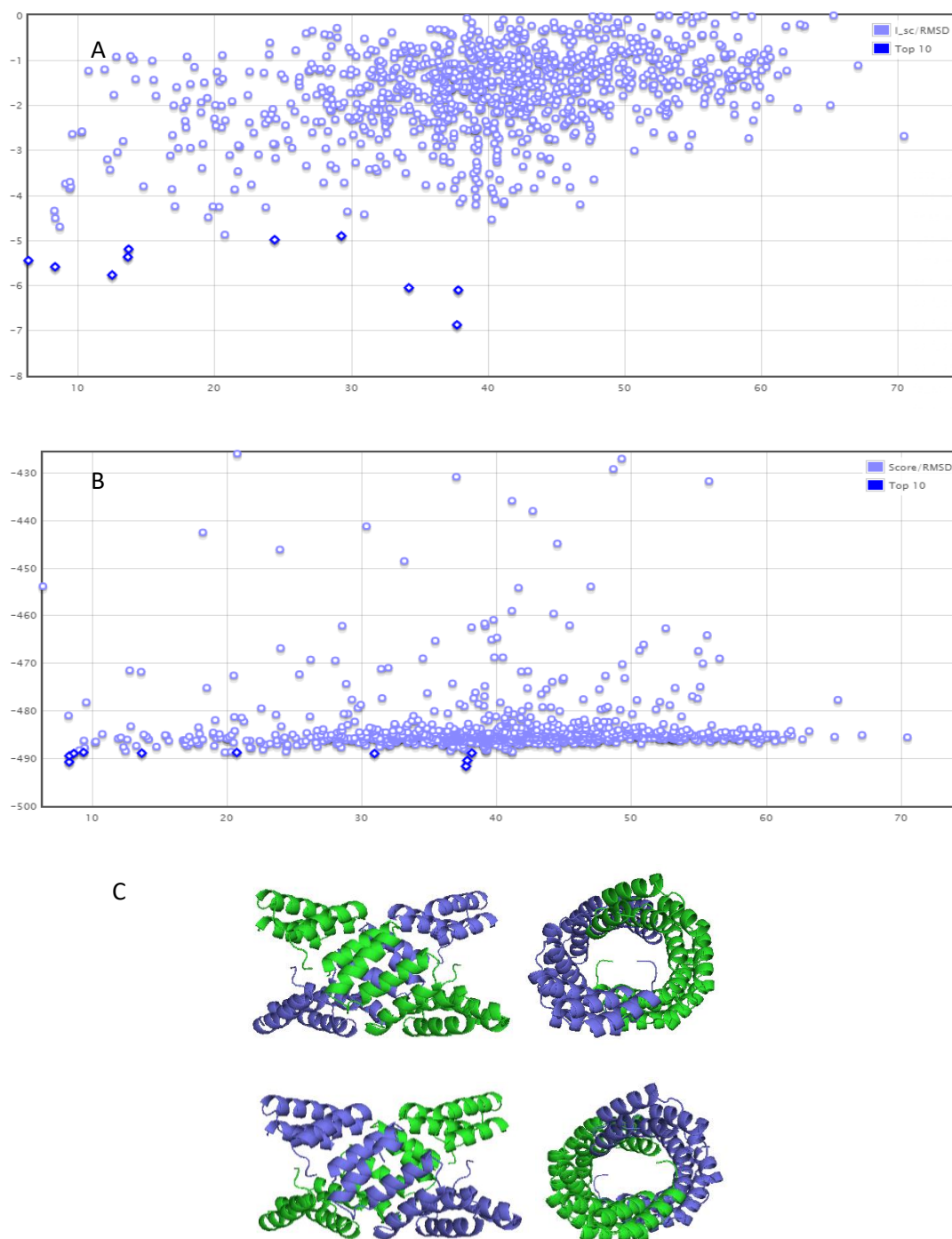


Figure 9. RosettaDock results for the design of nanotubes based on aromatic interactions. Computational analysis of the interface between both chains in the tyrosine model (C6Y) using *RosettaDock* online server. The plot show the energy maps of the Rosetta simulation. **A.** Plot of the interface score plotted against the RMSD (root-mean-square deviation). The interface scores are total score of the complex minus the total score of each chain in isolation. **B.** Plot of the total score

plotted against the RMSD. Highlighted in darker blue are the models that displayed lower energies. **C.** PDB structures from the docking using Rosetta online server. Two representative nanotubular complexes with a minimum free-energy are displayed in the lateral and axial view. The different colors point out the different protein chains forming the CTPR dimers.

Cluster	Members	Representative	Weighted Score
0	104	Center	-894.4
		Lowest Energy	-1026.5
1	91	Center	-658.7
		Lowest Energy	-1173.3
2	81	Center	-643.6
		Lowest Energy	-1003.2
3	62	Center	-727.3
		Lowest Energy	-1018.8
4	60	Center	-963.1
		Lowest Energy	-963.1
5	49	Center	-651.2
		Lowest Energy	-700.6
6	41	Center	-698.6
		Lowest Energy	-832.5
7	35	Center	-637.1
		Lowest Energy	-637.1
8	34	Center	-603.1
		Lowest Energy	-806.0
9	29	Center	-594.4
		Lowest Energy	-664.0
10	25	Center	-626.2
		Lowest Energy	-815.6
11	24	Center	-616.2
		Lowest Energy	-666.0
12	23	Center	-592.8
		Lowest Energy	-856.9

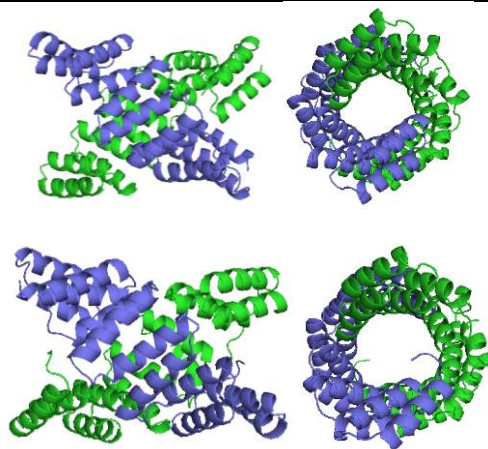


Figure 10. Computational analysis of the design of nanotubes based on aromatic interactions using *ClusPro* server. The table show the results ordered in function of cluster size. Two energy scores are displayed for each cluster, the center is energy in the cluster center (the structure that has the highest number of neighbor structures in the cluster) and the energy of the lowest-energy structure in the cluster. On the bottom, two representative complexes form the docking results with a minimum free-energy are displayed in lateral and axial view. The different colors point out different protein chains.

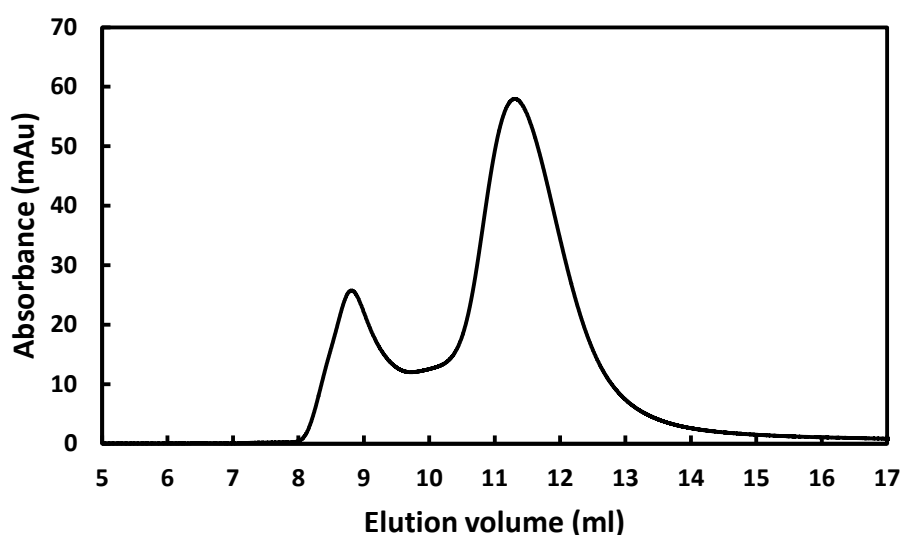


Figure 11. Size exclusion chromatography of C6Y dimer purified over a Superdex 75 column. The chromatogram display two peaks corresponding to the dimeric and monomeric forms of C6Y at elution volume of 8.5ml and 11.5 ml, respectively.

Appendix 2

**Engineered protein-based functional
nanopatterned materials for bio-optical
devices**

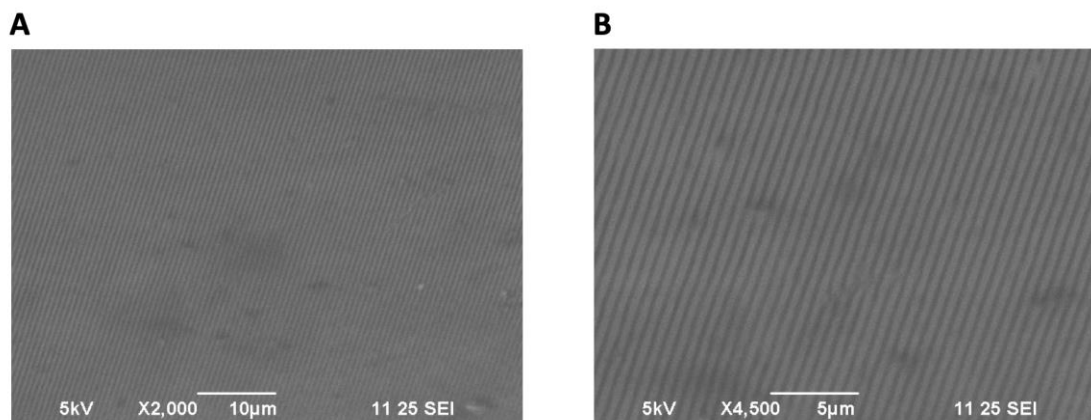


Figure 1. SEM images of CTPR nanostructured film 6 months after manufacturing, stored at room temperature and ambient humidity at two different magnifications.

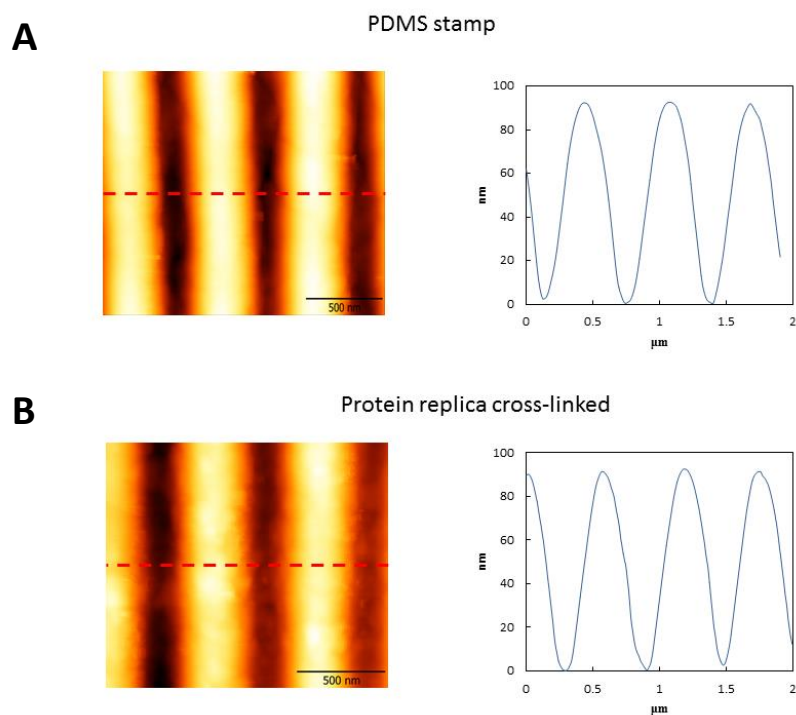


Figure 2. AFM image of PDMS stamp (A) and CTPR nanostructured film replica upon cross-linking reaction and water immersion (B) showing $2 \mu\text{m}^2 \times 2 \mu\text{m}^2$ area and z-axis profile.

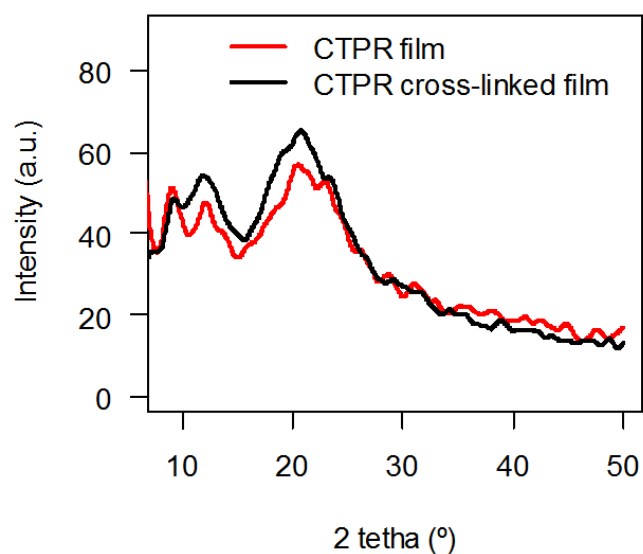


Figure 3. X-ray diffraction spectra of CTPR nanostructured film and CTPR nanostructured cross-linked film under moisture conditions.

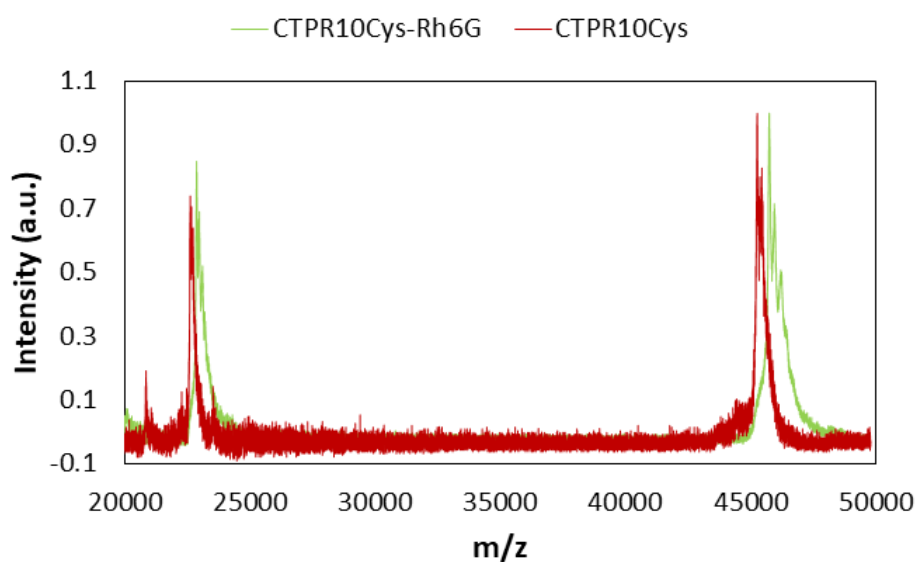


Figure 4. Mass spectra of CTPR 10Cys and CTPR 10Cys functionalized with Rh6G. The molecular weight of CTPR 10Cys protein resulted in 45257.6 Da (in red), whereas the protein conjugated 45737.5 Da (in green). The difference of 479.94 between both peaks correspond to the molecular weight of the Rh6G ($MW_{\text{theoretical}}$: 481.50 Da).

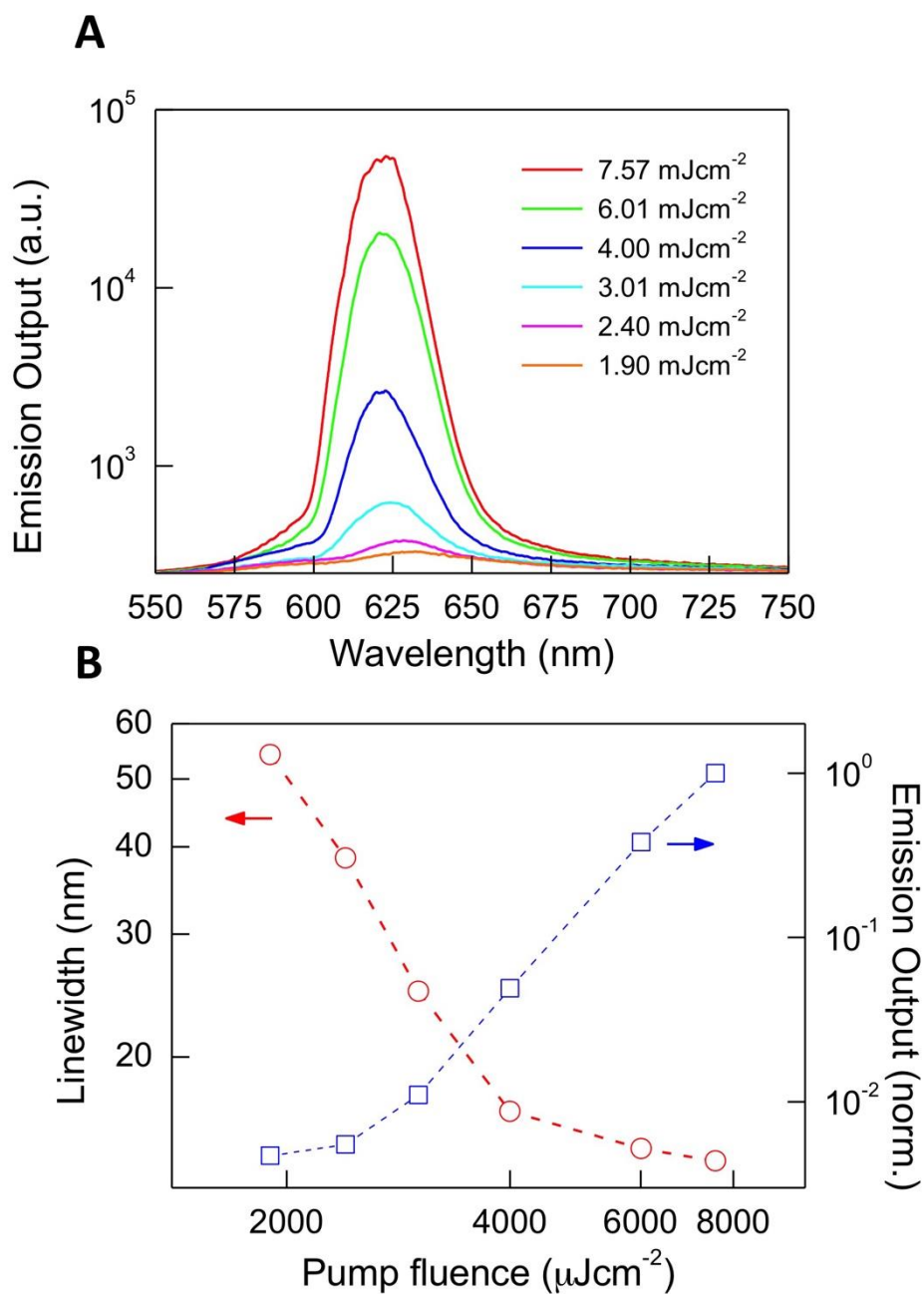


Figure 5. (A) A log-lin plot of the PL spectra upon different pump fluences. (B) Log-log plots of emission linewidth (circles, left Y-axis) and emission output normalized by the output at the highest fluence (squares, right Y-axis) versus pump fluence, (red and blue arrows indicate respectively their corresponding Y-axis).

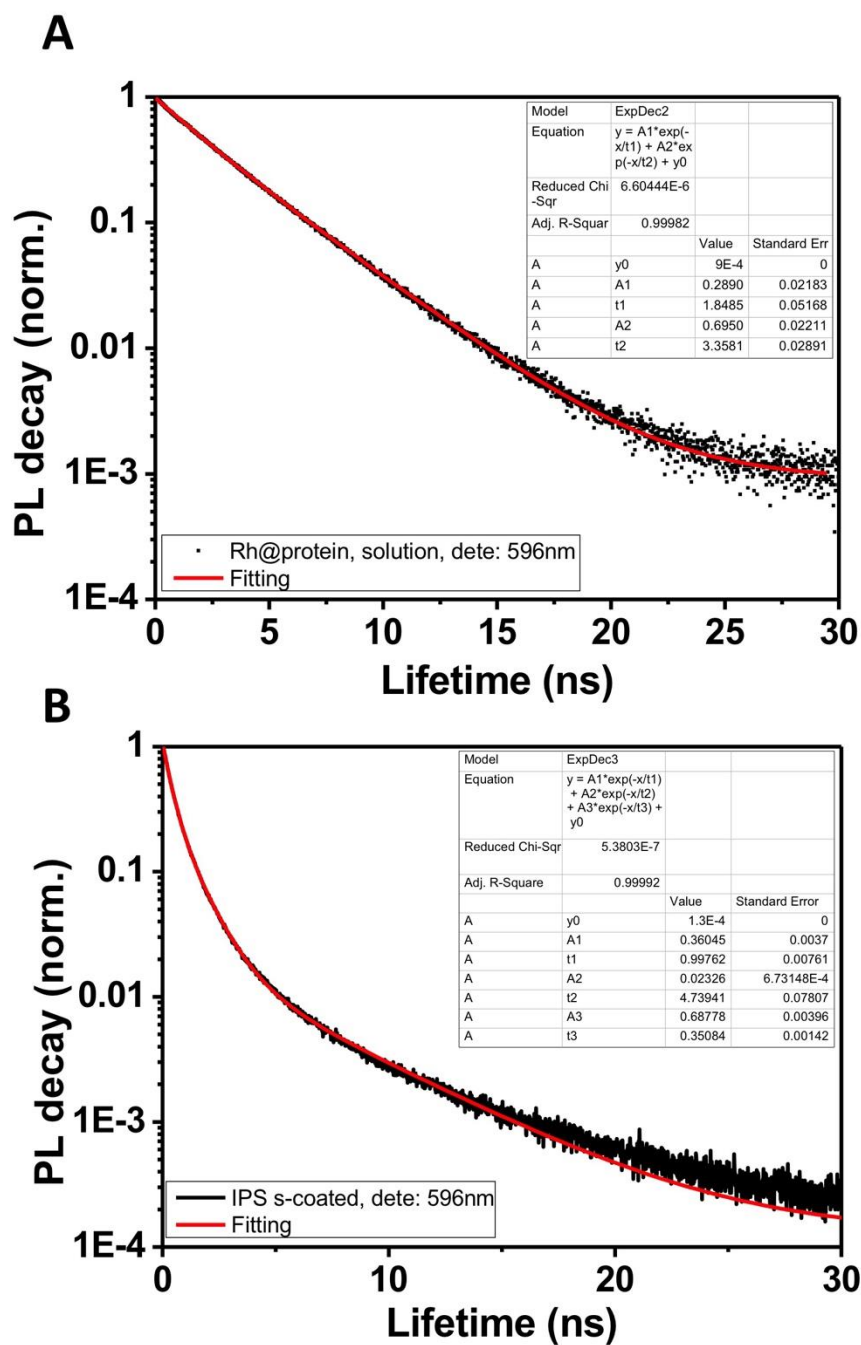


Figure 6. Time resolved PL decay curves on CTPR-RH6G in solution (A) and film (B). PL decays of solutions (films) were fitted according to a two- (three-) exponential law. Lifetimes were obtained as an intensity average of the components taking into account their respective statistical weight.

Table 1. Time resolved PL constants of CTPR-RH6G in solution and film.

Sample	χ^2	A_1	τ_1 (ns)	A_2	τ_2 (ns)	A_3	τ_3 (ns)	τ_{av} (ns)	ϕ (%)	k_r (s ⁻¹)	k_{nr} (s ⁻¹)
Film	0.999	0.360	0.997	0.687	0.350	0.023	4.739	1.353	17	$1.2 \cdot 10^8$	$6.2 \cdot 10^8$
Solution	0.999	0.289	1.848	0.695	3.358	-	-	3.07	24.5	$0.8 \cdot 10^8$	$2.5 \cdot 10^8$

Where τ_{av} is the intensity-weighted average PL lifetime obtained from the individual lifetime components (τ_i) and their statistical weights in the fits (A_i) as:

$$\tau_{av} = \frac{\sum_i \tau_i A_i^2}{\sum_i A_i}$$

whereas ϕ stands for the PL quantum efficiency and k_r and k_{nr} are the radiative and non radiative decay rates respectively determined as:

$$k_r = \frac{\phi}{\tau_{av}} \quad k_{nr} = \frac{1 - \phi}{\tau_{av}}$$

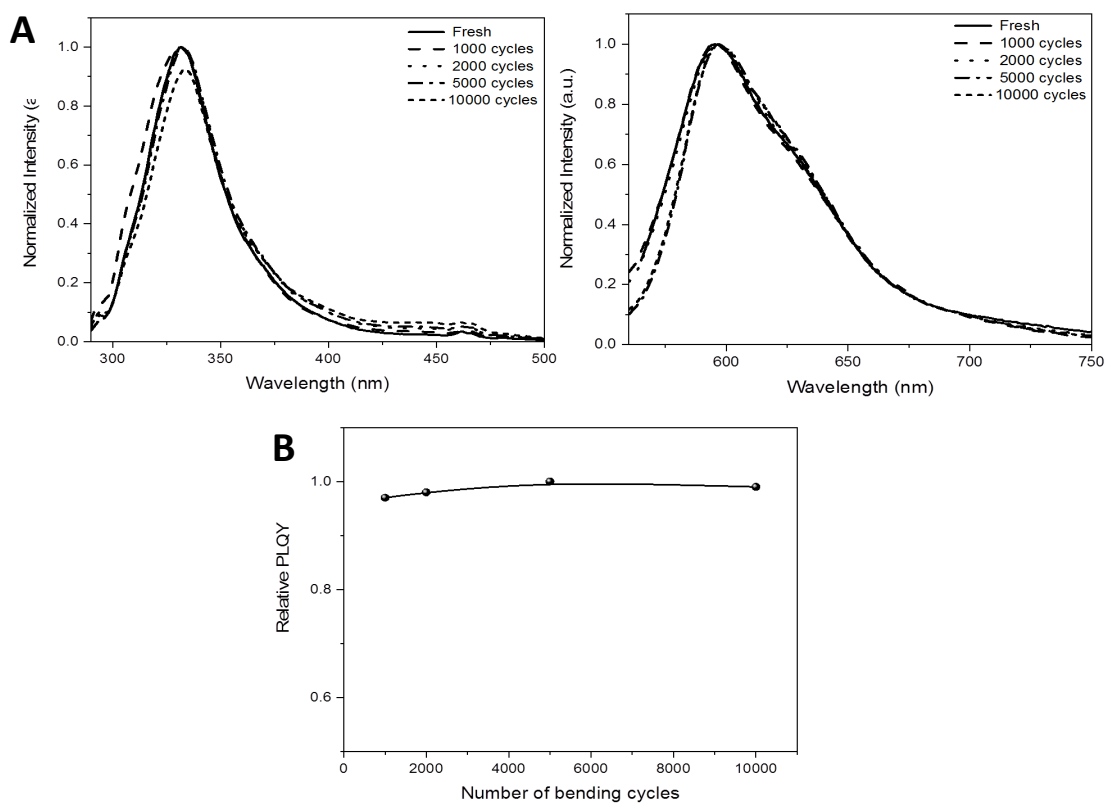


Figure 7. (A) Emission spectra of the CTPR-Rh films focusing on the emission of the CTPR ($I_{\text{exc}}=275$ nm; left) and the Rh ($I_{\text{exc}}=550$ nm; right) after each bending cycle (see legend). (B) Changes of the photoluminescence quantum yield (PLQY) after each bending cycle.

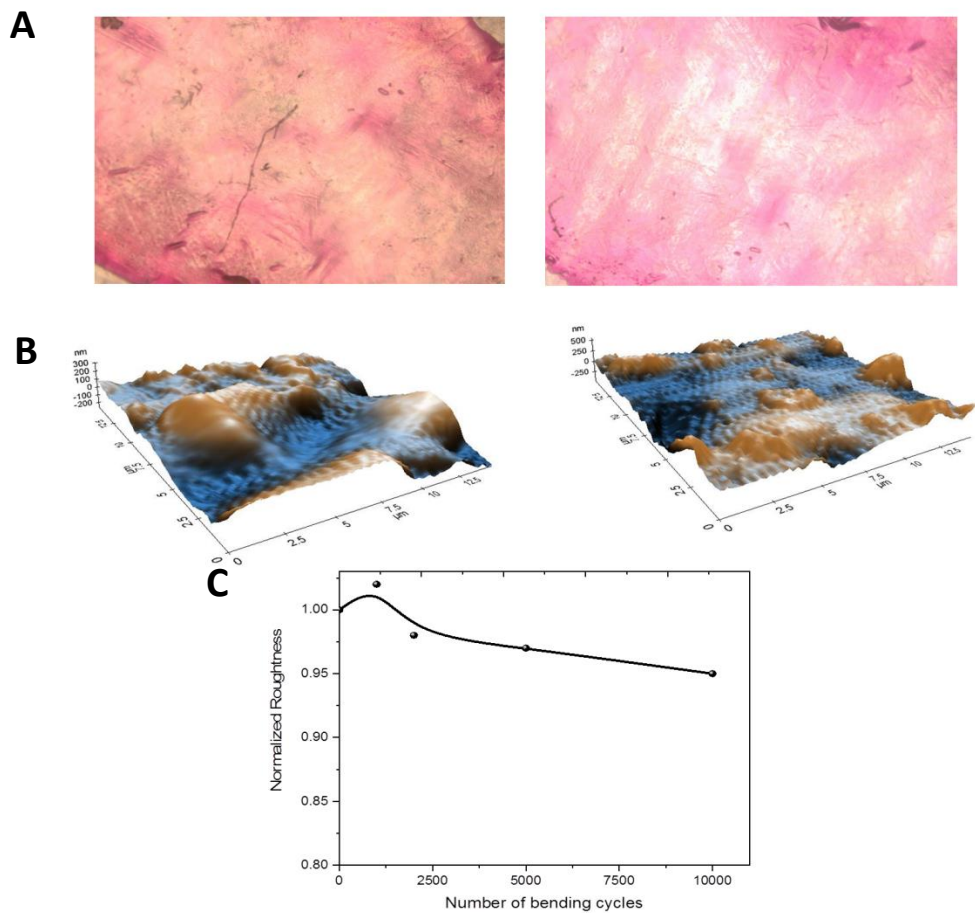


Figure 8. (A) Optical image of fresh (left) and after 10,000 bending cycles (right) of CTPR-Rh films. (B) AFM image of fresh (left) and after 10,000 bending cycles (right) of CTPR-Rh films. (C) Roughness changes versus number of bending cycles.

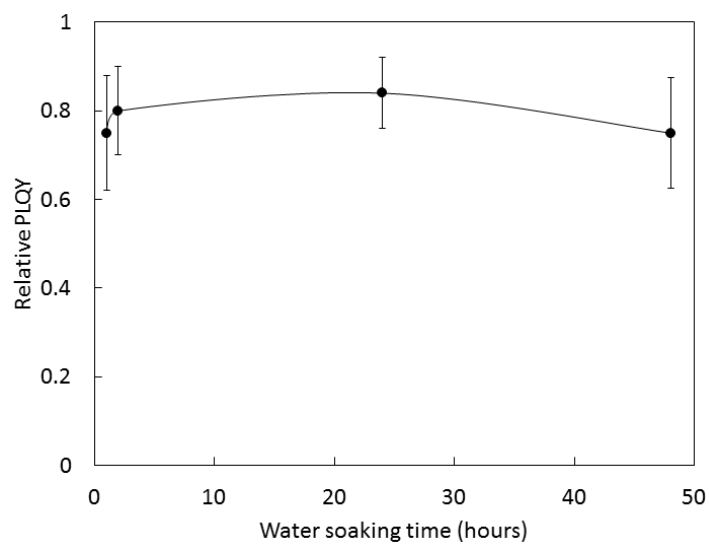


Figure 9. Photoluminescence quantum yield (PLQY) of CTPR-Rh6G nanopatterned cross-linked film upon several hours under moisture conditions.

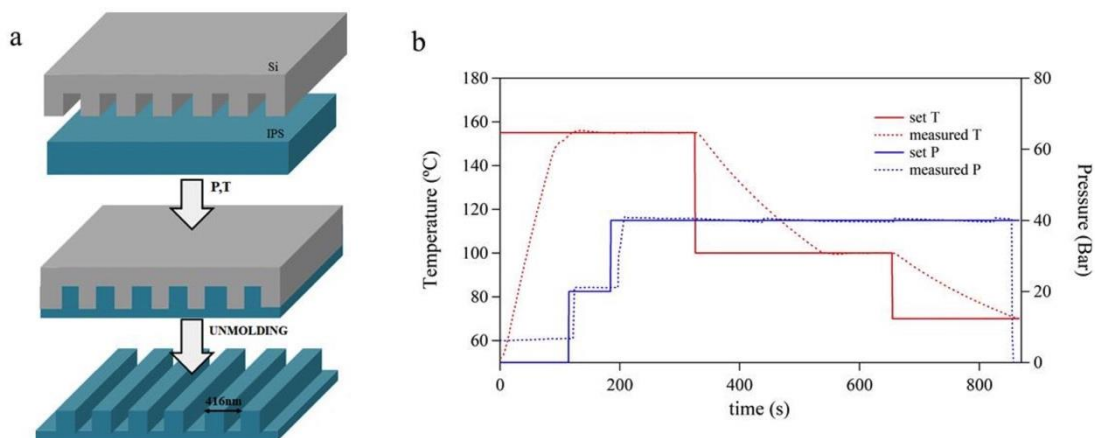


Figure 10. (a) Outline of the replication of a polymer grating from Si to IPS. (b) Temperature and pressure profiles during the nanoimprinting process.

Appendix 3

**Biocatalytic protein-based materials for
integration into energy devices**

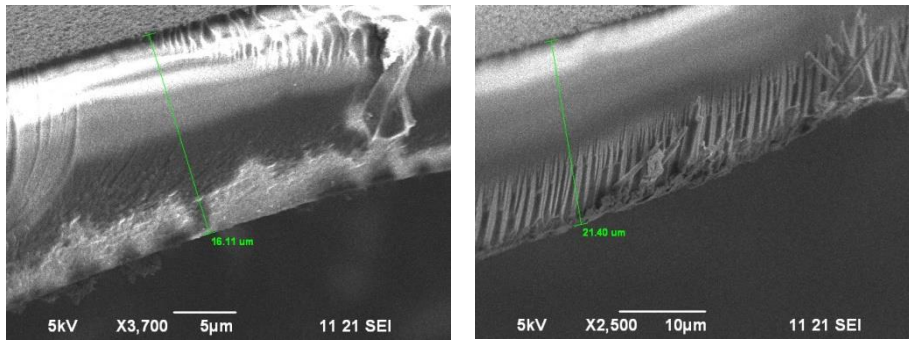


Figure 1. Scanning electron microscopy (SEM) of the biomaterial. Cross-section of different areas showing the film thickness.

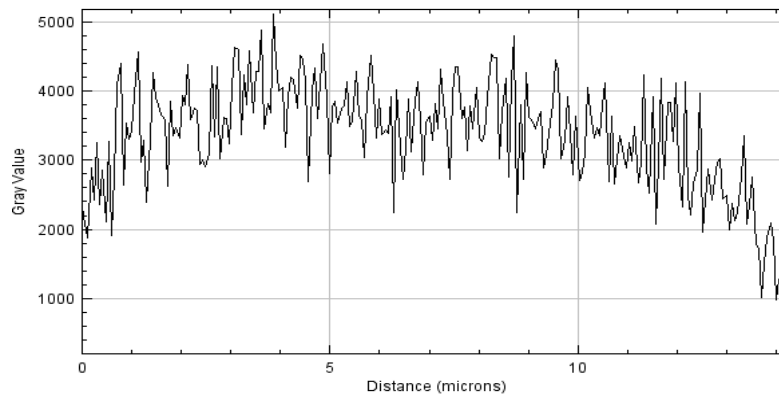


Figure 2. Fluorescence intensity distribution across the confocal fluorescence Z-stack images within a film section monitoring the fluorescence intensity of the Rhodamine B isothiocyanate-labeled CAT.

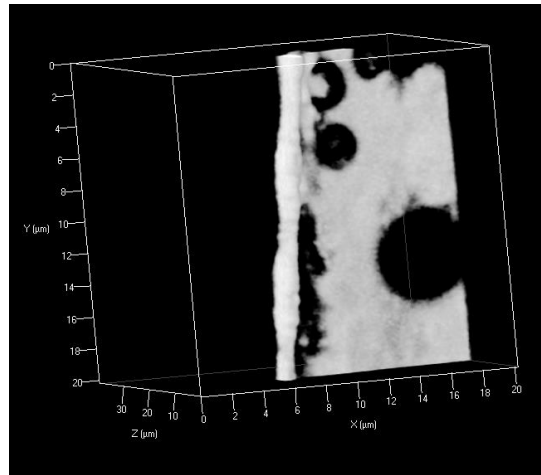


Figure 3. Confocal microscopy 3D reconstruction of the biomaterials from a Z-stack of the fluorescence intensity of the Rhodamine B isothiocyanate-labeled CAT. The image shows the fluorescence intensity at the cross-section of the biomaterial and at the surface.

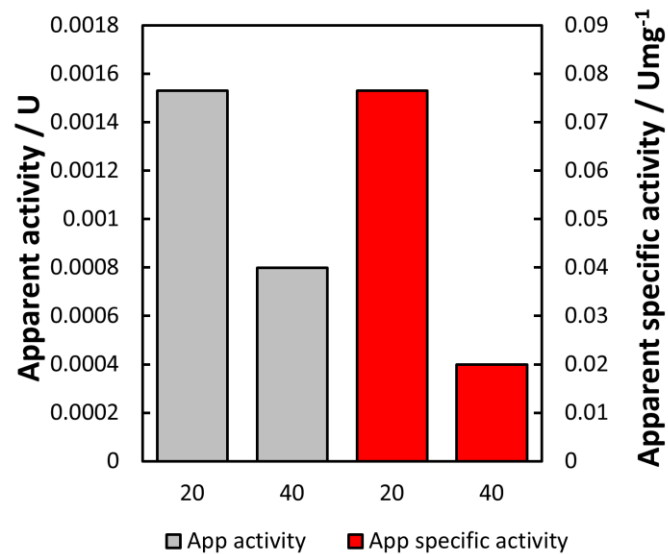


Figure 4. Apparent catalase activity and apparent catalase specific activity of protein films of 20 and 40 μm thickness.

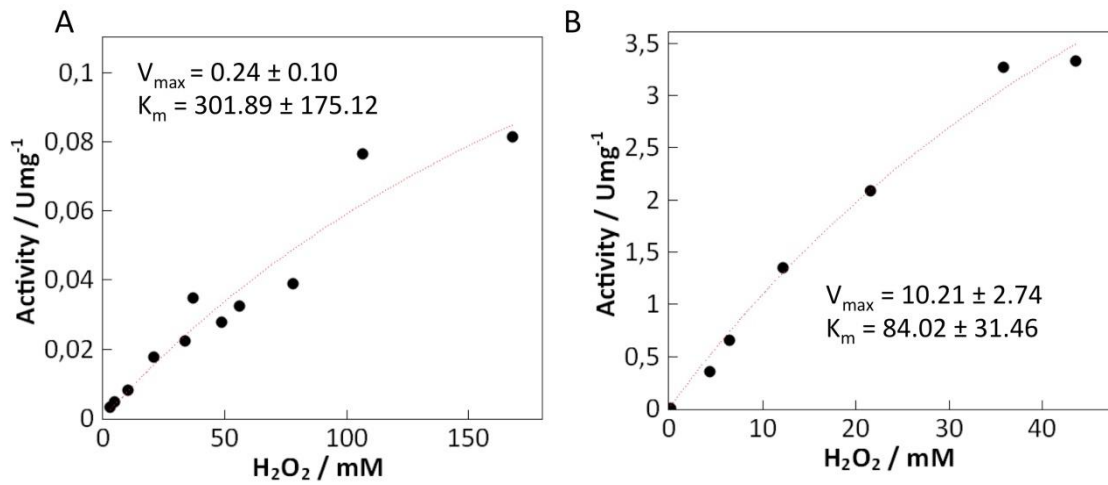


Figure 5. Measurements of activity of CAT at different substrate concentration. A. In the solid protein thin film. B. In solution.

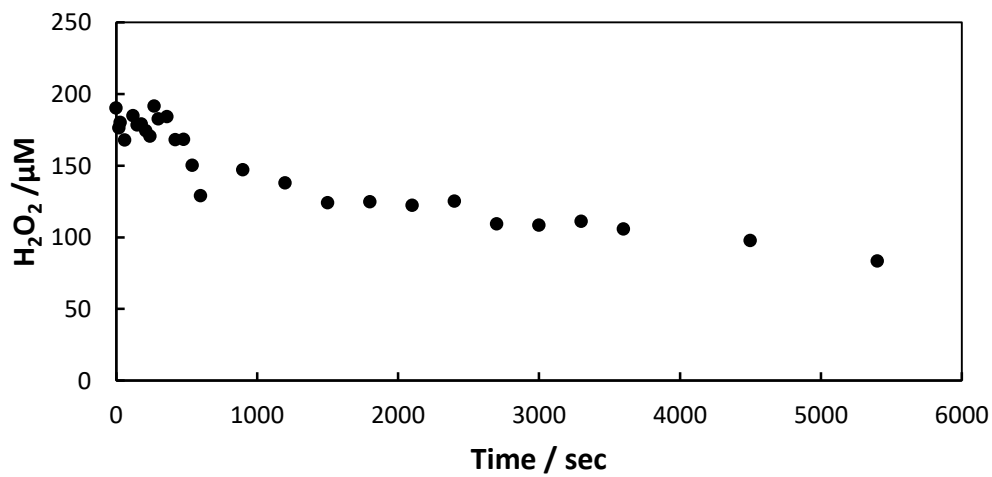


Figure 6. Enzymatic kinetic of H_2O_2 consumption by immobilized CAT. A lag-phase is observed during the first 400 sec of the reaction.

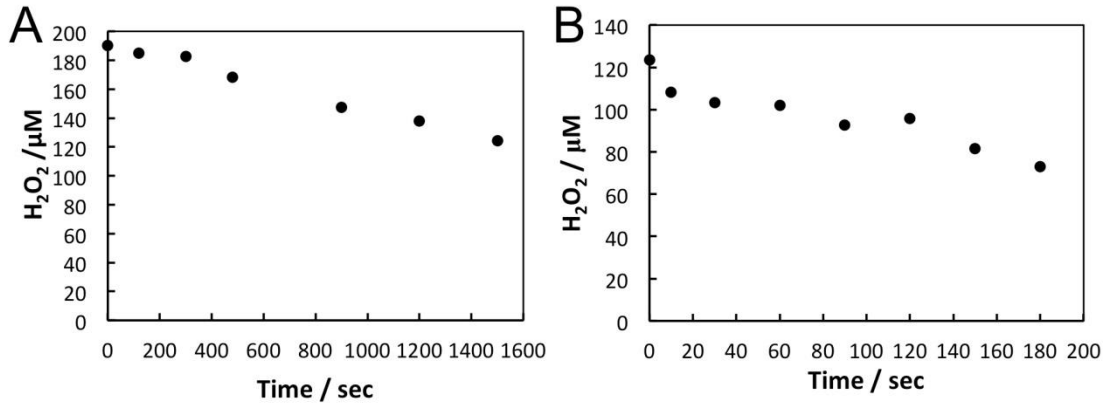


Figure 7. Enzymatic kinetics of CAT in solid thin film (A) and in solution (B).

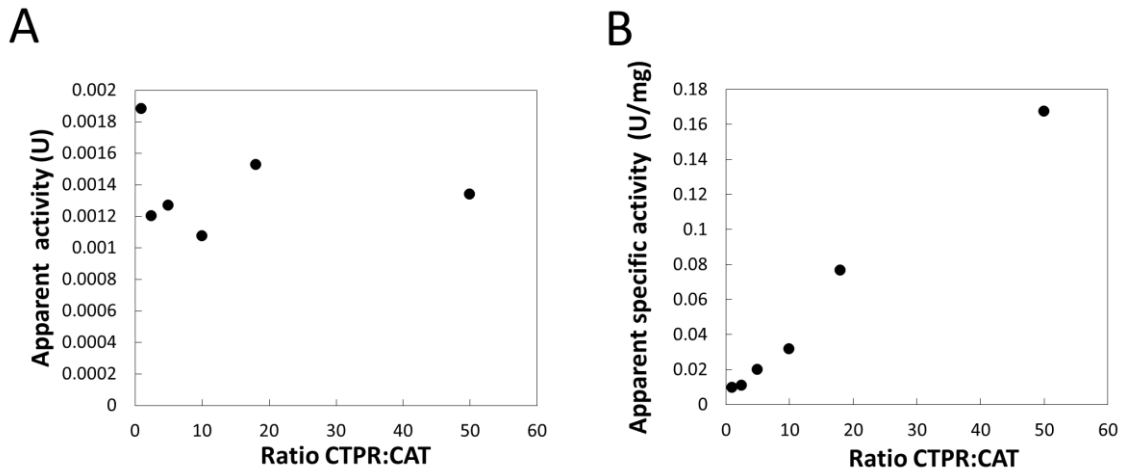


Figure 8. Apparent catalase activity (A) and apparent catalase specific activity (B) of protein films with different CTPR:CAT ratios.

References

- [1] A. Linde, D. Linde, A. Mezhlumian, *Phys. Rev. D* **1994**, *49*, 1783–1826.
- [2] P. Chellan, P. J. Sadler, *Phil. Trans. R. Soc. A* **2015**, *373*, 20140182.
- [3] W. Maret, *IJMS* **2016**, *17*, 66.
- [4] H. C. Betts, **n.d.**, 10.
- [5] P. Rimmer, O. Shorttle, *Life* **2019**, *9*, 12.
- [6] D. Lancet, R. Zidovetzki, O. Markovitch, **n.d.**, 36.
- [7] A. Lazcano, **n.d.**, 5.
- [8] F. Feijó Delgado, N. Cermak, V. C. Hecht, S. Son, Y. Li, S. M. Knudsen, S. Olcum, J. M. Higgins, J. Chen, W. H. Grover, et al., *PLoS ONE* **2013**, *8*, e67590.
- [9] “Introduction to Proteins: Structure, Function, and Motion, Second Edition,” can be found under <https://www.crcpress.com/Introduction-to-Proteins-Structure-Function-and-Motion-Second-Edition/Kessel-Ben-Tal/p/book/9781498747172>, **n.d.**
- [10] **N.d.**
- [11] C. M. Dobson, **2003**, *426*, 7.
- [12] K. A. Dill, S. B. Ozkan, M. S. Shell, T. R. Weikl, **2008**, 32.
- [13] C. B. Anfinsen, *Science* **1973**, *181*, 223–230.
- [14] J. D. Forman-Kay, T. Mittag, *Structure* **2013**, *21*, 1492–1499.
- [15] R. B. Berlow, H. J. Dyson, P. E. Wright, *Journal of Molecular Biology* **2018**, *430*, 2309–2320.
- [16] G. N. Ramachandran, C. Ramakrishnan, V. Sasisekharan, **n.d.**, 5.
- [17] K. Yue, K. A. Dill, *Proceedings of the National Academy of Sciences* **1995**, *92*, 146–150.
- [18] H. Lodish, A. Berk, S. L. Zipursky, P. Matsudaira, D. Baltimore, J. Darnell, *Molecular Cell Biology. 4th edition* **2000**.
- [19] F. Yang, L. G. Moss, G. N. Phillips, **1996**, *14*, 6.
- [20] **N.d.**
- [21] E. MacCarthy, D. Perry, D. B. KC, in *Protein Supersecondary Structures: Methods and Protocols* (Ed.: A.E. Kister), Springer New York, New York, NY, **2019**, pp. 15–45.
- [22] J. M. Gulbis, Z. Kelman, J. Hurwitz, M. O’Donnell, J. Kuriyan, *Cell* **1996**, *87*, 297–306.
- [23] P. Agarwal, *Microb Cell Fact* **2006**, *5*, 2.
- [24] Q. Q. Gao, E. M. McNally, in *Comprehensive Physiology* (Ed.: R. Terjung), John Wiley & Sons, Inc., Hoboken, NJ, USA, **2015**, pp. 1223–1239.
- [25] K. Gelse, *Advanced Drug Delivery Reviews* **2003**, *55*, 1531–1546.
- [26] S. Kato, T. Matsui, C. Gatsogiannis, Y. Tanaka, *Biophys Rev* **2018**, *10*, 191–202.
- [27] A. J. Marengo-Rowe, *Baylor University Medical Center Proceedings* **2006**, *19*, 239–245.
- [28] T. Vora, D. Bisset, S.-H. Chung, *Biophysical Journal* **2008**, *95*, 1600–1611.
- [29] C. N. Morrison, T. Spatzal, D. C. Rees, *J. Am. Chem. Soc.* **2017**, *139*, 10856–10862.
- [30] R. Z. Kramer, J. Bella, P. Mayville, B. Brodsky, H. M. Berman, *nature structural biology* **1999**, *6*, 4.
- [31] B. Hazes, K. H. Kalk, W. G. J. Hol, K. A. Magnus, C. Bonaventura, J. Bonaventura, Z. Dauter, *Protein Science* **2008**, *2*, 597–619.
- [32] V. I. Timofeev, R. N. Chuprov-Netochin, V. R. Samigina, V. V. Bezuglov, K. A. Miroshnikov, I. P. Kuranova, *Acta Crystallogr F Struct Biol Cryst Commun* **2010**, *66*, 259–263.
- [33] L. D. Barron, *Chem. Soc. Rev.* **1986**, *15*, 189.
- [34] J. Gal, *Nature Chem* **2017**, *9*, 604–605.
- [35] D. G. Blackmond, *Cold Spring Harb Perspect Biol* **2019**, *11*, a032540.
- [36] L. D. Barron, *Space Sci Rev* **2008**, *135*, 187–201.
- [37] C. Grande, N. H. Patel, *Nature* **2009**, *457*, 1007–1011.
- [38] L. K. Jesson, S. C. H. Barrett, *Nature* **2002**, *417*, 707–707.
- [39] N. Kitadai, S. Maruyama, *Geoscience Frontiers* **2018**, *9*, 1117–1153.

- [40] M. P. Johnson, *Essays In Biochemistry* **2016**, *60*, 255–273.
- [41] M. F. Hohmann-Marriott, R. E. Blankenship, *Annu. Rev. Plant Biol.* **2011**, *62*, 515–548.
- [42] R. Guo, J. Gu, S. Zong, M. Wu, M. Yang, *Biomedical Journal* **2018**, *41*, 9–20.
- [43] L. I. Grossman, D. E. Wildman, T. R. Schmidt, M. Goodman, *Trends in Genetics* **2004**, *20*, 578–585.
- [44] G. S. Watson, J. A. Watson, B. W. Cribb, *Annual Review of Entomology* **2017**, *62*, 185–205.
- [45] H. Gao, H. Yao, *Proceedings of the National Academy of Sciences* **2004**, *101*, 7851–7856.
- [46] Rakitov Roman, Gorb Stanislav N., *Proceedings of the Royal Society B: Biological Sciences* **2013**, *280*, 20122391.
- [47] “Biologically inspired LED lens from cuticular nanostructures of firefly lantern | PNAS,” can be found under <https://www.pnas.org/content/109/46/18674>, **n.d.**
- [48] H. Butt, A. K. Yetisen, D. Mistry, S. A. Khan, M. U. Hassan, S. H. Yun, *Advanced Optical Materials* **2016**, *4*, 497–504.
- [49] R. A. Potyrailo, R. K. Bonam, J. G. Hartley, T. A. Starkey, P. Vukusic, M. Vasudev, T. Bunning, R. R. Naik, Z. Tang, M. A. Palacios, et al., *Nat Commun* **2015**, *6*, 7959.
- [50] R. Rakitov, S. N. Gorb, *Proc. Biol. Sci.* **2013**, *280*, 20122391.
- [51] J.-J. Kim, Y. Lee, H. G. Kim, K.-J. Choi, H.-S. Kweon, S. Park, K.-H. Jeong, *PNAS* **2012**, *109*, 18674–18678.
- [52] P. H. Niewiarowski, A. Y. Stark, A. Dhinojwala, *Journal of Experimental Biology* **2016**, *219*, 912–919.
- [53] C. A. Tippetts, Y. Fu, A.-M. Jackson, E. U. Donev, R. Lopez, *J. Opt.* **2016**, *18*, 065105.
- [54] T. Brunette, F. Parmeggiani, P.-S. Huang, G. Bhabha, D. C. Ekiert, S. E. Tsutakawa, G. L. Hura, J. A. Tainer, D. Baker, *Nature* **2015**, *528*, 580–584.
- [55] Y. Hsia, J. B. Bale, S. Gonen, D. Shi, W. Sheffler, K. K. Fong, U. Nattermann, C. Xu, P.-S. Huang, R. Ravichandran, et al., *Nature* **2016**, *535*, 136–139.
- [56] H. Shen, J. A. Fallas, E. Lynch, W. Sheffler, B. Parry, N. Jannetty, J. Decarreau, M. Wagenbach, J. J. Vicente, J. Chen, et al., *Science* **2018**, *362*, 705–709.
- [57] F. F. Miranda, K. Iwasaki, S. Akashi, K. Sumitomo, M. Kobayashi, I. Yamashita, J. R. H. Tame, J. G. Heddle, *Small* **2009**, *5*, 2077–2084.
- [58] L. Miao, Q. Fan, L. Zhao, Q. Qiao, X. Zhang, C. Hou, J. Xu, Q. Luo, J. Liu, *Chem. Commun.* **2016**, *52*, 4092–4095.
- [59] N. C. Seeman, **n.d.**, 23.
- [60] P. W. K. Rothemund, *Nature* **2006**, *440*, 297–302.
- [61] S. R. Dugasani, B. Gnapareddy, M. R. Kesama, S. Jeon, J.-H. Jeong, S. H. Park, *AIP Advances* **2019**, *9*, 015011.
- [62] B. Paulson, I. Shin, H. Jeong, B. Kong, R. Khazaeinezhad, S. R. Dugasani, W. Jung, B. Joo, H.-Y. Lee, S. Park, et al., *Sci Rep* **2018**, *8*, 9358.
- [63] B.-S. Kim, D. J. Mooney, *Trends in Biotechnology* **1998**, *16*, 224–230.
- [64] H. Xing, H. Lee, L. Luo, T. R. Kyriakides, *Biotechnology Advances* **2019**, 107421.
- [65] S. F. Badylak, *Biomaterials* **2007**, *28*, 3587–3593.
- [66] G. S. Hussey, J. L. Dziki, S. F. Badylak, *Nat Rev Mater* **2018**, *3*, 159–173.
- [67] L. E. R. O’Leary, J. A. Fallas, E. L. Bakota, M. K. Kang, J. D. Hartgerink, *Nature Chem* **2011**, *3*, 821–828.
- [68] J. F. Almine, D. V. Bax, S. M. Mithieux, L. Nivison-Smith, J. Rnjak, A. Waterhouse, S. G. Wise, A. S. Weiss, *Chem. Soc. Rev.* **2010**, *39*, 3371.
- [69] R. Wang, J. Ozsvar, G. C. Yeo, A. S. Weiss, *Current Opinion in Chemical Engineering* **2019**, *24*, 54–60.
- [70] **N.d.**

- [71] L. Nilebäck, J. Hedin, M. Widhe, L. S. Floderus, A. Krona, H. Bysell, M. Hedhammar, *Biomacromolecules* **2017**, *18*, 846–854.
- [72] M. M. Fernandes, D. M. Correia, A. da Costa, S. Ribeiro, M. Casal, S. Lanceros-Méndez, R. Machado, *Composites Part B: Engineering* **2018**, *153*, 413–419.
- [73] M. Sohail Haroone, L. Li, A. Ahmad, Y. Huang, R. Ma, P. Zhang, Y. Hu, Q. Muhammad Kaleem, J. Lu, *Journal of Materiomics* **2018**, *4*, 165–171.
- [74] B. Tang, J. Li, X. Hou, T. Afrin, L. Sun, X. Wang, *Ind. Eng. Chem. Res.* **2013**, *52*, 4556–4563.
- [75] G. Zhang, T. Xu, H. Du, Y. Qiao, X. Guo, L. Shi, Y. Zhang, S. Shuang, C. Dong, H. Ma, *J. Mater. Chem. C* **2016**, *4*, 3540–3545.
- [76] J. L. Yarger, B. R. Cherry, A. van der Vaart, *Nat Rev Mater* **2018**, *3*, 18008.
- [77] M. Humenik, T. Scheibel, A. Smith, in *Progress in Molecular Biology and Translational Science*, Elsevier, **2011**, pp. 131–185.
- [78] B. Marelli, N. Patel, T. Duggan, G. Perotto, E. Shirman, C. Li, D. L. Kaplan, F. G. Omenetto, *Proceedings of the National Academy of Sciences* **2017**, *114*, 451–456.
- [79] T. Deptuch, H. Dams-Kozłowska, *Materials* **2017**, *10*, 1417.
- [80] T. P. J. Knowles, T. W. Oppenheim, A. K. Buell, D. Y. Chirgadze, M. E. Welland, *Nature Nanotech* **2010**, *5*, 204–207.
- [81] G. Wei, Z. Su, N. P. Reynolds, P. Arosio, I. W. Hamley, E. Gazit, R. Mezzenga, *Chem. Soc. Rev.* **2017**, *46*, 4661–4708.
- [82] L. Altamura, C. Horvath, S. Rengaraj, A. Rongier, K. Elouarzaki, C. Gondran, A. L. B. Maçon, C. Vendrely, V. Bouchiat, M. Fontecave, et al., *Nature Chem* **2017**, *9*, 157–163.
- [83] A. V. Kajava, *Journal of Structural Biology* **2001**, *134*, 132–144.
- [84] F. Parmeggiani, P.-S. Huang, *Current Opinion in Structural Biology* **2017**, *45*, 116–123.
- [85] M. A. Andrade, C. Perez-Iratxeta, C. P. Ponting, *Journal of Structural Biology* **2001**, *134*, 117–131.
- [86] A. C. Papageorgiou, *The EMBO Journal* **1997**, *16*, 5162–5177.
- [87] E. B. Tikhonova, A. S. Ethayathulla, Y. Su, P. Hariharan, S. Xie, L. Guan, *Sci Rep* **2015**, *5*, 8070.
- [88] A. L. Cortajarena, J. Wang, L. Regan, *FEBS Journal* **2010**, *277*, 1058–1066.
- [89] L. D’Andrea, *Trends in Biochemical Sciences* **2003**, *28*, 655–662.
- [90] D. Romera, P. Couleaud, S. H. Mejias, A. Aires, A. L. Cortajarena, *Biochemical Society Transactions* **2015**, *43*, 825–831.
- [91] C. Scheufler, A. Brinker, G. Bourenkov, S. Pegoraro, L. Moroder, H. Bartunik, F. U. Hartl, I. Moarefi, **n.d.**, 12.
- [92] Y. Daimon, C. Iwama-Masui, Y. Tanaka, T. Shiota, T. Suzuki, R. Miyazaki, H. Sakurada, T. Lithgow, N. Dohmae, H. Mori, et al., *Molecular Microbiology* **2017**, *106*, 760–776.
- [93] H. K. Binz, M. T. Stumpp, P. Forrer, P. Amstutz, **n.d.**, 15.
- [94] T. Aksel, *Biophysical Journal* **n.d.**, 13.
- [95] E. R. G. Main, Y. Xiong, M. J. Cocco, L. D’Andrea, L. Regan, *Structure* **2003**, *11*, 497–508.
- [96] T. Kajander, A. L. Cortajarena, S. Mochrie, L. Regan, *Acta Crystallographica Section D Biological Crystallography* **2007**, *63*, 800–811.
- [97] T. Kajander, A. L. Cortajarena, E. R. G. Main, S. G. J. Mochrie, L. Regan, *Journal of the American Chemical Society* **2005**, *127*, 10188–10190.
- [98] T. J. Magliery, L. Regan, *Journal of Molecular Biology* **2004**, *343*, 731–745.
- [99] A. L. Cortajarena, F. Yi, L. Regan, *ACS Chem. Biol.* **2008**, *3*, 161–166.
- [100] A. L. Cortajarena, T. Y. Liu, M. Hochstrasser, L. Regan, *ACS Chem. Biol.* **2010**, *5*, 545–552.
- [101] A. L. Cortajarena, T. Kajander, W. Pan, M. J. Cocco, L. Regan, *Protein Engineering Design and Selection* **2004**, *17*, 399–409.
- [102] A. L. Cortajarena, S. G. J. Mochrie, L. Regan, *Protein Science* **2011**, *20*, 1042–1047.

- [103] A. Aires, E. Lopez-Martinez, A. Cortajarena, *Biosensors* **2018**, *8*, 110.
- [104] A. Aires, J. F. Cadenas, R. Guantes, A. L. Cortajarena, *Nanoscale* **2017**, *9*, 13760–13771.
- [105] J. López-Andarias, S. H. Mejías, T. Sakurai, W. Matsuda, S. Seki, F. Feixas, S. Osuna, C. Atienza, N. Martín, A. L. Cortajarena, *Advanced Functional Materials* **2018**, *28*, 1704031.
- [106] S. H. Mejías, J. López-Andarias, T. Sakurai, S. Yoneda, K. P. Erazo, S. Seki, C. Atienza, N. Martín, A. L. Cortajarena, *Chemical Science* **2016**, *7*, 4842–4847.
- [107] Jacob Israelachvili, Richard Pashley, *Nature* **1982**, *300*, 341–342.
- [108] E. E. Meyer, K. J. Rosenberg, J. Israelachvili, *Proceedings of the National Academy of Sciences* **2006**, *103*, 15739–15746.
- [109] C.-J. Tsai, J. Zheng, C. Alemán, R. Nussinov, *Trends in Biotechnology* **2006**, *24*, 449–454.
- [110] C.-J. Tsai, J. Zheng, D. Zanuy, N. Haspel, H. Wolfson, C. Alemán, R. Nussinov, *Proteins* **2007**, *68*, 1–12.
- [111] D. Sanchez-deAlcazar, S. H. Mejias, K. Erazo, B. Sot, A. L. Cortajarena, *Journal of Structural Biology* **2018**, *201*, 118–129.
- [112] C. O. S. Sorzano, J. R. Bilbao-Castro, Y. Shkolnisky, M. Alcorlo, R. Melero, G. Caffarena-Fernández, M. Li, G. Xu, R. Marabini, J. M. Carazo, *Journal of Structural Biology* **2010**, *171*, 197–206.
- [113] S. J. Ludtke, P. R. Baldwin, W. Chiu, *Journal of Structural Biology* **1999**, *128*, 82–97.
- [114] S. R. Comeau, D. W. Gatchell, S. Vajda, C. J. Camacho, *Nucleic Acids Research* **2004**, *32*, W96–W99.
- [115] S. R. Comeau, D. W. Gatchell, S. Vajda, C. J. Camacho, **n.d.**, 6.
- [116] D. Kozakov, D. Beglov, T. Bohnuud, S. E. Mottarella, B. Xia, D. R. Hall, S. Vajda, *Proteins* **2013**, *81*, 2159–2166.
- [117] A. V. Kajava, *Journal of Structural Biology* **2001**, *134*, 132–144.
- [118] Y.-T. Lai, D. Cascio, T. O. Yeates, *Science* **2012**, *336*, 1129–1129.
- [119] T. O. Yeates, *Nature Nanotech* **2011**, *6*, 541–542.
- [120] **N.d.**
- [121] W. W. Newcomb, F. L. Homa, D. R. Thomsen, F. P. Booy, B. L. Trus, A. C. Steven, J. V. Spencer, J. C. Brown, *Journal of Molecular Biology* **1996**, *263*, 432–446.
- [122] M. Silverman, M. Simon, *Nature* **1974**, *249*, 73–74.
- [123] D. S. Goodsell, A. J. Olson, *Annual Review of Biophysics and Biomolecular Structure* **2000**, *29*, 105–153.
- [124] M. H. Ali, B. Imperiali, *Bioorganic & Medicinal Chemistry* **2005**, *13*, 5013–5020.
- [125] J. Monod, J. Wyman, J.-P. Changeux, *Journal of Molecular Biology* **1965**, *12*, 88–118.
- [126] Y. Ofran, B. Rost, *Journal of Molecular Biology* **2003**, *325*, 377–387.
- [127] C. Chothia, J. Janin, *Nature* **1975**, *256*, 705–708.
- [128] C. Deremble, R. Lavery, *Current Opinion in Structural Biology* **2005**, *15*, 171–175.
- [129] H. Ponstingl, Thomas Kabir, D. Gorse, J. M. Thornton, *Progress in Biophysics and Molecular Biology* **2005**, *89*, 9–35.
- [130] D. Reichmann, O. Rahat, M. Cohen, H. Neuvirth, G. Schreiber, *Current Opinion in Structural Biology* **2007**, *17*, 67–76.
- [131] S. J. Wodak, J. Janin, *Adv. Protein Chem.* **2002**, *61*, 9–73.
- [132] C. Yan, F. Wu, R. L. Jernigan, D. Dobbs, V. Honavar, *Protein J.* **2008**, *27*, 59–70.
- [133] D. Pum, J. L. Toca-Herrera, U. B. Sleytr, *Int J Mol Sci* **2013**, *14*, 2484–2501.
- [134] J. Raff, S. Matys, M. Suhr, M. Vogel, T. Günther, K. Pollmann, in *Protein-Based Engineered Nanostructures* (Eds.: A.L. Cortajarena, T.Z. Grove), Springer International Publishing, Cham, **2016**, pp. 245–279.
- [135] D. L. Caspar, D. A. Goodenough, L. Makowski, W. C. Phillips, *J. Cell Biol.* **1977**, *74*, 605–628.

- [136] J. E. Rash, K. G. V. Davidson, T. Yasumura, C. S. Furman, *Neuroscience* **2004**, *129*, 915–934.
- [137] M. G. Mateu, *Adv. Exp. Med. Biol.* **2016**, *940*, 83–120.
- [138] M. C. Morais, *Proc. Natl. Acad. Sci. U.S.A.* **2016**, *113*, 11390–11392.
- [139] T. L. Blundell, N. Srinivasan, *Proc. Natl. Acad. Sci. U.S.A.* **1996**, *93*, 14243–14248.
- [140] K. Rajagopal, J. P. Schneider, *Current Opinion in Structural Biology* **2004**, *14*, 480–486.
- [141] R. V. Ulijn, A. M. Smith, *Chem Soc Rev* **2008**, *37*, 664–675.
- [142] D. N. Woolfson, Z. N. Mahmoud, *Chem Soc Rev* **2010**, *39*, 3464–3479.
- [143] J.-M. Lehn, *PNAS* **2002**, *99*, 4763–4768.
- [144] E. Gazit, *Nat Nanotechnol* **2008**, *3*, 8–9.
- [145] T. F. A. De Greef, M. M. J. Smulders, M. Wolffs, A. P. H. J. Schenning, R. P. Sijbesma, E. W. Meijer, *Chem. Rev.* **2009**, *109*, 5687–5754.
- [146] D. Papapostolou, A. M. Smith, E. D. T. Atkins, S. J. Oliver, M. G. Ryadnov, L. C. Serpell, D. N. Woolfson, *Proceedings of the National Academy of Sciences of the United States of America* **2007**, *104*, 10853–10858.
- [147] J. Zheng, J. J. Birktoft, Y. Chen, T. Wang, R. Sha, P. E. Constantinou, S. L. Ginell, C. Mao, N. C. Seeman, *Nature* **2009**, *461*, 74–77.
- [148] L. Jaeger, A. Chworos, *Curr. Opin. Struct. Biol.* **2006**, *16*, 531–543.
- [149] C. J. Delebecque, A. B. Lindner, P. A. Silver, F. A. Aldaye, *Science* **2011**, *333*, 470–474.
- [150] I. Cherny, E. Gazit, *Angew. Chem. Int. Ed. Engl.* **2008**, *47*, 4062–4069.
- [151] E. Gazit, *Chem. Soc. Rev.* **2007**, *36*, 1263–1269.
- [152] S. L. Gras, A. K. Tickler, A. M. Squires, G. L. Devlin, M. A. Horton, C. M. Dobson, C. E. MacPhee, *Biomaterials* **2008**, *29*, 1553–1562.
- [153] C. A. E. Hauser, S. Zhang, *Chem Soc Rev* **2010**, *39*, 2780–2790.
- [154] J. P. Jung, J. Z. Gasiorowski, J. H. Collier, *Biopolymers* **2010**, *94*, 49–59.
- [155] J. B. Matson, R. H. Zha, S. I. Stupp, *Current Opinion in Solid State and Materials Science* **2011**, *15*, 225–235.
- [156] A. Aggeli, M. Bell, N. Boden, J. N. Keen, P. F. Knowles, T. C. McLeish, M. Pitkeathly, S. E. Radford, *Nature* **1997**, *386*, 259–262.
- [157] E. F. Banwell, E. S. Abelardo, D. J. Adams, M. A. Birchall, A. Corrigan, A. M. Donald, M. Kirkland, L. C. Serpell, M. F. Butler, D. N. Woolfson, *Nature Mater* **2009**, *8*, 596–600.
- [158] M. J. Pandya, G. M. Spooner, M. Sunde, J. R. Thorpe, A. Rodger, D. N. Woolfson, *Biochemistry* **2000**, *39*, 8728–8734.
- [159] J. P. Schneider, D. J. Pochan, B. Ozbas, K. Rajagopal, L. Pakstis, J. Kretsinger, *J. Am. Chem. Soc.* **2002**, *124*, 15030–15037.
- [160] R. V. Ulijn, D. N. Woolfson, *Chem. Soc. Rev.* **2010**, *39*, 3349–3350.
- [161] S. Zhang, M. A. Greenfield, A. Mata, L. C. Palmer, R. Bitton, J. R. Mantei, C. Aparicio, M. O. de la Cruz, S. I. Stupp, *Nature Mater* **2010**, *9*, 594–601.
- [162] J. M. Fletcher, R. L. Harniman, F. R. H. Barnes, A. L. Boyle, A. Collins, J. Mantell, T. H. Sharp, M. Antognozzi, P. J. Booth, N. Linden, et al., *Science* **2013**, *340*, 595–599.
- [163] J. G. Heddle, *Nanotechnol Sci Appl* **2008**, *1*, 67–78.
- [164] A. Fegan, B. White, J. C. T. Carlson, C. R. Wagner, *Chem. Rev.* **2010**, *110*, 3315–3336.
- [165] A. L. Cortajarena, T. Grove, Eds., *Protein-Based Engineered Nanostructures*, Springer International Publishing, **2016**.
- [166] S. Howorka, *Curr. Opin. Biotechnol.* **2011**, *22*, 485–491.
- [167] Y.-T. Lai, N. P. King, T. O. Yeates, *Trends Cell Biol.* **2012**, *22*, 653–661.
- [168] D. Papapostolou, S. Howorka, *Mol Biosyst* **2009**, *5*, 723–732.
- [169] D. Grueninger, N. Treiber, M. O. P. Ziegler, J. W. A. Koetter, M.-S. Schulze, G. E. Schulz, *Science* **2008**, *319*, 206–209.

- [170] J. Clarke, L. Regan, *Curr. Opin. Struct. Biol.* **2010**, *20*, 480–481.
- [171] R. de la Rica, H. Matsui, *Chem. Soc. Rev.* **2010**, *39*, 3499–3509.
- [172] Y. Lim, K.-S. Moon, M. Lee, *Chem Soc Rev* **2009**, *38*, 925–934.
- [173] M. Zelzer, R. V. Ulijn, *Chem Soc Rev* **2010**, *39*, 3351–3357.
- [174] J. D. Brodin, X. I. Ambroggio, C. Tang, K. N. Parent, T. S. Baker, F. A. Tezcan, *Nature Chem* **2012**, *4*, 375–382.
- [175] N. A. Carter, T. Z. Grove, *Biomacromolecules* **2015**, *16*, 706–714.
- [176] T. Z. Grove, L. Regan, A. L. Cortajarena, *J. R. Soc. Interface* **2013**, *10*, 20130051.
- [177] S. H. Mejías, B. Sot, R. Guantes, A. L. Cortajarena, *Nanoscale* **2014**, *6*, 10982–10988.
- [178] J. C. Sinclair, K. M. Davies, C. Vénien-Bryan, M. E. M. Noble, *Nature Nanotech* **2011**, *6*, 558–562.
- [179] H. Gradišar, S. Božič, T. Doles, D. Vengust, I. Hafner-Bratkovič, A. Mertelj, B. Webb, A. Šali, S. Klavžar, R. Jerala, *Nat Chem Biol* **2013**, *9*, 362–366.
- [180] N. P. King, W. Sheffler, M. R. Sawaya, B. S. Vollmar, J. P. Sumida, I. André, T. Gonen, T. O. Yeates, D. Baker, *Science* **2012**, *336*, 1171–1174.
- [181] D. N. Woolfson, G. J. Bartlett, A. J. Burton, J. W. Heal, A. Niitsu, A. R. Thomson, C. W. Wood, *Curr. Opin. Struct. Biol.* **2015**, *33*, 16–26.
- [182] M. A. Andrade, C. Perez-Iratxeta, C. P. Ponting, *Journal of Structural Biology* **2001**, *134*, 117–131.
- [183] A. L. Cortajarena, S. G. J. Mochrie, L. Regan, *Protein Science* **2011**, *20*, 1042–1047.
- [184] A. L. Cortajarena, S. G. J. Mochrie, L. Regan, *Protein Sci.* **2011**, *20*, 1042–1047.
- [185] Y. L. Boersma, A. Plückthun, *Curr. Opin. Biotechnol.* **2011**, *22*, 849–857.
- [186] A. L. Cortajarena, T. Y. Liu, M. Hochstrasser, L. Regan, *ACS Chem. Biol.* **2010**, *5*, 545–552.
- [187] M. E. Jackrel, A. L. Cortajarena, T. Y. Liu, L. Regan, *ACS Chem. Biol.* **2010**, *5*, 553–562.
- [188] R. Parker, A. Mercedes-Camacho, T. Z. Grove, *Protein Sci.* **2014**, *23*, 790–800.
- [189] E. R. G. Main, J. J. Phillips, C. Millership, *Biochem. Soc. Trans.* **2013**, *41*, 1152–1158.
- [190] D. Romera, P. Couleaud, S. H. Mejias, A. Aires, A. L. Cortajarena, *Biochem. Soc. Trans.* **2015**, *43*, 825–831.
- [191] E. R. G. Main, A. R. Lowe, S. G. J. Mochrie, S. E. Jackson, L. Regan, *Curr. Opin. Struct. Biol.* **2005**, *15*, 464–471.
- [192] S. H. Mejias, A. Aires, P. Couleaud, A. L. Cortajarena, *Adv. Exp. Med. Biol.* **2016**, *940*, 61–81.
- [193] F. Parmeggiani, P.-S. Huang, *Curr. Opin. Struct. Biol.* **2017**, *45*, 116–123.
- [194] T. Brunette, F. Parmeggiani, P.-S. Huang, G. Bhabha, D. C. Ekiert, S. E. Tsutakawa, G. L. Hura, J. A. Tainer, D. Baker, *Nature* **2015**, *528*, 580–584.
- [195] L. Doyle, J. Hallinan, J. Bolduc, F. Parmeggiani, D. Baker, B. L. Stoddard, P. Bradley, *Nature* **2015**, *528*, 585–588.
- [196] K. Park, B. W. Shen, F. Parmeggiani, P.-S. Huang, B. L. Stoddard, D. Baker, *Nat. Struct. Mol. Biol.* **2015**, *22*, 167–174.
- [197] L. D. D’Andrea, L. Regan, *Trends Biochem. Sci.* **2003**, *28*, 655–662.
- [198] E. R. G. Main, Y. Xiong, M. J. Cocco, L. D’Andrea, L. Regan, *Structure* **2003**, *11*, 497–508.
- [199] T. Kajander, A. L. Cortajarena, L. Regan, *Methods Mol. Biol.* **2006**, *340*, 151–170.
- [200] T. J. Magliery, L. Regan, *Journal of Molecular Biology* **2004**, *343*, 731–745.
- [201] T. Z. Grove, M. Hands, L. Regan, *Protein Eng Des Sel* **2010**, *23*, 449–455.
- [202] T. Kajander, A. L. Cortajarena, S. Mochrie, L. Regan, *Acta Crystallogr. D Biol. Crystallogr.* **2007**, *63*, 800–811.
- [203] M. Khan, I. Khan, M. N. Umar, D.-H. Oh, *IET Nanobiotechnology* **2015**, *9*, 396–400.
- [204] A. Biswas, I. S. Bayer, A. S. Biris, T. Wang, E. Dervishi, F. Faupel, *Advances in Colloid and Interface Science* **2012**, *170*, 2–27.

- [205] S. Li, Q. Jiang, S. Liu, Y. Zhang, Y. Tian, C. Song, J. Wang, Y. Zou, G. J. Anderson, J.-Y. Han, et al., *Nat Biotechnol* **2018**, *36*, 258–264.
- [206] P. K. Lo, P. Karam, F. A. Aldaye, C. K. McLaughlin, G. D. Hamblin, G. Cosa, H. F. Sleiman, *Nature Chem* **2010**, *2*, 319–328.
- [207] T. Gerling, K. F. Wagenbauer, A. M. Neuner, H. Dietz, **n.d.**, 8.
- [208] N. A. W. Bell, U. F. Keyser, *FEBS Letters* **2014**, *588*, 3564–3570.
- [209] S. Mashaghi, T. Jadidi, G. Koenderink, A. Mashaghi, *IJMS* **2013**, *14*, 4242–4282.
- [210] D. Tesauro, A. Accardo, C. Diaferia, V. Milano, J. Guillon, L. Ronga, F. Rossi, *Molecules* **2019**, *24*, 351.
- [211] K. DeFrates, T. Markiewicz, P. Gallo, A. Rack, A. Weyhmler, B. Jarmusik, X. Hu, *IJMS* **2018**, *19*, 1717.
- [212] X. Hu, A. Guiseppi-Elie, C. Z. Dinu, *Nanoscale* **2019**, *11*, 4987–4998.
- [213] T. Komatsu, *Nanoscale* **2012**, *4*, 1910–1918.
- [214] A. B. Seabra, N. Durán, *Peptides* **2013**, *39*, 47–54.
- [215] A. J. Burton, F. Thomas, C. Agnew, K. L. Hudson, S. E. Halford, R. L. Brady, D. N. Woolfson, *J. Am. Chem. Soc.* **2013**, *135*, 12524–12527.
- [216] I. W. Hamley, *Angewandte Chemie International Edition* **2014**, *53*, 6866–6881.
- [217] C. R. Martin, P. Kohli, *Nat Rev Drug Discov* **2003**, *2*, 29–37.
- [218] M. Reches, E. Gazit, *Science* **2003**, *300*, 625–627.
- [219] M. R. Ghadiri, J. R. Granja, R. A. Milligan, D. E. McRee, N. Khazanovich, *Nature* **1993**, *366*, 324–327.
- [220] J. Hume, J. Sun, R. Jacquet, P. D. Renfrew, J. A. Martin, R. Bonneau, M. L. Gilchrist, J. K. Montclare, *Biomacromolecules* **2014**, *15*, 3503–3510.
- [221] S. A. Potekhin, T. N. Melnik, V. Popov, N. F. Lanina, A. A. Vazina, P. Rigler, A. S. Verdini, G. Corradin, A. V. Kajava, *Chemistry & Biology* **2001**, *8*, 1025–1032.
- [222] C. Xu, R. Liu, A. K. Mehta, R. C. Guerrero-Ferreira, E. R. Wright, S. Dunin-Horkawicz, K. Morris, L. C. Serpell, X. Zuo, J. S. Wall, et al., *J. Am. Chem. Soc.* **2013**, *135*, 15565–15578.
- [223] E. H. Egelman, C. Xu, F. DiMaio, E. Magnotti, C. Modlin, X. Yu, E. Wright, D. Baker, V. P. Conticello, *Structure* **2015**, *23*, 280–289.
- [224] C. Valéry, M. Paternostre, B. Robert, T. Gulik-Krzywicki, T. Narayanan, J.-C. Dedieu, G. Keller, M.-L. Torres, R. Cherif-Cheikh, P. Calvo, et al., *Proc Natl Acad Sci U S A* **2003**, *100*, 10258–10262.
- [225] N. C. Burgess, T. H. Sharp, F. Thomas, C. W. Wood, A. R. Thomson, N. R. Zaccai, R. L. Brady, L. C. Serpell, D. N. Woolfson, *J. Am. Chem. Soc.* **2015**, *137*, 10554–10562.
- [226] A. R. Thomson, C. W. Wood, A. J. Burton, G. J. Bartlett, R. B. Sessions, R. L. Brady, D. N. Woolfson, *Science* **2014**, *346*, 485–488.
- [227] N. R. Zaccai, B. Chi, A. R. Thomson, A. L. Boyle, G. J. Bartlett, M. Bruning, N. Linden, R. B. Sessions, P. J. Booth, R. L. Brady, et al., *Nat. Chem. Biol.* **2011**, *7*, 935–941.
- [228] R. Chapman, M. Daniai, M. Liang Koh, K. A. Jolliffe, S. Perrier, *Chemical Society Reviews* **2012**, *41*, 6023–6041.
- [229] A. Petrov, G. F. Audette, *WIREs Nanomed Nanobiotechnol* **2012**, *4*, 575–585.
- [230] Y. Bai, Q. Luo, J. Liu, *Chem. Soc. Rev.* **2016**, *45*, 2756–2767.
- [231] I. Uddin, S. Frank, M. J. Warren, R. W. Pickersgill, *Small* **2018**, *14*, 1704020.
- [232] F. F. Miranda, K. Iwasaki, S. Akashi, K. Sumitomo, M. Kobayashi, I. Yamashita, J. R. H. Tame, J. G. Hedde, *Small* **2009**, *5*, 2077–2084.
- [233] E. R. Ballister, A. H. Lai, R. N. Zuckermann, Y. Cheng, J. D. Mougous, *Proceedings of the National Academy of Sciences* **2008**, *105*, 3733–3738.

- [234] I. Medalsy, O. Dgany, M. Sowwan, H. Cohen, A. Yukashevskaya, S. G. Wolf, A. Wolf, A. Koster, O. Almog, I. Marton, et al., *Nano Lett.* **2008**, *8*, 473–477.
- [235] N. H. Hopcroft, A. Manfredo, A. L. Wendt, A. M. Brzozowski, P. Gollnick, A. A. Antson, *Journal of Molecular Biology* **2004**, *338*, 43–53.
- [236] S. Nagano, E. F. Banwell, K. Iwasaki, M. Michalak, R. Pałka, K. Y. J. Zhang, A. R. D. Voet, J. G. Hedde, *Adv. Mater. Interfaces* **2016**, *3*, 1600846.
- [237] T. K. Nguyen, H. Negishi, S. Abe, T. Ueno, *Chem. Sci.* **2019**, *10*, 1046–1051.
- [238] S. A. Hughes, F. Wang, S. Wang, M. A. B. Kreutzberger, T. Osinski, A. Orlova, J. S. Wall, X. Zuo, E. H. Egelman, V. P. Conticello, *Proc Natl Acad Sci USA* **2019**, *116*, 14456–14464.
- [239] W. Wang, L. Wang, H. Chen, J. Zang, X. Zhao, G. Zhao, H. Wang, *J. Am. Chem. Soc.* **2018**, *140*, 14078–14081.
- [240] C. N. Pace, F. Vajdos, L. Fee, G. Grimsley, T. Gray, *Protein Sci.* **1995**, *4*, 2411–2423.
- [241] J. A. Mindell, N. Grigorieff, *J. Struct. Biol.* **2003**, *142*, 334–347.
- [242] R. Marabini, I. M. Masegosa, M. C. San Martín, S. Marco, J. J. Fernández, L. G. de la Fraga, C. Vaquerizo, J. M. Carazo, *Journal of Structural Biology* **1996**, *116*, 237–240.
- [243] S. H. W. Scheres, M. Valle, R. Nuñez, C. O. S. Sorzano, R. Marabini, G. T. Herman, J.-M. Carazo, *J. Mol. Biol.* **2005**, *348*, 139–149.
- [244] S. Lyskov, J. J. Gray, *Nucleic Acids Res.* **2008**, *36*, W233–238.
- [245] J. J. Phillips, C. Millership, E. R. G. Main, *Angew. Chem. Int. Ed. Engl.* **2012**, *51*, 13132–13135.
- [246] D. Zilberstein, V. Agmon, S. Schuldiner, E. Padan, *J. Bacteriol.* **1984**, *158*, 246–252.
- [247] A. M. Krachler, A. Sharma, C. Kleanthous, *Proteins* **2010**, *78*, 2131–2143.
- [248] D. Kozakov, D. R. Hall, B. Xia, K. A. Porter, D. Padhorny, C. Yueh, D. Beglov, S. Vajda, *Nat Protoc* **2017**, *12*, 255–278.
- [249] D. N. Woolfson, *Subcell. Biochem.* **2017**, *82*, 35–61.
- [250] D. N. Woolfson, G. J. Bartlett, M. Bruning, A. R. Thomson, *Curr. Opin. Struct. Biol.* **2012**, *22*, 432–441.
- [251] A. J. Burton, A. R. Thomson, W. M. Dawson, R. L. Brady, D. N. Woolfson, *Nature Chem* **2016**, *8*, 837–844.
- [252] P. J. E. Rowling, E. M. Sivertsson, A. Perez-Riba, E. R. G. Main, L. S. Itzhaki, *Biochem. Soc. Trans.* **2015**, *43*, 881–888.
- [253] T. Z. Grove, L. Regan, A. L. Cortajarena, *Journal of The Royal Society Interface* **2013**, *10*, 20130051–20130051.
- [254] A. L. Cortajarena, L. Regan, *Protein Science* **2011**, *20*, 336–340.
- [255] N. Pourdavoud, A. Mayer, M. Buchmüller, K. Brinkmann, T. Häger, T. Hu, R. Heiderhoff, I. Shutsko, P. Görrn, Y. Chen, et al., *Adv. Mater. Technol.* **2018**, *3*, 1700253.
- [256] M. Umar, K. Min, S. Kim, *Sensors and Actuators B: Chemical* **2018**, *255*, 3207–3215.
- [257] Q. Li, Y. Huang, J. Ning, C. Jiang, X. Wang, H. Chen, X. Li, R. Zhang, K. Zhang, J. Min, et al., *Nanoscale Res Lett* **2018**, *13*, 267.
- [258] V. DeMiguel-Soto, D. Leandro, M. Lopez-Amo, *Opt. Express* **2018**, *26*, 27189.
- [259] J. Mysliwiec, K. Cypriach, L. Sznitko, A. Miniewicz, *J. Opt.* **2017**, *19*, 033003.
- [260] Z. Yu, W. Li, J. A. Hagen, Y. Zhou, D. Klotzkin, J. G. Grote, A. J. Steckl, *Appl. Opt.* **2007**, *46*, 1507.
- [261] R. R. da Silva, C. T. Dominguez, M. V. dos Santos, R. Barbosa-Silva, M. Cavicchioli, L. M. Christovan, L. S. A. de Melo, A. S. L. Gomes, C. B. de Araújo, S. J. L. Ribeiro, *J. Mater. Chem. C* **2013**, *1*, 7181.
- [262] M. C. Gather, S. H. Yun, *Nature Photon* **2011**, *5*, 406–410.
- [263] C. Vannahme, F. Maier-Flaig, U. Lemmer, A. Kristensen, *Lab Chip* **2013**, *13*, 2675.

- [264] R. R. da Silva, C. T. Dominguez, M. V. dos Santos, R. Barbosa-Silva, M. Cavicchioli, L. M. Christovan, L. S. A. de Melo, A. S. L. Gomes, C. B. de Araújo, S. J. L. Ribeiro, *Journal of Materials Chemistry C* **2013**, *1*, 7181.
- [265] S. Terdale, A. Tantray, *Journal of Molecular Liquids* **2017**, *225*, 662–671.
- [266] D. Lusic, C. Coromelci-Pastravanu, I. Cretescu, I. Poullos, C.-D. Stan, *International Journal of Photoenergy* **2012**, *2012*, 1–8.
- [267] F. Yang, Y. Chu, L. Huo, Y. Yang, Y. Liu, J. Liu, *Journal of Solid State Chemistry* **2006**, *179*, 457–463.
- [268] L. Malfatti, T. Kidchob, D. Aiello, R. Aiello, F. Testa, P. Innocenzi, *J. Phys. Chem. C* **2008**, *112*, 16225–16230.
- [269] F. L. Arbeloa, P. R. Ojeda, I. L. Arbeloa, *J. Chem. Soc., Faraday Trans. 2* **1988**, *84*, 1903.
- [270] O. Koniev, A. Wagner, *Chem. Soc. Rev.* **2015**, *44*, 5495–5551.
- [271] E. Fresta, V. Fernández-Luna, P. B. Coto, R. D. Costa, *Advanced Functional Materials* **2018**, *28*, 1707011.
- [272] A. J. C. Kuehne, M. C. Gather, *Chem. Rev.* **2016**, *116*, 12823–12864.
- [273] “Biophotonics for Medical Applications - 1st Edition,” can be found under <https://www.elsevier.com/books/biophotonics-for-medical-applications/meglinski/978-0-85709-662-3>, **n.d.**
- [274] N. C. Abascal, L. Regan, *Open Biol* **2018**, *8*, DOI 10.1098/rsob.180113.
- [275] Y. Sun, Z. Guo, *Nanoscale Horiz.* **2018**, *4*, 52–76.
- [276] Z. Liu, Z. Zhang, R. O. Ritchie, *Adv. Mater. Weinheim* **2018**, *30*, e1705220.
- [277] C. Zhang, D. A. Mcadams, J. C. Grunlan, *Adv. Mater. Weinheim* **2016**, *28*, 6292–6321.
- [278] V. Fernández-Luna, P. B. Coto, R. D. Costa, *Angew. Chem. Int. Ed. Engl.* **2018**, *57*, 8826–8836.
- [279] W. Huang, S. Ling, C. Li, F. G. Omenetto, D. L. Kaplan, *Chem Soc Rev* **2018**, *47*, 6486–6504.
- [280] H. Tao, D. L. Kaplan, F. G. Omenetto, *Adv. Mater. Weinheim* **2012**, *24*, 2824–2837.
- [281] Y. Wang, D. Aurelio, W. Li, P. Tseng, Z. Zheng, M. Li, D. L. Kaplan, M. Liscidini, F. G. Omenetto, *Adv. Mater. Weinheim* **2017**, *29*, DOI 10.1002/adma.201702769.
- [282] Z. Zheng, J. Wu, M. Liu, H. Wang, C. Li, M. J. Rodriguez, G. Li, X. Wang, D. L. Kaplan, *Adv Healthc Mater* **2018**, *7*, e1701026.
- [283] B. D. Lawrence, M. Cronin-Golomb, I. Georgakoudi, D. L. Kaplan, F. G. Omenetto, *Biomacromolecules* **2008**, *9*, 1214–1220.
- [284] C. Holland, K. Numata, J. Rnjak-Kovacina, F. P. Seib, *Adv Healthc Mater* **2019**, *8*, e1800465.
- [285] E. Gazit, *Nature Chemistry* **2010**, *2*, 1010–1011.
- [286] S. Božič, T. Doles, H. Gradišar, R. Jerala, *Curr Opin Chem Biol* **2013**, *17*, 940–945.
- [287] J. S. Fletcher, N. P. Lockyer, S. Vaidyanathan, J. C. Vickerman, *Anal. Chem.* **2007**, *79*, 2199–2206.
- [288] T. Z. Grove, L. Regan, *Current Opinion in Structural Biology* **2012**, *22*, 451–456.
- [289] T. Kajander, A. L. Cortajarena, E. R. G. Main, S. G. J. Mochrie, L. Regan, *J. Am. Chem. Soc.* **2005**, *127*, 10188–10190.
- [290] A. L. Cortajarena, J. Wang, L. Regan, *FEBS Journal* **2010**, *277*, 1058–1066.
- [291] N. A. Carter, T. Z. Grove, *J. Am. Chem. Soc.* **2018**, *140*, 7144–7151.
- [292] A. L. Cortajarena, F. Yi, L. Regan, *ACS Chem. Biol.* **2008**, *3*, 161–166.
- [293] A. L. Cortajarena, T. Kajander, W. Pan, M. J. Cocco, L. Regan, *Protein Engineering Design and Selection* **2004**, *17*, 399–409.
- [294] S. H. Mejías, J. López-Andarias, T. Sakurai, S. Yoneda, K. P. Erazo, S. Seki, C. Atienza, N. Martín, A. L. Cortajarena, *Chem Sci* **2016**, *7*, 4842–4847.

- [295] P. Couleaud, S. Adan-Bermudez, A. Aires, S. H. Mejías, B. Sot, A. Somoza, A. L. Cortajarena, *Biomacromolecules* **2015**, *16*, 3836–3844.
- [296] D. J. Lipomi, R. V. Martinez, L. Cademartiri, G. M. Whitesides, *Polymer Science: A Comprehensive Reference*, Elsevier BV, Amsterdam, **2012**.
- [297] K. Ramanathan, M. A. Bangar, M. Yun, W. Chen, N. V. Myung, A. Mulchandani, *J. Am. Chem. Soc.* **2005**, *127*, 496–497.
- [298] J. Hong, J. B. Edel, A. J. deMello, *Drug Discov. Today* **2009**, *14*, 134–146.
- [299] E. Menard, M. A. Meitl, Y. Sun, J.-U. Park, D. J.-L. Shir, Y.-S. Nam, S. Jeon, J. A. Rogers, *Chem. Rev.* **2007**, *107*, 1117–1160.
- [300] H. Arakawa, M. Aresta, J. N. Armor, M. A. Barteau, E. J. Beckman, A. T. Bell, J. E. Bercaw, C. Creutz, E. Dinjus, D. A. Dixon, et al., *Chem. Rev.* **2001**, *101*, 953–996.
- [301] M. E. Stewart, C. R. Anderton, L. B. Thompson, J. Maria, S. K. Gray, J. A. Rogers, R. G. Nuzzo, *Chem. Rev.* **2008**, *108*, 494–521.
- [302] B. J. Wiley, D. J. Lipomi, J. Bao, F. Capasso, G. M. Whitesides, *Nano Lett* **2008**, *8*, 3023–3028.
- [303] D.-H. Kim, J.-H. Ahn, W. M. Choi, H.-S. Kim, T.-H. Kim, J. Song, Y. Y. Huang, Z. Liu, C. Lu, J. A. Rogers, *Science* **2008**, *320*, 507–511.
- [304] B. D. Gates, Q. Xu, M. Stewart, D. Ryan, C. G. Willson, G. M. Whitesides, *Chem. Rev.* **2005**, *105*, 1171–1196.
- [305] Y. Xia, J. A. Rogers, K. E. Paul, G. M. Whitesides, *Chem. Rev.* **1999**, *99*, 1823–1848.
- [306] A. Mujahid, N. Iqbal, A. Afzal, *Biotechnol. Adv.* **2013**, *31*, 1435–1447.
- [307] M. A. Brenckle, H. Tao, S. Kim, M. Paquette, D. L. Kaplan, F. G. Omenetto, *Adv Mater* **2013**, *25*, 2409–2414.
- [308] Z. Zhou, Z. Shi, X. Cai, S. Zhang, S. G. Corder, X. Li, Y. Zhang, G. Zhang, L. Chen, M. Liu, et al., *Adv. Mater. Weinheim* **2017**, *29*, DOI 10.1002/adma.201605471.
- [309] A. Espinha, C. Dore, C. Matricardi, M. I. Alonso, A. R. Goñi, A. Mihi, *Nat Photonics* **2018**, *12*, 343–348.
- [310] D. Sánchez-deAlcázar, S. Velasco-Lozano, N. Zeballos, F. López-Gallego, A. L. Cortajarena, *ChemBioChem* **2019**, *20*, 1977–1985.
- [311] T. B. Queiroz, M. B. S. Botelho, L. De Boni, H. Eckert, A. S. S. de Camargo, *Journal of Applied Physics* **2013**, *113*, 113508–1.
- [312] A. L. Cortajarena, G. Lois, E. Sherman, C. S. O’Hern, L. Regan, G. Haran, *J. Mol. Biol.* **2008**, *382*, 203–212.
- [313] G. Ghosh, *Appl. Opt., AO* **1997**, *36*, 1540–1546.
- [314] E. Vasileva, Y. Li, I. Sychugov, M. Mensi, L. Berglund, S. Popov, *Advanced Optical Materials* **2017**, *5*, 1700057.
- [315] S. Forget, S. Chénais, *Organic Solid-State Lasers*, Springer-Verlag, Berlin Heidelberg, **2013**.
- [316] J. López-Andarias, S. H. Mejías, T. Sakurai, W. Matsuda, S. Seki, F. Feixas, S. Osuna, C. Atienza, N. Martín, A. L. Cortajarena, *Advanced Functional Materials* **2018**, *28*, 1704031.
- [317] N. Tsutsumi, M. Shinobu, *Appl. Phys. B* **2011**, *105*, 839–845.
- [318] Y. Xu, G. Hai, H. Xu, H. Zhang, Z. Zuo, Q. Zhang, R. Xia, C. Sun, J. Castro-Smirnov, A. Sousaraei, et al., *Advanced Optical Materials* **2018**, *6*, 1800263.
- [319] M. Fischer, J. Georges, *Chemical Physics Letters* **1996**, *260*, 115.
- [320] P. Yang, G. Wirnsberger, H. C. Huang, S. R. Cordero, M. D. McGehee, B. Scott, T. Deng, G. M. Whitesides, B. F. Chmelka, S. K. Buratto, et al., *Science* **2000**, *287*, 465–468.
- [321] F. Marlow, M. D. McGehee, D. Zhao, B. F. Chmelka, G. D. Stucky, *Advanced Materials* **1999**, *11*, 632–636.
- [322] J. C. Altman, R. E. Stone, B. Dunn, F. Nishida, *IEEE Photonics Technology Letters* **1991**, *3*, 189–190.

- [323] N. U. Wetter, A. R. de Miranda, É. Pecoraro, S. J. L. Ribeiro, E. Jimenez-Villar, *RSC Adv.* **2018**, *8*, 29678–29685.
- [324] L. Cerdán, E. Enciso, V. Martín, J. Bañuelos, I. López-Arbeloa, A. Costela, I. García-Moreno, *Nature Photonics* **2012**, *6*, 621–626.
- [325] K. Kuriki, T. Kobayashi, N. Imai, T. Tamura, S. Nishihara, Y. Nishizawa, A. Tagaya, Y. Koike, Y. Okamoto, *Appl. Phys. Lett.* **2000**, *77*, 331–333.
- [326] A. Costela, F. Florido, I. Garcia-Moreno, R. Duchowicz, F. Amat-Guerri, J. M. Figuera, R. Sastre, *Applied Physics B: Lasers and Optics* **1995**, *60*, 383.
- [327] A. Costela, I. Garcia-Moreno, J. M. Figuera, F. Amat-Guerri, R. Mallavia, M. D. Santa-Maria, R. Sastre, *Journal of Applied Physics* **1996**, *80*, 3167–3173.
- [328] N. Tsutsumi, Y. Hirano, K. Kinashi, W. Sakai, *Langmuir* **2018**, *34*, 7527–7535.
- [329] N. Tsutsumi, S. Nagi, K. Kinashi, W. Sakai, *Sci Rep* **2016**, *6*, 34741.
- [330] L. Wang, Y. Sun, Z. Li, A. Wu, G. Wei, *Materials (Basel)* **2016**, *9*, DOI 10.3390/ma9010053.
- [331] J. T. Overpeck, C. Conde, *Science* **2019**, *364*, 807–807.
- [332] M. H. Ahmadi, M. Ghazvini, M. Alhuyi Nazari, M. A. Ahmadi, F. Pourfayaz, G. Lorenzini, T. Ming, *Int J Energy Res* **2019**, *43*, 1387–1410.
- [333] E. Serrano, G. Rus, J. García-Martínez, *Renewable and Sustainable Energy Reviews* **2009**, *13*, 2373–2384.
- [334] Y. Zi, Z. L. Wang, *APL Materials* **2017**, *5*, 074103.
- [335] B. Jaffe, R. S. Roth, S. Marzullo, *J. RES. NATL. BUR. STAN.* **1955**, *55*, 239.
- [336] S. Velasco-Lozano, M. Knez, F. López-Gallego, *ACS Appl. Energy Mater.* **2018**, *1*, 2032–2040.
- [337] R. Sugadev, M. N. Ponnuswamy, K. Sekar, **n.d.**, 11.
- [338] L. Cao, **n.d.**, 580.
- [339] J. Zdarta, A. Meyer, T. Jesionowski, M. Pinelo, *Catalysts* **2018**, *8*, 92.
- [340] S. Datta, L. R. Christena, Y. R. S. Rajaram, *3 Biotech* **2013**, *3*, 1–9.
- [341] J. Britton, S. Majumdar, G. A. Weiss, *Chem. Soc. Rev.* **2018**, *47*, 5891–5918.
- [342] S. Velasco-Lozano, F. López-Gallego, R. Vázquez-Duhalt, J. C. Mateos-Díaz, J. M. Guisán, E. Favela-Torres, *Biomacromolecules* **2014**, *15*, 1896–1903.
- [343] F. López-Gallego, E. Jackson, L. Betancor, *Chem. Eur. J.* **2017**, *23*, 17841–17849.
- [344] I. Aranaz, N. Acosta, A. Heras, *Biocatalysis and Biotransformation* **2018**, *36*, 89–101.
- [345] J. E. Hyeon, S. K. Shin, S. O. Han, *Biotechnology Journal* **2016**, *11*, 1386–1396.
- [346] A. L. Cortajarena, J. Wang, L. Regan, *FEBS Journal* **2010**, *277*, 1058–1066.
- [347] Z. Liu, Z. Zhang, R. O. Ritchie, *Advanced Materials* **2018**, *30*, 1705220.
- [348] C. Ezquerro, E. Fresta, E. Serrano, E. Lalinde, J. García-Martínez, J. R. Berenguer, R. D. Costa, *Materials Horizons* **2019**, DOI 10.1039/C8MH00578H.
- [349] A. J. C. Kuehne, M. C. Gather, *Chemical Reviews* **2016**, *116*, 12823–12864.
- [350] Igor Meglinski, *Biophotonics for Medical Applications*, Woodhead Publishing, **2015**.
- [351] N. C. Abascal, L. Regan, *Open Biology* **2018**, *8*, 180113.
- [352] Y. Sun, Z. Guo, *Nanoscale Horizons* **2019**, *4*, 52–76.
- [353] C. Zhang, D. A. Mcadams, J. C. Grunlan, *Advanced Materials* **2016**, *28*, 6292–6321.
- [354] M. J. Webber, E. A. Appel, E. W. Meijer, R. Langer, *Nature Materials* **2016**, *15*, 13–26.
- [355] W. Huang, S. Ling, C. Li, F. G. Omenetto, D. L. Kaplan, *Chemical Society Reviews* **2018**, *47*, 6486–6504.
- [356] J. Zdarta, A. Meyer, T. Jesionowski, M. Pinelo, *Catalysts* **2018**, *8*, 92.
- [357] H.-T. Deng, Z.-K. Xu, Z.-M. Liu, J. Wu, P. Ye, *Enzyme and Microbial Technology* **2004**, *35*, 437–443.
- [358] M. B. Méndez, C. W. Rivero, F. López-Gallego, J. M. Guisán, J. A. Trelles, *Journal of Biotechnology* **2018**, *270*, 39–43.

- [359] Q. Zhu, W. Zhuang, H. Niu, L. Ge, B. Villacorta Hernandez, J. Wu, K. Wang, D. Liu, Y. Chen, C. Zhu, et al., *Colloids and Surfaces B: Biointerfaces* **2018**, *164*, 155–164.
- [360] R. L. de Oliveira, O. S. da Silva, A. Converti, T. S. Porto, *International Journal of Biological Macromolecules* **2018**, *115*, 1088–1093.
- [361] S. Escobar, C. Bernal, J. M. Bolivar, B. Nidetzky, F. López-Gallego, M. Mesa, *Molecular Catalysis* **2018**, *449*, 106–113.
- [362] M. S. Mohy Eldin, C. G. P. H. Schroën, A. E. M. Janssen, D. G. Mita, J. Tramper, *Journal of Molecular Catalysis B: Enzymatic* **2000**, *10*, 445–451.
- [363] A. G. Grigoras, *Biochemical Engineering Journal* **2017**, *117*, 1–20.
- [364] A. Härtl, E. Schmich, J. A. Garrido, J. Hernando, S. C. R. Catharino, S. Walter, P. Feulner, A. Kromka, D. Steinmüller, M. Stutzmann, *Nature Materials* **2004**, *3*, 736–742.
- [365] G. Zhang, M. B. Quin, C. Schmidt-Dannert, *ACS Catalysis* **2018**, *8*, 5611–5620.
- [366] Y. L. Boersma, A. Plückthun, *Current Opinion in Biotechnology* **2011**, *22*, 849–857.
- [367] S. H. Mejias, A. Aires, P. Couleaud, A. L. Cortajarena, *Adv. Exp. Med. Biol.* **2016**, *940*, 61–81.
- [368] M. Alfonso-Prieto, X. Biarnés, P. Vidossich, C. Rovira, *Journal of the American Chemical Society* **2009**, *131*, 11751–11761.
- [369] K. K. Gaikwad, S. Singh, Y. S. Lee, *Environmental Chemistry Letters* **2018**, *16*, 523–538.
- [370] J. Kaushal, S. Mehandia, G. Singh, A. Raina, S. K. Arya, *Biocatalysis and Agricultural Biotechnology* **2018**, *16*, 192–199.
- [371] J. M. Bolivar, S. Schelch, M. Pfeiffer, B. Nidetzky, *Journal of Molecular Catalysis B: Enzymatic* **2016**, *134*, 302–309.
- [372] M. R. Chapman, S. C. Cosgrove, N. J. Turner, N. Kapur, A. J. Blacker, *Angewandte Chemie International Edition* **2018**, *57*, 10535–10539.
- [373] R. C. Rodrigues, C. Ortiz, Á. Berenguer-Murcia, R. Torres, R. Fernández-Lafuente, *Chem. Soc. Rev.* **2013**, *42*, 6290–6307.
- [374] A. Starzyk, M. Cieplak, *The Journal of Chemical Physics* **2011**, *135*, 235103.
- [375] T. Kajander, A. L. Cortajarena, L. Regan, in *Protein Design*, Humana Press, New Jersey, **2006**, pp. 151–170.
- [376] A. G. Destaye, C.-K. Lin, C.-K. Lee, *ACS Applied Materials & Interfaces* **2013**, *5*, 4745–4752.
- [377] C. J. Lusty, *Journal of Applied Crystallography* **1999**, *32*, 106–112.
- [378] S. Velasco-Lozano, M. Knez, F. López-Gallego, *ACS Applied Energy Materials* **2018**, *1*, 2032–2040.
- [379] J. Briscoe, N. Jalali, P. Woolliams, M. Stewart, P. M. Weaver, M. Cain, S. Dunn, *Energy & Environmental Science* **2013**, *6*, 3035.
- [380] C. Riccardi, S. McCormick, R. Kasi, C. Kumar, *Angewandte Chemie International Edition* **2018**, *57*, 10158–10162.
- [381] G. Ozyilmaz, S. S. Tukel, O. Alptekin, *INDIAN J. BIOCHEM. BIOPHYS.* **2007**, *44*, 6.
- [382] A. C. O. Mafra, W. Kopp, M. B. Beltrame, R. de Lima Camargo Giordano, M. P. de Arruda Ribeiro, P. W. Tardioli, *Journal of Molecular Catalysis B: Enzymatic* **2016**, *133*, 107–116.
- [383] J. Kaushal, Seema, G. Singh, S. K. Arya, *Biotechnology Reports* **2018**, *18*, e00258.